

寻找与引力波或伽马暴关联的大亚 湾实验中微子信号

(申请清华大学理学博士学位论文)

培 养 单 位： 工程物理系

学 科： 物理学

研 究 生： 郭 磊

指 导 教 师： 陈 少 敏 教 授

二〇二〇年十一月

**Search for neutrinos associated with
gravitational-waves or gamma-ray bursts
at Daya Bay**

Dissertation Submitted to
Tsinghua University
in partial fulfillment of the requirement
for the degree of
Doctor of Philosophy
in
Physics
by
Guo Lei

Dissertation Supervisor: Professor Chen Shaomin

November, 2020

学位论文公开评阅人和答辩委员会名单

公开评阅人名单

无（全隐名评阅）

答辩委员会名单

主席	曹臻	研究员	中科院高能所
委员	衡月昆	研究员	中科院高能所
	王晓锋	教授	清华大学物理系
	冯骅	教授	清华大学天文系
	CHEN SHAOMIN	教授	清华大学工物系
	王喆	副教授	清华大学工物系
秘书	续本达	助理教授	清华大学工物系

摘要

与引力波（GW）或伽马暴（GRB）事例关联的中微子，是指在宇宙中由致密双星体合并或者大质量恒星塌缩过程而伴随产生的，并具有短时间爆发特征的中微子。目前为止，理论对于这类天体事件内部发生的物理过程并不清楚。宇宙中穿梭的中微子，与物质极其微弱的相互作用使其能够作为信使，携带天体点源内部最原始的信息到达地球上的探测器。在已经到来的多信使观测时代，中微子、引力波和伽马暴的联合观测对于了解这些天体过程的动力学机制及宇宙的演化至关重要。本论文在大亚湾反应堆中微子实验装置上，利用大亚湾 8 个子探测器共约 340 吨液体闪烁体，开展了关联信号的寻找。主要工作与创新点如下：

- 研究了反电子中微子的反贝塔衰变反应过程的能量微分截面，分析了随能量增加截面计算的偏差。讨论了反应产生的反冲中子能量对正电子能量测量的影响，并给出了修正公式。在模拟研究中，对上述过程产生的延迟中子慢化过程及俘获截面所采用的不同数据库进行了比较，并估计出了对探测效率的影响。
- 在大亚湾实验中，具有瞬发正电子与延迟中子俘获信号特征的反电子中微子事例被用来与目前为止最全的致密星体合并产生的引力波事例进行了关联，例如，GW150914, GW151012, GW151226, GW170104, GW170608, GW170814 和 GW170817。根据不同的物理动机需求，我们采用了多个搜索时间窗口， ± 10 s, ± 500 s 和 ± 1000 s 来搜索中微子信号，发现事例数与本底水平相符，并据此导出相应的中微子通量上限。在单能谱的假设下，给出了 90% 置信区间下 5 MeV - 90 MeV 的中微子通量上限为 $(1.12 - 2.28) \times 10^{11} \text{ cm}^{-2}$ 到 $1.0 \times 10^8 \text{ cm}^{-2}$ 。在费米-狄拉克能谱的假设下，中微子在 (1.8 MeV, 100 MeV) 能区和不同时间窗口的通量上限范围为 $(4.2 - 5.5) \times 10^9 \text{ cm}^{-2}$ 。
- 分析了从 2011 年 12 月到 2019 年 3 月期间，共计 2225 个伽马暴事例，关联中微子信号的搜寻时间窗口包括 ± 500 s, ± 1000 s，以及一个由不同伽马暴持续时间以及红移决定的动态时间窗口。搜索结果显示，中微子信号数相对于本底数目没有明显的超出迹象。在 90% 置信区间下的单能谱假设的通量上限范围为 $0.08 \times 10^7 \text{ cm}^{-2}$ 到 $2.03 \times 10^{10} \text{ cm}^{-2}$ 之间。在费米-狄拉克的能谱假设下的上限范围是 $(2.08 - 10.8) \times 10^7 \text{ cm}^{-2}$ 。这些是国际上最新的 GRB 关联中微子通量的上限结果。

关键词：中微子；中微子探测；引力波；伽马暴；通量

Abstract

Neutrinos associated with gravitational waves (GW) or gamma-ray bursts (GRB) are produced in the universe during the coalescence of compact binaries or the collapse of massive stars and have characteristics of short bursts. So far, theories are unclear about the physical processes that occur inside such celestial events. Neutrinos travel through space, interacting so weakly with matter that they act as messengers, carrying the most primitive information from the interior of celestial point sources to detectors on Earth. In the era of multi-messengers, combined observations of neutrinos, gravitational waves, and gamma-ray bursts are crucial to understanding the dynamics of these celestial processes and the universe's evolution. This dissertation used about 340 tons of liquid scintillators in 8 electron anti-neutrino detectors in Daya Bay to search for correlated signals. The main work and innovations are as follows:

- The energy differential cross-section of the inverse-beta-decay reaction for electron anti-neutrinos was studied by analyzing the deviation of cross-section calculations with increasing energy. The recoil neutron's influence on positron energy measurement was under discussion and yielding a modified formula to take effect into account. We performed simulation studies to compare the different databases for the thermalization, capture the above reaction's cross-section of the delayed neutron, and estimated the effect on detection efficiency.
- We searched for electron anti-neutrino events with a prompt positron and delayed neutron capture signals associated with the complete gravitational wave events-GW150914, GW151012, GW151226, GW170104, GW170608, GW170814, and GW170817-caused by compact binaries' mergers in the Daya Bay experiment. According to different motivations, we applied multiple search time windows, ± 10 s, ± 500 s, and ± 1000 s. We found that all were consistent with the background level and accordingly derived the corresponding upper limit of neutrino fluence. Under the monochromatic energy spectra's assumption, the upper limit of neutrino fluence of 5 MeV - 90 MeV at 90% confidence interval is $(1.12 - 2.28) \times 10^{11} \text{ cm}^{-2}$ to $1.0 \times 10^8 \text{ cm}^{-2}$. Under the assumption of the Fermi-Dirac energy spectrum, the upper limit of neutrino fluence in (1.8 MeV, 100 MeV) energy region and different time windows is $(4.2 - 5.5) \times 10^9 \text{ cm}^{-2}$.

- We analyzed a total of 2225 events of GRBs occurring from December 2011 to March 2019. The searching time window of correlated neutrino signal includes ± 500 s, ± 1000 s, and a dynamic time window determined by different GRBs duration and redshift. The results show that the number of neutrino signals did not exceed the number of backgrounds. The upper limit of fluence at the Daya Bay experiment was between $0.08 \times 10^7 \text{ cm}^{-2}$ and $2.03 \times 10^{10} \text{ cm}^{-2}$ at the 90% confidence level for the monochromatic energy spectra hypothesis and $(2.08 - 10.8) \times 10^7 \text{ cm}^{-2}$ for the Fermi-Dirac energy spectrum assumption. These limits are the latest upper bound results of GRB associated neutrino fluence in the world.

Key Words: neutrino; neutrino detection; Gravitational-Wave; Gamma-Ray burst; fluence

Contents

摘要.....	I
Abstract	II
Contents.....	IV
List of Figures.....	VII
List of Tables	XV
Nomenclature	XVIII
Chapter 1 Introduction.....	1
1.1 The Standard Model and neutrinos	1
1.1.1 Neutrinos in the Standard Model	2
1.1.2 Neutrino sources	3
1.2 Gravitational-Waves	4
1.2.1 Observation	5
1.2.2 Neutrino production	7
1.2.3 Related searches and experiments	9
1.3 Gamma-Ray bursts.....	10
1.3.1 GRB phenomenology.....	10
1.3.2 Neutrino production	13
1.3.3 Previous experimental searches.....	18
1.4 Thesis organization	19
Chapter 2 The Daya Bay reactor neutrino experiment.....	21
2.1 Physical significance.....	21
2.2 The design and layout	22
2.3 Anti-neutrino detector	26
2.4 Muon veto system.....	28
2.5 Calibration and energy reconstruction.....	29
2.5.1 Time calibration.....	30
2.5.2 Energy reconstruction	30

2.5.3	Energy resolution	31
2.6	Data taking	31
2.6.1	Detector operation	31
2.6.2	Reconstructed data production	33
Chapter 3	Neutrino energy and fluence	34
3.1	Energy conversion	34
3.2	Neutrino fluence.....	37
Chapter 4	Simulation studies	39
4.1	IBD cross-section	39
4.1.1	IBD cross-section formulae.....	39
4.1.2	IBD cross-section in GW and GRB analyses	41
4.2	Study of the neutron databases in Geant4.....	41
4.2.1	Geant4 simulation for neutrons	42
4.2.2	The fast simulation framework.....	42
4.2.3	Simulation results	42
4.3	Full simulation package for the Daya Bay experiment.....	46
4.4	The capture fraction of IBD neutrons	47
4.5	Chapter summary.....	48
Chapter 5	Events selection criteria and efficiency.....	49
5.1	Events selection criteria	49
5.2	Definition of detection efficiency	51
5.3	Efficiency for the monochromatic spectra	52
5.4	Efficiency for the Fermi-Dirac spectrum	55
5.5	Chapter summary.....	57
Chapter 6	Measurement of $\bar{\nu}_e$ associated with GWs	58
6.1	Analysis strategy	58
6.1.1	Validation of likelihood function.....	58
6.1.2	Maximum likelihood fitting	60
6.2	Data analysis	63
6.2.1	Search time windows	63
6.2.2	Data sample.....	65
6.2.3	Background estimation.....	68

6.2.4	IBD candidates	72
6.2.5	Signal significance	76
6.3	Results of $\bar{\nu}_e$ searches	78
6.3.1	Limits on $\bar{\nu}_e$ fluence	78
6.3.2	Limits on $\bar{\nu}_e$ luminosity	80
6.4	Chapter summary	82
Chapter 7 Measurement of $\bar{\nu}_e$ associated with GRBs		84
7.1	Data analysis	84
7.1.1	GRBs data set	84
7.1.2	Search time windows	86
7.1.3	Selected GRBs	88
7.1.4	Background estimation	89
7.1.5	IBD candidates	91
7.2	Results of $\bar{\nu}_e$ searches	95
7.3	Chapter summary	96
Chapter 8 Conclusion		97
Bibliography		101
Appendix A Geant4 9.6 physical list		109
Appendix B Geant4 10.3 physical list		113
Appendix C Muon veto efficiency and multiplicity cut efficiency		116
Appendix D IBD candidates for all GWs		119
Appendix E Summary parameters to calculate neutrino fluence		132
Appendix F IBD candidates for all GRBs		136
Acknowledgements		140
声 明		141
Resume and Academic Achievements		142
指导教师学术评语		143
答辩委员会决议书		144

List of Figures

- Figure 1.1 Twelve elementary fermions and four gauge bosons. The purple part represents six quarks. The green part represents six leptons. The orange part represents four bosons. The yellow part represents Higgs boson. (From Ref.^[13]).
..... 2
- Figure 1.2 Summary of the spectra of dominant natural and artificial neutrino fluxes. The energy range from μeV to meV is that of cosmological (or “relic”) neutrinos. The keV-MeV energy range is dominant from the Sun, supernovae, nuclear reactor, and the Earth (“Terrestrial” or “geo-” anti- ν). A higher energy ranges are populated by neutrinos from the atmospheric in the Earth, supernova remnants, and Active Galactic Nuclei (AGN). (From Ref.^[15]). 3
- Figure 1.3 Illustration of the merger of two BHs. The GW ripples outward when the BHs spiral toward each other. The area near the BHs would appear highly warped. The GW is difficult to be observed directly. The plot comes from Ref.^[22]. 5
- Figure 1.4 The shift in periastron time varies with the year since 1975 when two stars keep getting closer. The curve change shows the PSR 1913+16’s orbit decreasing continuously in 30 years. The points represent the measurements. The plot comes from Ref.^[24] 6
- Figure 1.5 A schematic diagram of a laser interferometer. (From Ref.^[29]). 7
- Figure 1.6 GW150914 signal from a binary BH merges observed at Hanford, Washington (H1, left column panels) and Livingston, Louisiana (L1, right column panels). The origin of x-axis is the time detected. The top two panels show that the GW signal was first detected by L1, and then by H1. The second row shows the GW signal spectrum predicted by different models. The third row shows the Residuals after subtracting the filtered numerical relativity waveform from the filtered detector time series. The bottom row shows that the signal frequency over time. (From Ref.^[30]). 8

Figure 1.7	Neutrino spectra for the proton-neutron stars (PNS) and the accretion disk of black holes (AD-BH) without the oscillation. The \dot{m} represents the accretion rates. (From Ref. ^[39]).....	9
Figure 1.8	“naked-eye” GRB generated in artist’s concept. The observation shows two jets in opposite directions from the center. (white and green beams). (From Ref. ^[46]).	11
Figure 1.9	Positions of all the GRBs detected by BASTE on the sky. The shade of color represents the difference in fluence. The horizontal central axis of the picture represents the Milky Way. The distribution of GRBs is isotropic in the universe ^[49]	12
Figure 1.10	Duration time T_{90} distribution of GRBs detected by BATSE ^[50]	13
Figure 1.11	Time profile of GRB examples observed by BATSE. (From Ref. ^[52])....	14
Figure 1.12	Fitting results of GRB 990123 spectra, and top panel displays the photon flux and the bottom panel displays the energy flux. (From Ref. ^[54]).....	15
Figure 1.13	Cartoon schematic of a GRB generated from the relativistic fireball. When the internal shells collide with the external shells, γ -rays and neutrinos are generated. As the external shells expand outward, they collide with the medium and then produce γ -rays, Optical, Radio, X-rays, and high-energy neutrinos. Credit: NASA.....	16
Figure 1.14	Feynman diagram for the process $e^-e^+ \rightarrow \nu_l\bar{\nu}_l$ ($l = e, \tau, \mu$).....	16
Figure 1.15	Upper limits of $\bar{\nu}_e$ from GRBs versus MeV neutrino energy. (From Ref. ^[70]).....	18
Figure 2.1	Elevation profile of the mountain above the experimental and the depth meter water equivalent (m.w.e.) of each hall. (From Ref. ^[84]).....	23
Figure 2.2	Layout of eight detectors and six reactor cores in the Daya Bay reactor neutrino experiment. The black line represents the tunnels that connect each EH. The red points stand for the reactor cores in each NNP. (From Ref. ^[86])...	24
Figure 2.3	Reactor anti-neutrino disappear probability as a function of distance from the source. $P_{\text{dis}} = P_{12} + P_{13}$ is the total disappearance probability. (From Ref. ^[87]).	25
Figure 2.4	Diagram of prompt and delayed generation in IBD interaction. (From Ref. ^[89]).	27
Figure 2.5	Schematic for a Daya Bay antineutrino detector. (From Ref. ^[86]).	28

Figure 2.6	Structure of the Daya Bay reactor neutrino experiment in the near-site. It consists of the central detector, the water Cherenkov detectors, and the RPC detector. (From Ref. ^[86]).	30
Figure 2.7	The open blue makers represent the energy resolution measured by calibration sources, IBD neutrons, and natural α particles. The blue solid line represents the limits of resolution given by the statistical uncertainty of photoelectron counting. The solid orange markers reveal that the resolutions are consistent with the Monte-Carlo simulation. The dashed orange shows that the predicted from the simulation is better than estimated for the calibration sources. The open blue triangles represent the resolutions for natural α particles. (From Ref. ^[94]).	32
Figure 2.8	Time line of Daya Bay data taking and AD installation.	32
Figure 3.1	Relationship between true kinetic energy of positrons and neutrinos in the simulation.	35
Figure 3.2	Distributions of true kinetic energy and quenching energy loss of neutrons in the simulation.	36
Figure 3.3	Relation between neutrino energy and prompt energy. The black line represents the prompt energy. The red line represents the fitting result of the prompt energy. A simple fitting was adopted. $E_p = A \times E_\nu^2 + B \times E_\nu + C$, where $A = -0.001 \text{ MeV}^{-1}$, $B = 1.01$, $C = -0.73 \text{ MeV}$. The blue line represents the average kinetic energy of neutrons.	36
Figure 3.4	Fermi-Dirac energy and flux spectra for the electron anti-neutrinos	37
Figure 3.5	Schematic flow of the neutrino generation from GWs or GRBs to the Daya Bay detectors. Furthermore, it also provides the neutrino fluence calculation and the main background sources for our analysis.	38
Figure 4.1	Upper panel is the total cross-section for $\bar{\nu}_e + p \rightarrow e^+ + n$. The bottom panel is the average $\langle \cos\theta \rangle$. The solid line is the result at first order in $1/M$ where M is the nucleon mass and the short-dashed line is result at zeroth order in $1/M$. The long-dashed line is the result of Eq.(3.18) of Ref. ^[100] . The dot-dashed line is the result after considering the contributions of the threshold ($E_\nu = 1.806 \text{ MeV}$) effects. (From Ref. ^[69]).	40
Figure 4.2	Distribution of total cross-section versus neutrino energy below 100 MeV and distribution of $\cos\theta$ of neutrino energy 10 MeV.	41

Figure 4.3	Summary of neutron simulation processes to study the influence brought by different Geant4 physical lists. “Sim.” means simulation. “frac.” means fraction.	43
Figure 4.4	Schematic view of the detector in the simulation. Neutrons generated uniformly in the GdLS region.	43
Figure 4.5	Neutron’s flight time until captured in the GdLS. Several discrete neutron kinetic energies were selected and simulated in the two different Geant4 versions, respectively. Neutrons are put into the GdLS region and isotropic emitted.	44
Figure 4.6	Neutron’s flight distance until captured in the GdLS. Several discrete neutron kinetic energies were selected and simulated in the two different Geant4 versions, respectively. Neutrons are put into the GdLS region and isotropic emitted.....	45
Figure 4.7	Block diagram for the simulation processes in NuWa at Daya Bay.....	46
Figure 4.8	Detailed simulation processes for a 90 MeV neutrino case at NuWa. The numbers in the flow chart are the branching ratio of IBD events. “Gd-Cap” represents the physical process of Gd-captured. “H-Cap” represents the physical process of H-captured. “O-Cap” represents the physical process by other nuclei captured. “Inelastic-S” represents the inelastic scattering physical process. We only recorded the neutron tracks in the simulation because it is the delayed signal for IBD events.	47
Figure 5.1	Simulated efficiency of nH and nGd data in the detector simulation.	54
Figure 5.2	Distribution of the actual capture vertex of neutron in the GdLS and LS volume.....	56
Figure 5.3	IBD selection efficiency, ϵ_{other} , from the MC simulation as a function of the electron anti-neutrino energy.	57
Figure 6.1	Two simple examples validate the likelihood-based function used in the thesis.	59
Figure 6.2	Illustration of the relation between the p -value and the observed t_s and also with the significance Z	60
Figure 6.3	Data sources and structure in the analysis. “LE” represents low energy region($E_p < 10$ MeV). “HE” represents high energy region.	61

Figure 6.4	Flow chart of the $\bar{\nu}_e$ fluence calculation. “IBD. Cand.” represents observed IBD candidates. “Exp. BKG.” represents expected background events. “FCN” represents function. “U.L.” represents upper limit.	61
Figure 6.5	Distribution of IBD candidates of each GW within ± 1000 s.	63
Figure 6.6	Summary of the coincidence time of the neutrinos and the GW emission. (a) There is a 100 s time window to activate the central engine before breaking out. (b) The relativistic jet breaks out from the envelope. (c) The duration time has 250 s precursor before the GRB breaks out. (d) The main GRB burst time window is ~ 150 s. (e) The whole time is ± 500 s when both neutrinos and GWs emission may happen. (From Ref. ^[112]).	64
Figure 6.7	Observed IBD events survived from the IBD selection criteria at Daya Bay.	65
Figure 6.8	Energy distribution of the prompt energy versus the delayed energy from the P17B data sample.	66
Figure 6.9	Distribution of the coincident time for the nGd and the nH.	66
Figure 6.10	Distribution of the coincident distance between the prompt signal vertex and the delayed signal vertex for the nH from P17B data sample.	67
Figure 6.11	Distribution of the IBD event rates for the low-energy and high-energy events within ± 5 days of the GW150914 arrival time. The errors are statistical only.	68
Figure 6.12	Distribution of the IBD event rates for the low-energy and high-energy events within ± 5 days of the GW151012 arrival time. The errors are statistical only.	69
Figure 6.13	Distribution of the IBD event rates for the low-energy and high-energy events within ± 5 days of the GW151226 arrival time. The errors are statistical only.	69
Figure 6.14	Distribution of the IBD event rates for the low-energy and high-energy events within (-1, +5) days of the GW170104 arrival time. Detectors were turned off for a few days, which lead to the absence of some data. Furthermore, EH1 was not working normally and removed from the rate stability check. The errors are statistical only.	70

Figure 6.15	Distribution of the IBD event rates for the low-energy and high-energy events within ± 5 days of the GW170608 arrival time. The rate in EH1 is lower than EH2 due to only one AD working. The errors are statistical only.	70
Figure 6.16	Distribution of the IBD event rates for the low-energy and high-energy events within ± 5 days of the GW170814 arrival time. The rate in EH1 is lower than EH2 due to only one AD working. There is a blank in the rate because of the detector switch. The errors are statistical only.	71
Figure 6.17	Distribution of the IBD event rates for the low-energy and high-energy events within ± 5 days of the GW170817 arrival time. The rate in EH1 is lower than EH2 due to only one AD working. The errors are statistical only.	71
Figure 6.18	Prompt energy spectra of IBD candidates using the P17B data. The statistical uncertainty is considered.	72
Figure 6.19	Energy distribution of IBD candidates and expected background events of all GW events assuming the monochromatic spectra	73
Figure 6.20	Neutrino energy and relative time distribution of IBD candidates for GW150914.	74
Figure 6.21	Neutrino energy and relative time distribution of IBD candidates for GW151012.	74
Figure 6.22	Neutrino energy and relative time distribution of IBD candidates for GW151226.	75
Figure 6.23	Neutrino energy and relative time distribution of IBD candidates for GW170104.	75
Figure 6.24	Neutrino energy and relative time distribution of IBD candidates for GW170608.	75
Figure 6.25	Neutrino energy and relative time distribution of IBD candidates for GW170814.	76
Figure 6.26	Neutrino energy and relative time distribution of IBD candidates for GW170817.	76
Figure 6.27	Summary of all the GW events within the time window ± 1500 s. The origin of the x-axis represents the time when the GWs were detected.	77

Figure 6.28	90% C.L. upper limit of the fluence of $\bar{\nu}_e$ from GW. The “W” in the plot means the time window.....	79
Figure 7.1	Distribution of 1686 GRBs with T_{90} from December 2011 to March 2019.	85
Figure 7.2	Redshift information of the 212 GRBs recorded. (a) shows the distribution of the 212 GRBs and (b) show the distribution of redshift versus the date-time.	85
Figure 7.3	The number of GRBs observed in different Daya Bay operation time.	86
Figure 7.4	Relative flight-time delay distribution of the 212 GRBs recorded with the redshift.....	88
Figure 7.5	Signal time window is surrounded by the background time window. The GRB trigger is the trigger time fired by the detector on the earth.....	88
Figure 7.6	Definition of overlapping time between two GRBs.	89
Figure 7.7	Event rate for the data sample in the three experimental halls. In different experiment periods, Daya Bay has different numbers of ADs, which result in the event rate fluctuation of each experimental hall.....	90
Figure 7.8	Distribution of total IBD candidates of all GRBs assuming the monochromatic spectra.	91
Figure 7.9	Distributions of the number of GRBs correlated IBD candidates within the ± 500 s and ± 1000 s time window in EH1. The distribution of IBD candidates is fitted with a Poisson distribution.....	92
Figure 7.10	Distributions of the number of GRBs correlated IBD candidates within the ± 500 s and ± 1000 s time window in EH2. The distribution of IBD candidates is fitted with a Poisson distribution.	93
Figure 7.11	Distributions of the number of GRBs correlated IBD candidates within the ± 500 s and ± 1000 s time window in EH3. The distribution of IBD candidates is fitted with a Poisson distribution.	94
Figure 7.12	Fluence upper limits on $\bar{\nu}_e$ from GRBs as a function of neutrino energy within three search time windows.	95

Figure 8.1 Fluence upper limits on $\bar{\nu}_e$ ($E_{\bar{\nu}_e} < 20$ MeV) from a GRB as a function of neutrino energy. The neutrino fluence of several neutrino experiments is compared with each other. Borexino Primary and FADC represent two semi-independent DAQ systems in the Borexino neutrino experiment. KamLAND long and short represents the long GRBs and short GRBs, respectively. The neutrino fluence of Daya Bay is the result of a ± 1000 s search time window.....99

List of Tables

Table 1.1	Summary of GWs observed by the LIGO experiment. The masses of BH or NS are given in the source frame. M1 represents the primary mass of BH or NS, and M2 represents the secondary mass of BH or NS. D_{LIGO} represents the luminosity distance. 7	7
Table 2.1	Summary of the overburden, muon flux, and average energy for each EH. The muon flux and average energy are from simulation and the uncertainty of flux is about 10%. (Table data from Ref. ^[85])..... 24	24
Table 2.2	Detailed baselines from the center of six reactor cores to eight detectors. The distances are measured by the combination of station electronic theodolite and GPS with the precision of 18 mm. (Table data from Ref. ^[88]). 26	26
Table 4.1	Verification of our repeat calculation with Strumia and Vissani’s results of $\sigma(\bar{\nu}_e p \rightarrow ne^+)$. The unit of cross-section is 10^{-41} cm^2 . The “ σ_P ” represents the cross-section from Strumia and Vissani’s results . The “ σ_R ” represents the cross-section repeated by this thesis work. The “ $\langle \cos\theta_P \rangle$ ” represents the average cosine of the scattering angle from Strumia and Vissani’s results. The “ $\langle \cos\theta_R \rangle$ ” represents the average cosine of the scattering angle repeated from our work. 40	40
Table 4.2	IBD cross-section for discrete energy points and the average IBD cross-section, $\bar{\sigma}(E_\nu)$, for the Fermi-Dirac spectrum. 41	41
Table 4.3	Neutron capture fractions in the two different Geant4 versions for several specific neutron energies. The uncertainties are only statistical. 45	45
Table 4.4	Neutron captured fractions by different target elements in the GdLS volume is calculated. 48	48
Table 5.1	IBD selection criteria for the nH and nGd analyses. The details in the text. 49	49
Table 5.2	Summary of the efficiencies under the assumption of the Fermi-Dirac spectrum. $\varepsilon_{\text{other}}$ is the total IBD selection efficiency evaluated by Monte Carlo for the whole detector including GdLS ,LS and Acrylic. 57	57

Table 6.1	The 90% C.L. and 95% C.L. intervals for the Poisson signal mean s (for total observed events n , and known mean background b ranging from 0 to 7). Our results s are indicated by the “P-L”, and Feldman’s result ^[111] s are by the “F-C”, respectively.....	60
Table 6.2	Average background rate (per second per antineutrino detector) for the studied energy spectrum (Low E: $E_p < 10$ MeV, High E: $E_p > 10$ MeV).	74
Table 6.3	The p -values of signal significance for the $E_\nu = 5$ MeV energy points assuming the monochromatic spectra. The “nH+nGd” represents the combined of nH and nGd data.	78
Table 6.4	The p -values of signal significance for the $E_\nu = 7$ MeV energy points assuming the monochromatic spectra. The “nH+nGd” represents the combined of nH and nGd data.....	78
Table 6.5	Upper limits of fluence at 90% C.L. for three search time windows. The numbers of IBD candidates associated with the GW events and the background were averaged at Daya Bay.	79
Table 6.6	The 90% C.L. upper limits of neutrinos calculated by the averaged signal candidates and averaged background numbers of all GW events within three time windows assuming the Fermi-Dirac spectrum.	80
Table 6.7	Upper limits of $\bar{\nu}_e$ on 90% C.L. at Daya Bay associates with GW events based on the Fermi-Dirac spectrum within the search time window of ± 500 s (low-energy: $E_p < 10$ MeV, high-energy: $E_p > 10$ MeV). For each GW event, the values in the table are explained as follows. The “nGd + nH combine” in the column of the low-energy or high-energy represents the combination of nGd and nH data, which comes from eight ADs. The “Low + High combine” in the row of the nGd sample or nH sample represents the combination of low-energy and high-energy data. The final result in the last column and the last row for every GW event is calculated by the combination of low-energy nGd, low-energy nH, high-energy nGd, and high-energy nH.....	81
Table 6.8	Upper limits of luminosity (Unit: 10^{60} erg) on 90% C.L. associated with the GW events based on the Fermi-Dirac spectrum in the same time window ± 500 s. We summarized four experiment results. “-” represents that there are no experiments to calculate the neutrino fluence or luminosity.	82

Table 7.1	Data summary for GRBs from December 2011 to March 2019. Numbers of GRBs with T_{90} were recorded in the GRBWeb. Numbers of GRBs with redshift z were recorded in the GRBWeb.	84
Table 7.2	Running time of all detectors used in the GRB analysis during the Daya Bay operation time. T_f is the full-time of the detector operation. T_l is the live-time which has removed the detector dead time and the muon veto time, etc. ..	86
Table 7.3	The number of GRBs under three time windows. “Initial” represents the initial number of GRBs. “Removed overlap” represents the remaining GRBs after removing the overlap search time window. “Observed by DYB” represents the final number of GRBs used in the analysis at Daya Bay. “ $\pm T_{\text{Dyna}}$ ” represents the dynamic time window.....	89
Table 7.4	Average background event rates during the Daya Bay live-time assuming the Fermi-Dirac spectrum. The live-time has removed the search time for all GRBs-related ± 1000 s, which is the most extended of the three time windows. (Low-energy: $E_p < 10$ MeV, High-energy: $E_p > 10$ MeV)	90
Table 7.5	The total IBD candidates correlated with GRBs are shown within three search time windows assuming the Fermi-Dirac spectrum (LE: $E_p < 10$ MeV, HE: $E_p > 10$ MeV).....	92
Table 7.6	Fitting values of the distribution of GRB-correlated IBD candidates using a Poisson distribution under a time window of ± 500 s. (Low-energy: $E_p < 10$ MeV, High-energy: $E_p > 10$ MeV)	93
Table 7.7	Fitting values of the distribution of GRB-correlated IBD candidates using a Poisson distribution under a time window of ± 1000 s. (Low-energy: $E_p < 10$ MeV, High-energy: $E_p > 10$ MeV)	94
Table 7.8	Upper limits of fluence at 90% C.L. for three search time windows assuming the monochromatic spectra and the Fermi-Dirac spectrum. The number of $\bar{\nu}_e$ candidates associated with the GRB events are averaged. The background events are also averaged.....	95

Nomenclature

SM	Standard Model
GW	Gravitational-Wave
GRB	Gamma-Ray Burst
IBD	Inverse-Beta-Decay
CC	Charged-Current
NC	Neutral-Current
LEP	Large Electron-Positron
AGN	Active Galactic Nuclei
NS	Neutron Star
BH	Black Hole
M_{\odot}	Solar Mass
PNS	proton-neutron star
BATSE	Burst And Transient Source Experiment
NPP	Nuclear Power Plant
m.w.e	meter water equivalent
EH	Experimental Hall
GdLS	Gadolinium-doped Liquid Scintillator
LS	Liquid Scintillator
Ac	Acrylic
MO	Mineral Oil
PMT	Photomultiplier Tube
SSV	Stainless Steel Vessel
RPC	Resistive Plate Chamber
AD	Anti-neutrino Detector
nGd	Neutron captured on Gadolinium
nH	Neutron captured on Hydrogen
ESR	Enhanced Specular Reflector
ACU	Automatic Calibration Units
IWS	Inner Water Shield
OWS	Outer Water Shield
LED	Light-Emitting Diode

Nomenclature

ADC	Analog to Digital Converter
PE	Photoelectron
DAQ	Data acquisition
MC	Monte-Carlo
GCN	GRB Coordinates of Network

Chapter 1 Introduction

As a branch of physics frontiers, particle physics is of great significance for understanding the fundamental particles and their interactions. Neutrinos are the particles widely distributing in the universe. They can be from stars, atmospheric cosmic rays, supernovae, particle accelerators, and nuclear reactors, etc. Neutrinos rarely interact with matter. This feature allows them to serve as a unique probe for understanding violent astrophysical events, such as compact binaries mergers, supernovae bursts, and gamma-ray bursts. In the Standard Model (SM) picture, neutrinos are left-hand and massless. This chapter will briefly introduce neutrino physics, from its history, SM, to neutrino sources. Also presented are the physics of gravitational waves (GWs) and gamma-ray bursts (GRBs).

1.1 The Standard Model and neutrinos

In 1914, James Chadwick found that the electron β -decay energy spectrum $((N, Z) \rightarrow (N - 1, Z + 1) + e^- + \bar{\nu}_e)$ was continuous, which did not conform to the quantum laws that people knew at the time^[1]. Without the knowledge of $\bar{\nu}$, the β -decay process was thought to be a two-body decay: decaying nuclei and electrons. The continuity of the β -decay energy spectrum contradicted energy and momentum conservation. In 1930, Wolfgang Pauli proposed the concept of neutrino to explain this phenomenon^[2]. Pauli put forward the hypothesis that new particle was light in mass and electrically neutral. It was difficult to detect because of its weak interaction with matter. In 1932, it was named “neutrino” by physicist Enrico Fermi to distinguish neutrons discovered by Chadwick in the nucleus.

In 1956, Frederick Reines and Clyde Cowan eventually discovered the reactor neutrinos via the inverse-beta-decay (IBD)^[3] reaction as below,



In 1957, Bruno Pontecorvo proposed the neutrino oscillation theory, which stated that neutrinos with different flavors could be converted among themselves^[4]. In 1962, Leon M. Lederman, Melvin Schwartz, and Jack Steinberger discovered the ν_μ generated by the de-

cay of π [5]. In 1987, Kamiokande [6-7], IMB [8-9], and Baksan [10-11] neutrino experiments observed the neutrinos from a supernova, which was a milestone event for astrophysics. In 2000, the DONUT experiment from Fermilab announced the discovery of ν_τ [12], the last neutrino flavor predicted by the Standard Model.

1.1.1 Neutrinos in the Standard Model

In the SM, as shown in Fig. 1.1, there are twelve elementary fermions: three generations of quarks, (up, down), (charm, strange), and (top, bottom); three generations of leptons (electron, electron neutrino (ν_e)), (muon, muon neutrino (ν_μ)), and (tau, tau neutrino (ν_τ)). All of which, together with the gauge bosons and Higgs, form the building block of the material world. The elementary fermions interact with each other through four force-carriers, namely g boson, γ boson, Z boson, and W boson.

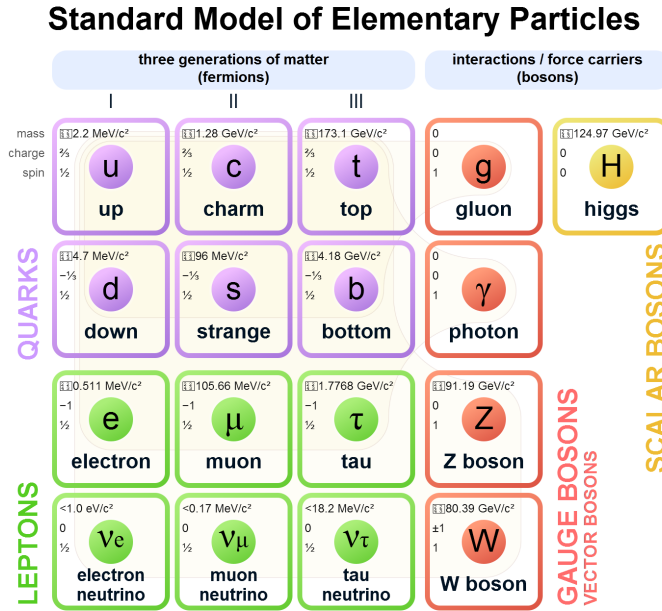


Figure 1.1 Twelve elementary fermions and four gauge bosons. The purple part represents six quarks. The green part represents six leptons. The orange part represents four bosons. The yellow part represents Higgs boson. (From Ref. [13]).

In the SM, the neutrino has a spin of $1/2$, no electric charge, and massless. Neutrinos only interact with matter via either the charged-current (CC) when exchanging the W^\pm bosons or the neutral-current (NC) when the neutrinos exchanging the Z^0 boson. In 1989, the Large Electron-Positron (LEP) Collider experiments measured the number of neutrinos involved in the Z^0 to be 2.9840 ± 0.0082 [14]. It is consistent with the predicted number of three-generation neutrinos in the SM. After a half-century of development, the

SM has achieved great success. Despite this, observation of neutrino oscillation indicates that neutrinos have mass—the only real laboratory evidence that the SM does not predict. Neutrinos can serve as a probe to search for new physics beyond the SM.

1.1.2 Neutrino sources

Figure 1.2 shows the spectra of various neutrinos. The energy ranges from μeV to EeV , and the differential flux can be as high as $10^{22} \text{ cm}^{-2}\text{s}^{-1}\text{sr}^{-1}\text{MeV}^{-1}$. They can be from either natural or artificial sources.

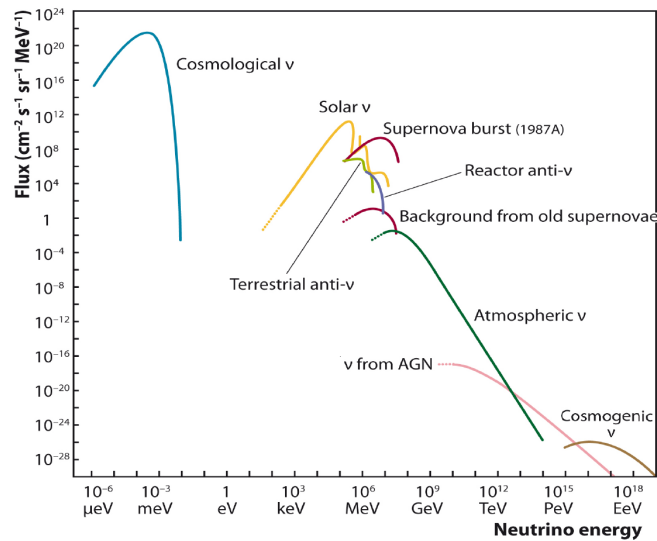


Figure 1.2 Summary of the spectra of dominant natural and artificial neutrino fluxes. The energy range from μeV to meV is that of cosmological (or “relic”) neutrinos. The keV – MeV energy range is dominant from the Sun, supernovae, nuclear reactor, and the Earth (“Terrestrial” or “geo-” anti- ν). A higher energy ranges are populated by neutrinos from the atmospheric in the Earth, supernova remnants, and Active Galactic Nuclei (AGN). (From Ref. [15]).

The Big Bang generated cosmological neutrinos with energy range from μeV to meV . However, detecting cosmological ν 's is challenging due to their low energy and frustratingly small reaction cross-section.

Solar neutrinos are pure electron neutrinos produced from the fusion processes which drive the sun. Measurements of solar neutrinos could enhance the understanding of the neutrino oscillation and solar physics. The fission of heavy nuclei, such as ^{235}U , ^{238}U , ^{239}Pu , and ^{241}Pu in nuclear power plants, emit 6×10^{20} electron anti-neutrinos with energy up to about 10 MeV per second for a typical 3 GW_{th} reactor core. Terrestrial neutrinos are from the radioactive decay chains of ^{232}Th , ^{238}U , ^{235}U , and those of the ^{40}K isotope inside the Earth [16–17], with energy extending to 3.26 MeV . In 1987, supernova 1987A in the

Large Magellanic Cloud was recorded by three neutrino experiments, which opened an era of multi-messengers observation in astrophysics. With the discovery of GWs, neutrinos associated with GWs and GRBs start to draw attention in neutrino experiments.

Much higher energy ranges of neutrinos are dominant from sources, like atmospheric neutrinos (created in cosmic ray interaction with Earth's atmosphere), AGN, and cosmogenic (ultra-energetic protons interaction with the 2.7 Kelvin cosmic microwave background)^[18].

1.2 Gravitational-Waves

The most widespread force in the universe is gravity, one of four fundamental forces in nature. The distribution of mass in the universe has always been a hot topic in cosmological research. The number of neutron stars (NSs) accounts for about 1% of the stellar star in the galaxy. For black holes (BHs), there are many stellar-mass BHs in the galaxy. Moreover, supermassive BHs ($10^6 M_{\odot} - 10^9 M_{\odot}$) always exist in the center of the galaxy^[19]. Quasars, X-rays binaries, and supernovae that use relativistic gravity to convert mass to energy are far more efficient than nuclear reactions. Gravitational radiation plays a role in understanding the mass distribution of the universe. Naturally, the most direct and convenient way to know the gravitational radiation is the observation of GWs. Furthermore, the GW detection opens up a new window for observational astronomy because of the difference between the information carried by GWs and electromagnetic counterparts. This new window can complete our view of the universe and unveil the formation of BHs, the merging of binary systems, and the hidden information of the center of galaxies where the supermassive BHs live, and so on.

GWs are the ripples of space-time caused by instances of high-energy explosions in the universe. The first mention of GWs in history was Albert Einstein in the general theory of relativity in 1916^[20-21]. Einstein predicted that massive objects like neutron stars or black holes would produce the distortions of space-time around them when they are orbiting each other. The more significant the mass, the higher the distortion of space-time. Imagine a small marble ball revolves around a trampoline with a bowling ball in the middle. The marble ball and the bowling ball can be two NSs, BHs, or NS and BH. The two approaching objects release gravitational plane waves. Fig. 1.3 shows that a massive BH merges with a relatively small BH. The released GWs are ripples in space-time, which would propagate in all directions away from the source. The cosmic ripples will carry the

most primitive information inside the origins and spread to the entire universe at the speed of light.

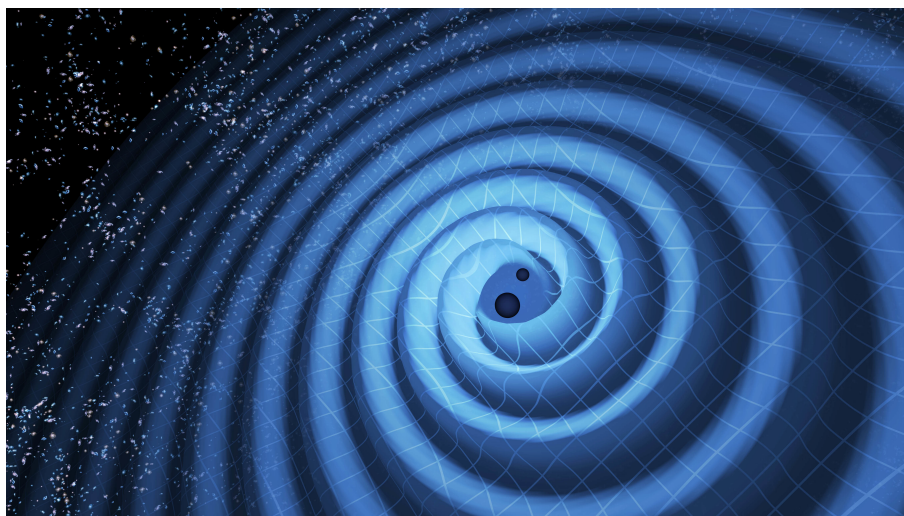


Figure 1.3 Illustration of the merger of two BHs. The GW ripples outward when the BHs spiral toward each other. The area near the BHs would appear highly warped. The GW is difficult to be observed directly. The plot comes from Ref.^[22].

In 1974, Taylor and Hulse discovered a binary pulsar PSR 1913+16 using the Arecibo Radio Observatory in Puerto Rico, which was the first discovery of a binary system according to the general relativity. In 1979, the detection of gravitational radiation effects was announced^[23]. To verify the correctness of general relativity, physicists began to observe PSR 1913+16 for several years and found that the radius of binary orbit decreased with time. This observation showed that the system has been losing energy, which was converted into another way to release it. According to the prediction of the general relativity, GW's emission will cause the loss of energy. Figure 1.4 shows that Einstein's general relativity prediction and the observation from PSR 1913+16 are consistent. In the 20th century, the observations of GWs were all indirect. The astrophysicists hope to observe the existence of GWs directly.

1.2.1 Observation

Three types of detector schemes can observe GWs directly. The first one proposed in 1960 employed a massive cylinder to detect mechanical oscillation induced by a gravitational signal. Joe Weber designed and implemented the detector and published the possible evidence caused by GWs^[25]. However, other similar experiments later failed to confirm the result^[26]. At the end of the 20th century, there were five experiments in the International Gravitational Event Collaboration to search for GW signals using this

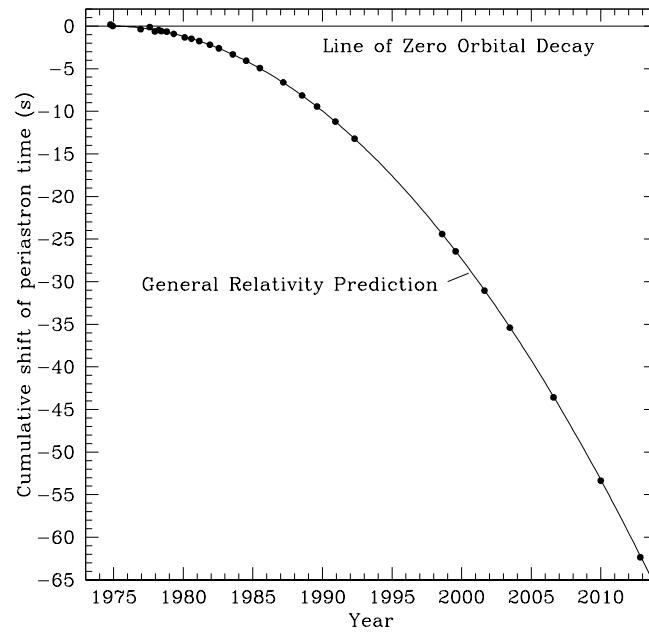


Figure 1.4 The shift in periastron time varies with the year since 1975 when two stars keep getting closer. The curve change shows the PSR 1913+16's orbit decreasing continuously in 30 years. The points represent the measurements. The plot comes from Ref.^[24]

method^[27].

The second scheme is a new approach to observe the GWs. Optical interferometers are composed of freely suspended reflectors at the ends of long paths that are at right angles. Shifts of interference fringes will alternately stretch one arm while contracting the other when the GWs pass. Figure 1.5 shows a schematic diagram of a laser interferometer. The Laser Interferometer Gravitational-Wave Observatory (LIGO)^[28] is the first one that observed GW's direct evidence.

The last scheme is the evolved Laser Interferometer Space Antenna (LISA). LISA has three independent spacecraft that form an equilateral triangle in space. The interferometers are at the corners of a triangle separated by some million km long. A passing gravitational wave will cause a change in distance between the satellites. As the space-based detector, LISA has better sensitivity than the ground-based like LIGO and can measure GW's amplitude, direction, and polarization.

The LIGO is composed of two interferometers, one with arm length 4 km at Hanford, Washington, and one at Livingston, Louisiana. On September 14, 2015, at 09:50:45 UTC, the LIGO detected a coincident GW signal, GW150914, which came from the binary BH mergers^[30]. This discovery has a significance of 5.1σ . Figure 1.6 shows the detected

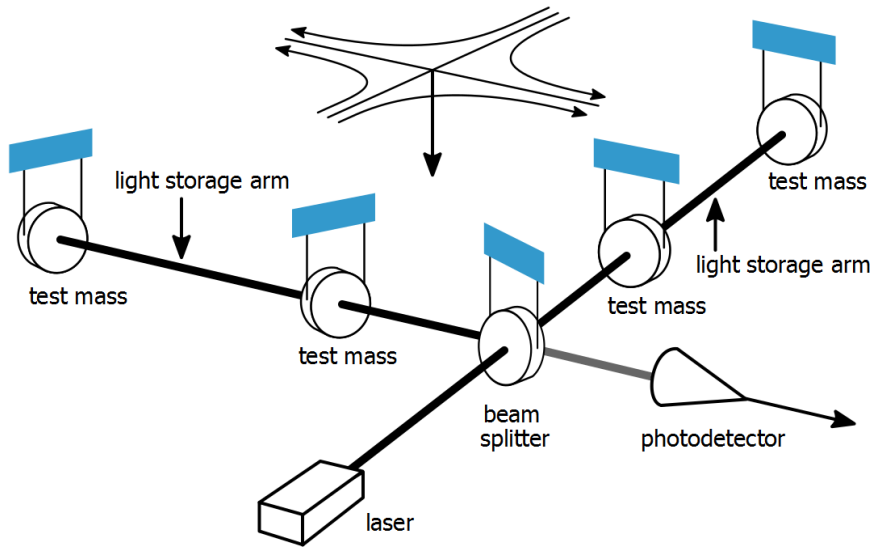


Figure 1.5 A schematic diagram of a laser interferometer. (From Ref. [29]).

signal of GW150914. The first direct observation of the GW signal is a milestone event for astrophysics.

Subsequently, LIGO successively announced other detected GW events. This thesis analyzes the GW events published by LIGO before 2019, namely GW151012^[31], GW151226^[32], GW170104^[33], GW170608^[34], GW170814^[35], GW170817^[36]. Table 1.1 lists a summary of source parameters for all the GWs. It is noted that most GWs were generated by the BH mergers, while the NS mergers generated GW170817.

Table 1.1 Summary of GWs observed by the LIGO experiment. The masses of BH or NS are given in the source frame. M1 represents the primary mass of BH or NS, and M2 represents the secondary mass of BH or NS. D_{LIGO} represents the luminosity distance.

GW type	UTC time	M1	M2	D_{LIGO}
GW150914	2015.09.14 09:50:45	$36^{+5}_{-4} M_{\odot}$	$29^{+4}_{-4} M_{\odot}$	410^{+160}_{-180} Mpc
GW151012	2015.10.12 09:54:43	$23^{+18}_{-6.0} M_{\odot}$	$13^{+4}_{-5} M_{\odot}$	1100^{+500}_{-500} Mpc
GW151226	2015.12.26 03:38:53	$14.2^{+8.3}_{-3.7} M_{\odot}$	$7.5^{+2.3}_{-2.3} M_{\odot}$	440^{+180}_{-190} Mpc
GW170104	2017.01.04 10:11:58	$31.2^{+8.4}_{-6.0} M_{\odot}$	$19.4^{+5.3}_{-5.9} M_{\odot}$	880^{+450}_{-390} Mpc
GW170608	2017.06.08 02:01:16	$12^{+7.0}_{-2.0} M_{\odot}$	$7^{+2.0}_{-2.0} M_{\odot}$	340^{+140}_{-140} Mpc
GW170814	2017.08.14 10:30:43	$30.5^{+5.7}_{-3.0} M_{\odot}$	$25.3^{+2.8}_{-4.2} M_{\odot}$	540^{+130}_{-210} Mpc
GW170817	2017.08.17 12:41:04	$1.36 - 1.60 M_{\odot}$	$1.17 - 1.60 M_{\odot}$	40^{+8}_{-14} Mpc

1.2.2 Neutrino production

Historically, the first multi-messenger detection of extra-solar occurred with SN1987A^[37] and referred to a broad spectrum of electromagnetic signals and neutrinos

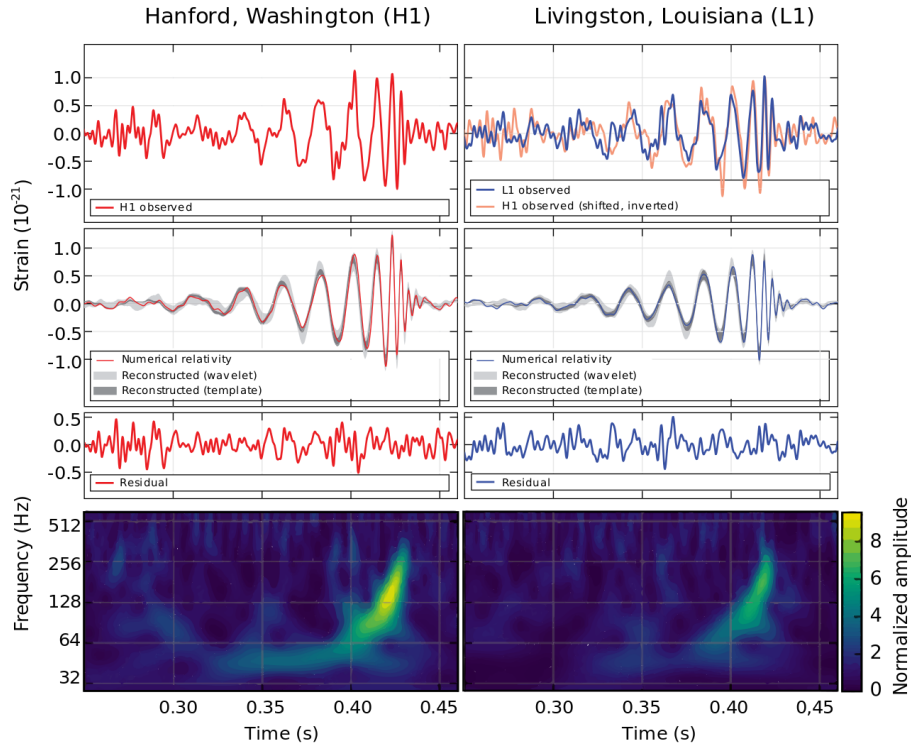


Figure 1.6 GW150914 signal from a binary BH merges observed at Hanford, Washington (H1, left column panels) and Livingston, Louisiana (L1, right column panels). The origin of x-axis is the time detected. The top two panels show that the GW signal was first detected by L1, and then by H1. The second row shows the GW signal spectrum predicted by different models. The third row shows the Residuals after subtracting the filtered numerical relativity waveform from the filtered detector time series. The bottom row shows that the signal frequency over time. (From Ref. ^[30]).

that were detected by Kamiokande^[6-7], IMB^[8-9], and Baksan^[10-11] with the neutrino energy ~ 20 MeV. With the direct observation of GWs, the astrophysicists expect to know more about the mechanism of GWs in conjunction with other detection methods. Neutrinos, as messengers of astrophysical events, have their advantages. Neutrinos could reveal the information from the hidden region of BH mergers because of their weak interaction with matter and null interaction with electromagnetic radiation. As neutrinos can travel almost unchanged from sources to detectors, they represent the invaluable messengers to bring a snapshot of the source at production.

After the GW150914 event, a weak GRB was found coincidentally 0.4 s by the Fermi Gamma-ray Burst Monitor^[38], although this GRB has a significant uncertainty astrophysics origin. The detection of GW170817 with a GRB170817A, detected by Fermi-GBR 1.7s after the coalescence, corroborates the hypothesis of a neutron star merger and provides the first direct evidence of a link between these merges and short GRB. The ex-

istence of GRB indicates that the accretion disk is likely to surround the merged object, which is the source of MeV neutrinos.

The main process of generating neutrinos in the accretion disk is



For the BH, the center of an accretion disk with a rapid accretion rate has a high enough temperature to trap neutrinos^[39]. After neutrinos are trapped, the gravitational binding energy loss rate is determined by the time which the neutrinos scatter out of the trapped region. For the low accretion rates, e.g., $\dot{m} = 0.1 M_\odot/s$ (M_\odot : solar mass), neutrinos are barely trapped. When the neutrinos are not trapped, the rate of energy loss is related to neutrino production. If the BH mass is $3 M_\odot$, a roughly 20% energy is released in the form of neutrinos for $\dot{m} = 1.0 M_\odot/s$ and 5% for $\dot{m} = 0.1 M_\odot/s$. Figure 1.7 shows the neutrino flux spectra of different accretion disk rates. The spectrum of neutrinos is below 100 MeV, which is the interesting energy range at Daya Bay. We expect to find the GW-related neutrino candidates at Daya Bay and provide a comprehensive understanding of the universe.

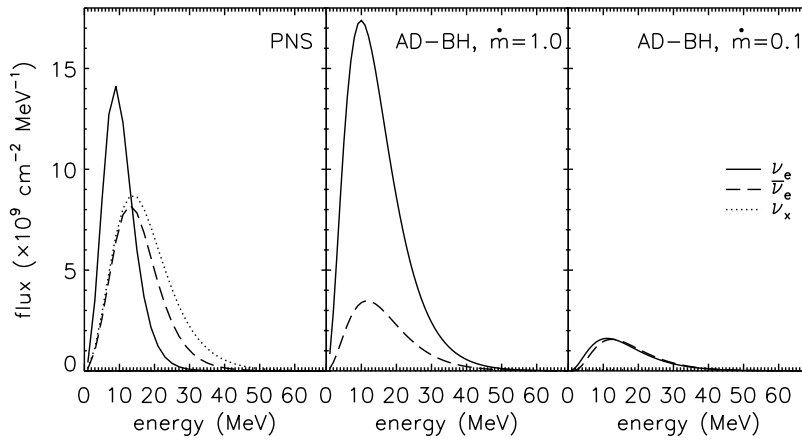


Figure 1.7 Neutrino spectra for the proton-neutron stars (PNS) and the accretion disk of black holes (AD-BH) without the oscillation. The \dot{m} represents the accretion rates. (From Ref.^[39]).

1.2.3 Related searches and experiments

Recently, many neutrino experiments have started the search for GW-related neutrinos.

ANTARES and IceCube^[40] had searched for high-energy (above ~ 100 GeV) neutrino signals in a time window of ± 500 s relative to GW150914. They found that the co-

incident neutrino signals were three and zero for IceCube and ANTARES, respectively. These results are consistent with the expected atmospheric background levels. Finally, ANTARES and IceCube announced that no neutrino signal observed from GW150914.

KamLAND^[41] presented the low-energy search results (below ~ 111 MeV) neutrino signals in a time window of ± 500 s. They investigated the neutrinos that coincided with GW150914, GW151012, and GW151226, and found no evidence.

Super-Kamiokande^[42] reported that the search results of neutrino signals coincided with GW150914, GW151012, and GW151226 within the neutrino energy from 3.5 MeV to 100 PeV. The search time window was ± 500 s around the GW detection time. They observed four neutrino candidates for GW150914 but found no candidates for GW151226. The neutrino candidates relative to GW150914 indicated that they were consistent with the expected background events. GW170817 was the first detected NS merger, but Super-K published the null search result of GW170817-related neutrinos^[43].

Borexino^[44] focused on searching the neutrino signals in the lower energy range (> 250 keV), which were coincident with GW150914, GW151226, and GW170104. They found that the search results were consistent with the expected solar neutrinos and background events.

1.3 Gamma-Ray bursts

GRBs are the phenomenon of instant brightening of gamma-ray bands from the universe. The energy is released between 10^{48} ergs and 10^{55} ergs if isotropic, lighting up the entire universe. They are the most energetic explosions in the universe^[45]. Figure 1.8 shows the visual effect of GRB when people see it naked^[46]. Satellite Vela first discovered GRB in 1967, and then a total of 16 GRBs were first published by Klebesadel in 1973^[47], marking the beginning of GRB research.

1.3.1 GRB phenomenology

After several decades of observation with γ -ray/X-ray satellites (BeppoSAX, KONUS/Wind, HETE-2, Swift, Integral, AGILE, and Fermi) and the follow-up carried out by ground-based optical, IR, mm, and radio, our understanding of GRBs has improved enormously. At the beginning of GRB research, the astrophysicists concluded that such high-energy events should occur in the Milky Way. In 1991, the Burst And Transient Source Experiment (BATSE) started operation, and data acquisition^[48]. Figure 1.9 shows

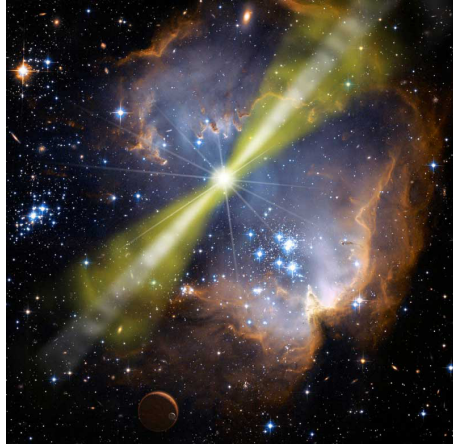


Figure 1.8 “naked-eye” GRB generated in artist’s concept. The observation shows two jets in opposite directions from the center. (white and green beams). (From Ref.^[46]).

the spatial locations where the BATSE observed a total of 2704 GRBs. It is observed that GRBs distribute uniformly in space but have no cluster on the plane where the Milky Way is located. It is believed that GRBs could be produced in the extra-galactic space, and the released energy is also underestimated.

In 1997, the BeppoSAX experiment started operation and was dedicated to observing the GRBs in the extra-galactic space and first found the GRBs’ afterglow effect. After the prompt gamma-ray signal, the afterglow follows and lasts up to several days. The discovery of afterglows can provide a higher precision measurement of GRB locations.

After decades of observation, the mechanisms of GRBs are still unclear. GRBs are roughly divided into two categories according to the duration time of bursts. Figure 1.10 shows the duration time of GRBs observed by BASTE. The definition of T_{90} is the time with the interval between 5% and 95% of the total fluence. There are two peaks, one is at 0.3 s, and the other is at 30 s. The T_{90} corresponding to the two-peak separation is about 2 s. When the $T_{90} > 2$ s, The GRB is called the long GRB. Otherwise, it is called the short GRB.

The bimodal structure of GRB during time T_{90} is thought to be caused by different GRB mechanisms corresponding to center engine models of long GRB and short GRB. Long GRBs originate from the core collapse of supernovae and have been observed with Type Ic supernovae^[51]. Compact binary mergers, such as NS-NS or NS-BH, generate short GRBs. For long GRBs and short GRBs, matter accumulates quickly on the stars’ surface and releases as relativistic jets of particles.

Observationally, the prompt emission phase of a GRB provides the temporal profile. The observed time profiles of GRBs have various shapes and duration times. The

2704 BATSE Gamma-Ray Bursts

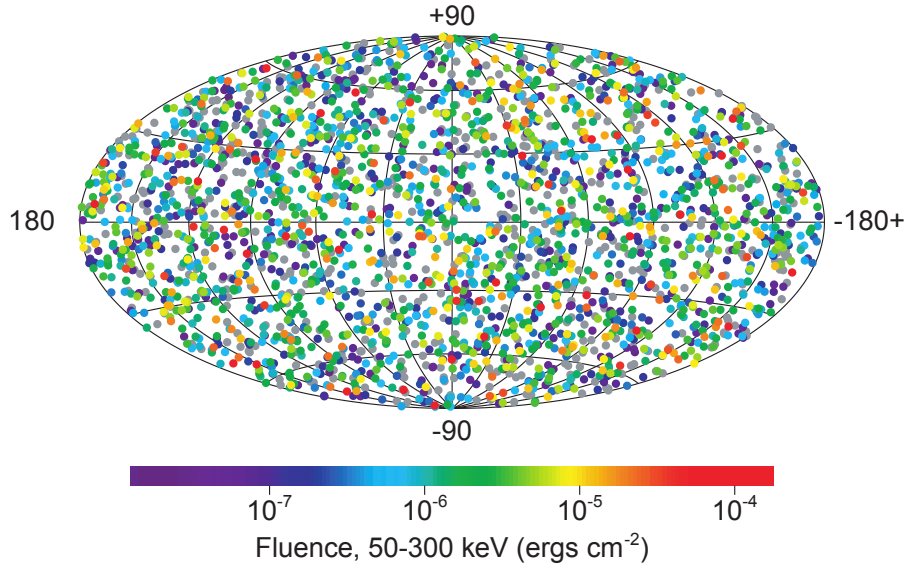


Figure 1.9 Positions of all the GRBs detected by BASTE on the sky. The shade of color represents the difference in fluence. The horizontal central axis of the picture represents the Milky Way. The distribution of GRBs is isotropic in the universe^[49].

observed time profile for the 20% GRBs is smooth. It is a typical Fast Rise Exponential Decay (FRED), which describes that the rise time is shorter than the decay time. The rest 80% of GRBs have rich substructures from single, double to multiple peaks. Figure 1.11 shows some GRB examples of the time profile observed by BATSE^[52].

The photon energy spectrum of GRB is non-thermal. The energy of photons released by GRBs is mainly in the energy of 50 - 1000 keV, and the peak is around a few hundred keV. However, there are many GRBs with a high-energy tail that can reach ~ 18 GeV^[53]. A semi-empirical BAND function^[52] using a double power-law joined smoothly to fit the typically GRB spectra.

$$F_{\gamma} = \epsilon_{\gamma} \frac{dn_{\gamma}}{d\epsilon_{\gamma}} = \begin{cases} A(\epsilon_{\gamma}/100)^{-\alpha} \exp\left(-\epsilon_{\gamma}(2-\alpha)/\epsilon_{\gamma,peak}\right) & \epsilon_{\gamma} \leq \epsilon_{\gamma,Break} \\ A\{(-\alpha + \beta)\epsilon_{\gamma,peak}/[100(2-\alpha)]\}^{\beta-\alpha} \exp(\alpha - \beta)(\epsilon_{\gamma}/100)^{-\beta} & \epsilon_{\gamma} > \epsilon_{\gamma,Break}, \end{cases} \quad (1-3)$$

where $\epsilon_{\gamma,Break} = (\beta - \alpha)\epsilon_{\gamma,peak}/(2 - \alpha)$. A is the amplitude in the unit of $s^{-1}cm^{-2}keV^{-1}$. α is the index of low energy spectra. β is the index of high energy spectra. “peak” energy is

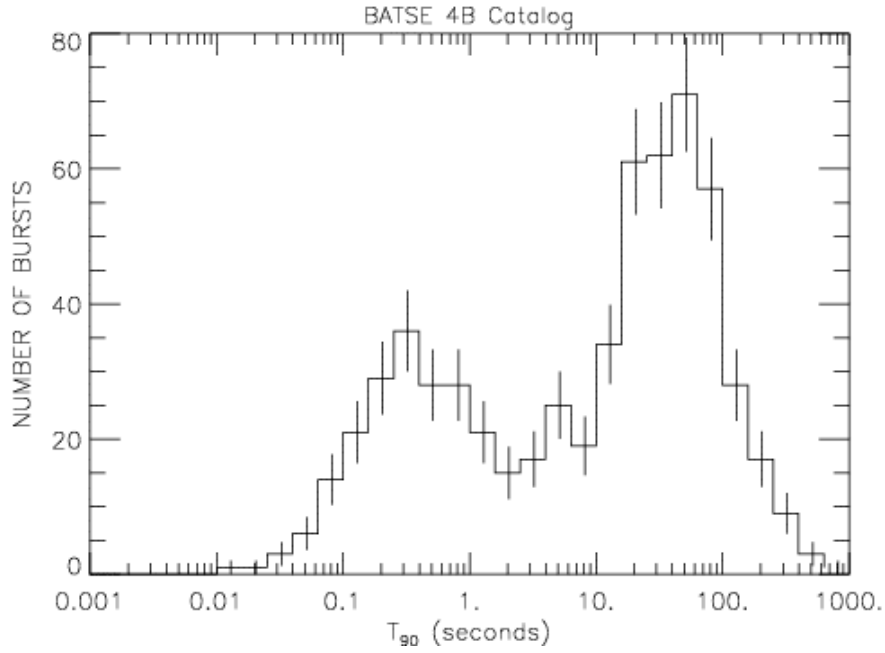


Figure 1.10 Duration time T_{90} distribution of GRBs detected by BATSE^[50].

the maximum energy in the $\epsilon_\gamma dn_\gamma/d\epsilon_\gamma$. The BAND function is approximated as follows,

$$F_\gamma = \epsilon_\gamma \frac{dn_\gamma}{d\epsilon_\gamma} \propto \begin{cases} \epsilon_\gamma^{-\alpha} & \epsilon \leq \epsilon_{\gamma, Break} \\ \epsilon_\gamma^{-\beta} & \epsilon > \epsilon_{\gamma, Break} \end{cases} \quad (1-4)$$

The breaking energy for most GRBs is the ranges between 100 keV and 400 keV. A typical break energy $\epsilon_{\gamma, Break} \approx 250$ keV, and the typical values for α and β are from 0 to 1.5 and 2, respectively. The results show that the energy spectra become soften with time, which explains the observed phenomenon that short GRB spectra are more rigid than long GRB spectra. Figure 1.12 shows the fitting of the GRB typical prompt spectrum^[54].

1.3.2 Neutrino production

When the GRB occurs and releases the energy up to $\sim 10^{53}$ ergs, whether neutrinos are the primary form to carry out most of the released energy has been an active research frontier. The predicted fluence of neutrinos is dependent on the models of the GRB's central engine. There are two models accepted by astrophysicists: the ultra-relativistic fireballs^[55] and the cosmic string^[56]. Both models could explain some aspects of the astronomical phenomena observed in GRB. We will describe two cosmological scenarios^[57] in detail below and give the predicted MeV-scale neutrino fluences depending on two models, respectively.

1) The relativistic fireball scenarios.

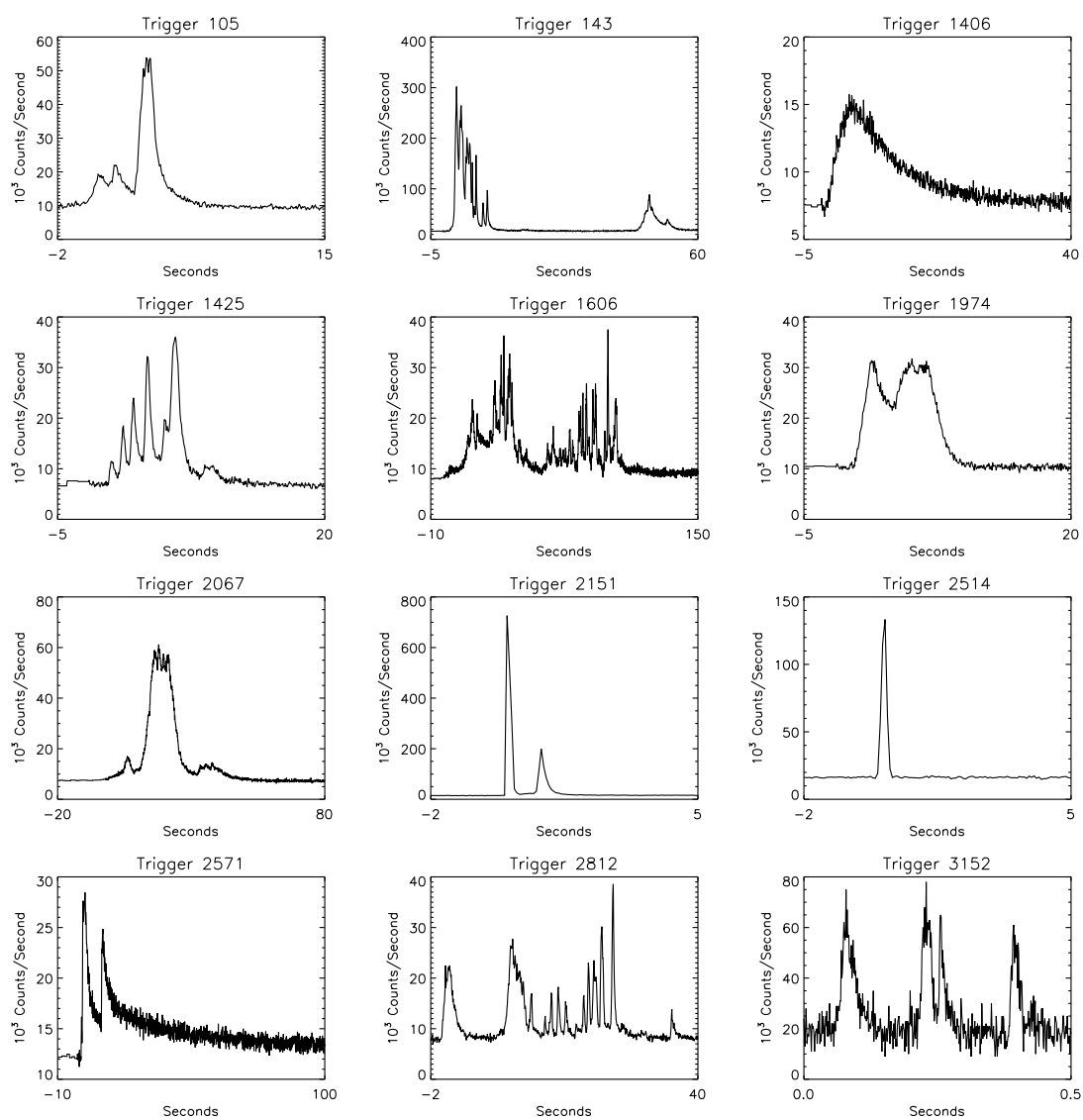


Figure 1.11 Time profile of GRB examples observed by BATSE. (From Ref. [52]).

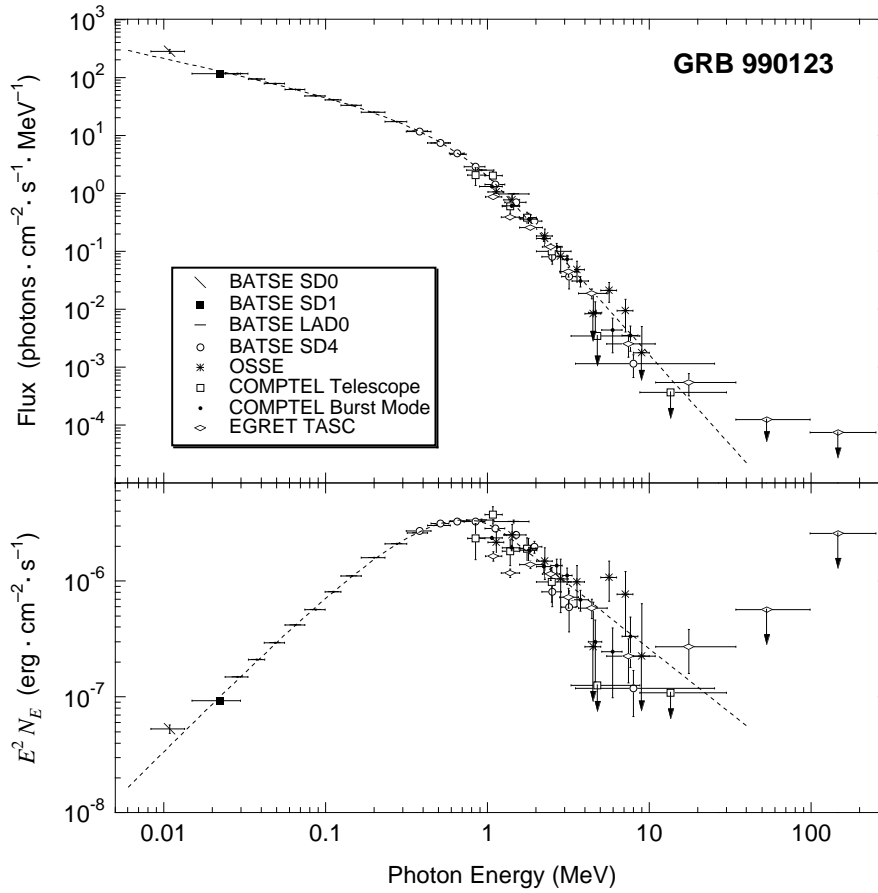


Figure 1.12 Fitting results of GRB 990123 spectra, and top panel displays the photon flux and the bottom panel displays the energy flux. (From Ref. [54]).

A relativistic fireball model can explain the generation of GRBs^[58-59]. The observed afterglow of GRBs confirmed the correctness of the fireball model^[60-61]. As shown in Fig. 1.13, the internal shells interact with the external shells when the fireball expands. This process generates γ -rays and neutrinos. The γ -rays are only released when the optical depth of the fireball sufficiently reduces. However, neutrinos could escape from the fireball, which is opaque to photons.

Different physical processes can produce high-energy neutrinos ($10^{14} \sim 10^{19}$ eV or higher)^[62-65] and MeV-scale neutrinos^[66]. When the external shells interact with the medium in the universe, the processes below could generate high energy neutrino^[67]:

$$p + \gamma \rightarrow (\Delta^+ \rightarrow) \begin{cases} n + \pi^+ \rightarrow n\mu^+\nu_\mu \rightarrow n + e^+ + \nu_e + \bar{\nu}_\mu + \nu_\mu, & \text{fraction } 1/3 \\ p + \pi^0 \rightarrow p\gamma\gamma, & \text{fraction } 2/3. \end{cases} \quad (1-5)$$

MeV-scale neutrino is the energy region of interest in the Daya Bay experiment. We

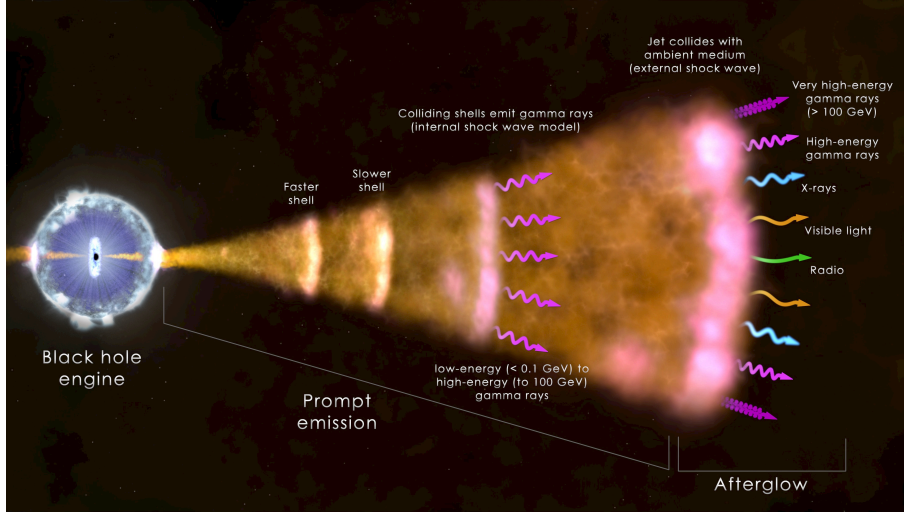


Figure 1.13 Cartoon schematic of a GRB generated from the relativistic fireball. When the internal shells collide with the external shells, γ -rays and neutrinos are generated. As the external shells expand outward, they collide with the medium and then produce γ -rays, Optical, Radio, X-rays, and high-energy neutrinos. Credit: NASA.

estimated the neutrino fluence under the fireball model. The main processes generate the MeV-scale neutrinos as follows (for $l = e, \tau, \mu$),

- Electron-positron annihilation: $e^+ + e^- \rightarrow \nu_l + \bar{\nu}_l$, as shown in Fig. 1.14.

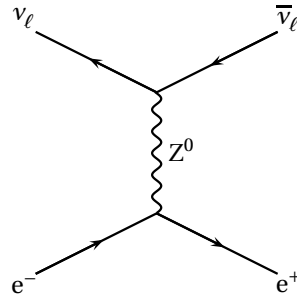


Figure 1.14 Feynman diagram for the process $e^- e^+ \rightarrow \nu_l \bar{\nu}_l$ ($l = e, \tau, \mu$).

- Electron captured on protons: $e^- + p \rightarrow n + \nu_e$.
- Positron captured on neutrons: $e^+ + n \rightarrow p + \bar{\nu}_e$.
- Nucleon-nucleon bremsstrahlung: $N + N \rightarrow N + N + \nu_l + \bar{\nu}_l$.

Ignoring the fireball model's complicated details, we can calculate the neutrino flux under a model assumption: a solar mass of neutrino energy 2×10^{53} ergs is released at a radius $R \approx 100$ km ball. The γ -rays energy is required when the γ fluency $F = 10^{-9} \text{ J} \cdot \text{m}^{-2}$ and the redshift $z = 1$.

$$E_\gamma = 2 \times 10^{51} \text{ erg} \left(\frac{D}{4000 \text{ Mpc}} \right)^2 \left(\frac{F}{10^{-9} \text{ J} \cdot \text{m}^{-2}} \right), \quad (1-6)$$

For the examples of neutron star merger, the neutrino energy released is 2×10^{53} ergs.

The neutrino energy in the fireball is $E_\nu \approx 10^2 E_\gamma$, as follows,

$$E_\nu = 65 \text{ MeV} \left(\frac{E_{\nu, \text{tot}}}{2 \times 10^{53} \text{ erg}} \right)^{1/4} \left(\frac{100 \text{ km}}{R} \right)^{3/4}, \quad (1-7)$$

where R is the fireball radius. Finally, the neutrino fluence is concluded from $E_{\nu, \text{tot}}/(4\pi D^2)$,

$$\Phi_\nu = \left(\frac{E_{\nu, \text{tot}}}{2 \times 10^{53} \text{ erg}} \right) \left(\frac{65 \text{ MeV}}{E_\nu} \right) \left(\frac{4000 \text{ Mpc}}{D} \right)^2 \text{ cm}^{-2}, \quad (1-8)$$

where $E_{\nu, \text{tot}}$ is the total neutrino energy released in the fireball, E_ν is the average neutrino energy, D is the distance to the source. In the Super-K experiment, Φ_ν is estimated to be 1.4 cm^{-2} from a single GRB assuming an E^{-2} neutrino spectrum with a typical value of redshift $z = 1$ (luminosity distance $\sim 5928.2 \text{ Mpc}$)^[68].

In a typical kiloton liquid scintillator (C_nH_{2n}) detector, there are about 8.6×10^{31} protons. The IBD cross-section at first-order^[69] is

$$\sigma_{\text{IBD}} = 9.42 \times 10^{-44} \text{ cm}^2 (E_\nu/\text{MeV} - 1.3)^2. \quad (1-9)$$

We convoluted a neutrino energy spectrum E^{-2} with the average energy $\langle E_{\bar{\nu}_e} \rangle = 12 \text{ MeV}$, the IBD cross-section, and the target proton numbers, obtaining an estimated number of neutrinos N from the GRB fire-ball model below,

$$N = 1190 \times \frac{L_{\bar{\nu}_e}}{2 \times 10^{53} \text{ erg}} \times \left(\frac{10 \text{ kpc}}{D_L} \right)^2 \times \frac{T_M}{1 \text{ kt}}, \quad (1-10)$$

where D_L is the distance, while T_M is the target mass. From Eq. (1-10), one can conclude that if a GRB occurs in the Milky Way Galaxy, the number of neutrinos will be enormous.

2) The cosmic string-type scenarios.

Another scenario is the cosmic string, which successfully explains some aspects of the GRB, especially for the high-redshift GRBs. The high-redshift GRBs release the high energy but have short durations. Furthermore, the high-redshift GRBs' rate is higher than the predicted by the collapsar model with an ordinary star formation rate. Compared to the relativistic fireball model, the neutrino fluence predicted by the cosmic string model is more significant. The neutrino fluence is as follows,

$$\Phi_\nu = 10^8 \left(\frac{\eta_\nu}{10^{-10}} \right)^{-1} \left(\frac{E_\nu}{100 \text{ MeV}} \right)^{-1} \left(\frac{F_\gamma}{10^{-6} \text{ erg} \cdot \text{cm}^{-2}} \right) \text{ cm}^{-2}, \quad (1-11)$$

where η_ν is the ratio of γ -rays energy to the neutrino energy, E_ν is the neutrino energy observed, and F_γ is the photon fluence. The tens MeV neutrino fluence of a typical GRB is estimated about $(10^7 - 10^8) \text{ cm}^{-2}$. We estimated the number of neutrinos N from the GRB cosmic string model,

$$N = 1.8 \times 10^6 \times \left(\frac{\eta_\nu}{10^{-10}}\right)^{-1} \times \frac{L_{\bar{\nu}_e}}{2 \times 10^{53} \text{ erg}} \times \left(\frac{1 \text{ Mpc}}{D_L}\right)^2 \times \frac{T_M}{1 \text{ kt}}, \quad (1-12)$$

where D_L is the distance, while T_M is the target mass.

1.3.3 Previous experimental searches

Figure 1.15 summarizes the upper limits of $\bar{\nu}_e$ fluence in the low-energy region by several major neutrino experiments^[70].

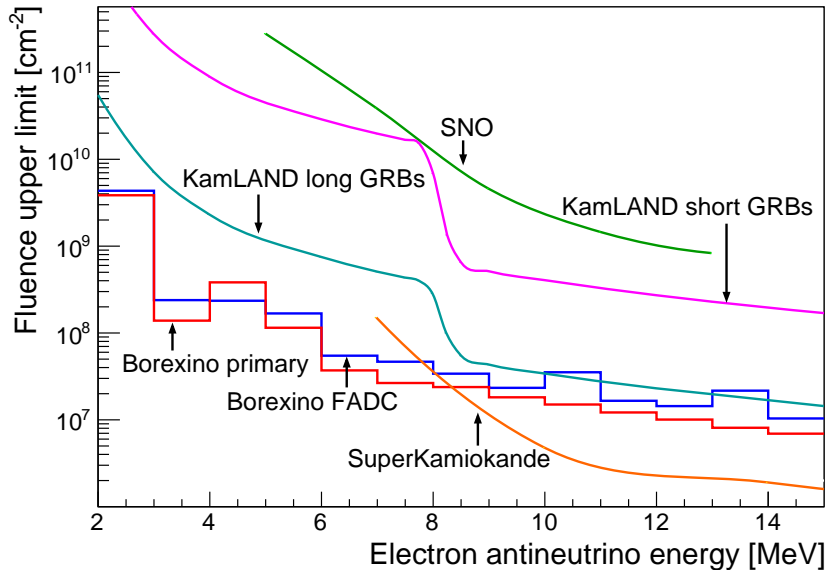


Figure 1.15 Upper limits of $\bar{\nu}_e$ from GRBs versus MeV neutrino energy. (From Ref.^[70]).

Super-Kamiokande^[68] analyzed 1454 GRBs observed by the BATSE experiment from April 1996 to May 2000. The neutrino energy range of searching was from 7 MeV to 100 TeV. There were no neutrino signal candidates observed with more than the expected background fluctuations associated with GRBs, yielding upper limits at 90% confidence level.

SNO^[71] searched for the neutrino energy below 20 MeV, associated with a total of 190 GRBs taken from Swift satellite. They concluded that there were no correlations between the neutrino candidates observed in SNO and the GRB sources.

KamLAND^[72] analyzed the GRBs, which split into two periods because of the reac-

tor switch. They searched prompt energy of $\bar{\nu}_e$ from 7.5 MeV to 100 MeV, associated with 192 GRBs in the first period from August 2002 to September 2011, and from 0.9 MeV to 100 MeV with a total of 39 GRBs in the second period. The neutrino signal candidates associated with GRBs were consistent with the expected background levels. Finally, they gave the upper limits of $\bar{\nu}_e$ fluence.

Borexino^[70] searched for the neutrinos and anti-neutrino with energy between 1.8 MeV and 15 MeV for a total of 2350 GRBs from December 2007 to November 2015. The neutrino signals were consistent with the background levels. They also gave the upper limits based on the experimental sensitivity.

IceCube^[73] and ANTARES^[74-75] searched for the high-energy (TeV - PeV) neutrino associated with a total of 1172 GRBs and 336 GRBs, respectively. Both experiments found no neutrino signals correlated with the GRB sources, giving the corresponding upper limits.

1.4 Thesis organization

Chapter 1 gives a brief introduction of the SM, the development history of neutrinos, and various neutrino sources and their energy distributions. It then introduces GW physics and the history of observation, listing the LIGO GW events associated with neutrinos at the Daya Bay experiment. Finally, it discusses GRB's observed physical properties, model-dependent neutrino emission mechanisms, and associated neutrinos' searches in other neutrino experiments.

Chapter 2 gives a brief introduction to the Daya Bay reactor neutrino experiment. The physical goals and significance are listed. We also introduce the design schemes of the experiment, the detector, and the subsystems. We also present the research process of the Daya Bay experiment and the experimental operation status.

Chapter 3 focuses on the studies of neutrino energy and the method of neutrino fluence calculation.

Chapter 4 introduces the simulation studies. We first study the IBD cross-section in the simulation generator. And then, we study the neutron simulation in different Geant4 versions. In the end, we introduce the simulation package at Daya Bay and provide the studies of high-energy neutrino (tens MeV) simulation in the detector.

Chapter 5 introduces the IBD events selection criteria and the detector efficiency under two energy spectra, namely monochromatic spectra and Fermi-Dirac spectrum.

Chapter 6 introduces the GW data analysis. We first verify the correctness of the analysis approach and then construct a likelihood function to calculate the upper limit of neutrino fluence. We present GW-associated neutrinos' search results, search time windows, background estimation, neutrino candidates, and signal significance. Finally, we give the $\bar{\nu}_e$ fluence associated with GW events.

Chapter 7 introduces the GRB data analysis. We present the search results of GRB-related neutrinos, GRB data samples, search time windows, background estimation, neutrino candidates. Finally, we give the upper limits of GRB-related neutrino fluence.

Chapter 8 summarizes the analysis of searching for neutrinos from GWs or GRBs and gives the prospect of this research.

Chapter 2 The Daya Bay reactor neutrino experiment

The Daya Bay Reactor Neutrino Experiment^[76] is one of the new generation reactor neutrino experiments. The physical goal is to accurately measure $\sin^2 2\theta_{13}$ (sensitivity can reach 0.01) at a 90% confidence level after three years of data accumulation. In March 2012, the Daya Bay experimental collaboration first reported that $\sin^2 2\theta_{13}$ was non-zero at 5.2σ , and its central value was $\sin^2 2\theta_{13} = 0.092 \pm 0.016$ (stat.) ± 0.005 (syst.)^[77]. In addition to the leading measurements of $\sin^2 2\theta_{13}$ and Δm_{32}^2 , other physical topics were also studied, such as the search for light sterile neutrinos^[78-80], the measurement of anti-neutrino spectrum^[81-82], and the IBD yields from the primary fissionable isotopes in the reactor fuel^[83].

This chapter introduces the Daya Bay reactor neutrino experiment, including the significance of the measurement of θ_{13} , the layout of the experiment, the design of the anti-neutrino detector (AD), the subsystem of the detector, and the data taking.

2.1 Physical significance

Before the Daya Bay experiment, a few parameters correlated to the neutrino oscillation phenomenon still need further measurement, which consists of the signs of Δm_{32}^2 , $\sin^2 2\theta_{13}$, and δ . In particular, the conjugation and parity violation (CPV) phase δ could explain the phenomenon of matter-antimatter asymmetry in the universe. The experimental physicists plan to build the long-baseline neutrino oscillation experiments utilizing ν_μ and $\bar{\nu}_\mu$ beams generated by the accelerator. They could measure CPV by comparing $\nu_\mu \rightarrow \nu_e$ and $\bar{\nu}_\mu \rightarrow \bar{\nu}_e$ oscillation probability. The long-baseline neutrino oscillation probability formula is as follows,

$$\begin{aligned}
 P_{\text{long-baseline}} \simeq & \sin^2 2\theta_{13} \sin^2 \theta_{23} \sin^2 \Delta \\
 & \pm \alpha \sin 2\theta_{13} \sin \delta_{CP} \cos \theta_{13} \sin 2\theta_{12} \sin 2\theta_{23} \sin^3 \Delta \\
 & + \alpha \sin 2\theta_{13} \cos \delta_{CP} \cos \theta_{13} \sin 2\theta_{12} \cos \Delta \sin^2 \Delta \\
 & + \alpha^2 \cos^2 \theta_{23} \sin^2 2\theta_{12} \sin^2 \Delta,
 \end{aligned} \tag{2-1}$$

where $\alpha = \Delta m_{21}^2 / \Delta m_{32}^2$, $\Delta = \Delta m_{31}^2 L / (4E_\nu)$. The second term's negative sign on the right side of the equation corresponds to the neutrino mode, and the positive sign corresponds to

the anti-neutrino mode. Equation (2-1) implies that the signs of Δm_{32}^2 and θ_{13} are required to determine the CPV in the oscillation probability. It is possible to reduce the matter effect by reducing the length of the baseline, which means to reduce the signs of Δm_{32}^2 's effect. In the meantime, the energy of the beam ensures that L/E is unchanged, guaranteeing the sensitivity to Δm_{32}^2 in the experiment. However, it is hard to reduce the impact brought by θ_{13} .

The measurement of δ is more difficult with the smaller value of $\sin^2 2\theta_{13}$. If its value is less than 0.01, the attempt to measure CPV is challenging by the existing experimental methods. Moreover, the next generation of the accelerator and detector technology is required. Therefore, the measurement of $\sin^2 2\theta_{13}$ at a 90% confidence level could reach a sensitivity of 0.01, which is of great significance in theoretical and experimental aspects. It will determine the development of the next generation of neutrino experiments. Besides, the neutrino oscillation is the only confirmed evidence beyond the SM. The accurate measurement of the $\sin^2 2\theta_{13}$ mixing angle can further identify the existence of new physics.

2.2 The design and layout

The physics goal of the Daya Bay neutrino experiment is to measure $\sin^2 2\theta_{13}$ to an accuracy of 0.01 or higher, which is better than an order of magnitude compared with the sensitivity in the CHOOZ neutrino experiment. Considering the individual layout of the reactor cores and utilizing the unique advantage of Daya Bay, the specific design of the experiment is as follows:

1. Significant statistics

The Daya Bay locates about 50 kilometers in the east of Shenzhen City and about 55 kilometers in the northeast of Hong Kong. Daya Bay Nuclear Power Plant (NPP) is about 1 km away from Ling Ao phase I NPP. There are four reactor cores, two for each NPP, and each reactor core's thermal power is 2.9 GW. In 2010 and 2011, two cores of Ling Ao phase II NPP began to run, and thermal powers were 2.9 GW each. The Daya Bay - Ling Ao phase I - Ling Ao phase II all operate with a total thermal power of 17.4 GW, making it be the second-largest reactor group in the world. Compared with competition experiments, such as RENO, the statistics of the anti-neutrino can be significantly improved.

2. Mountain shield

There are higher mountains next to reactor cores. These are 300 m to 500 m away from the reactor cores, and the mountains are as high as 100 m or more; It is about 400 m height at about 2 km (oscillation maximum) from the reactor cores. The mountain is composed of monolithic granite suitable for tunnel excavation and the establishment of an underground laboratory. All experimental halls (EH) are under the mountains. Figure 2.1^[84] shows each hall's overburden and the mountain's experimental elevation profile.

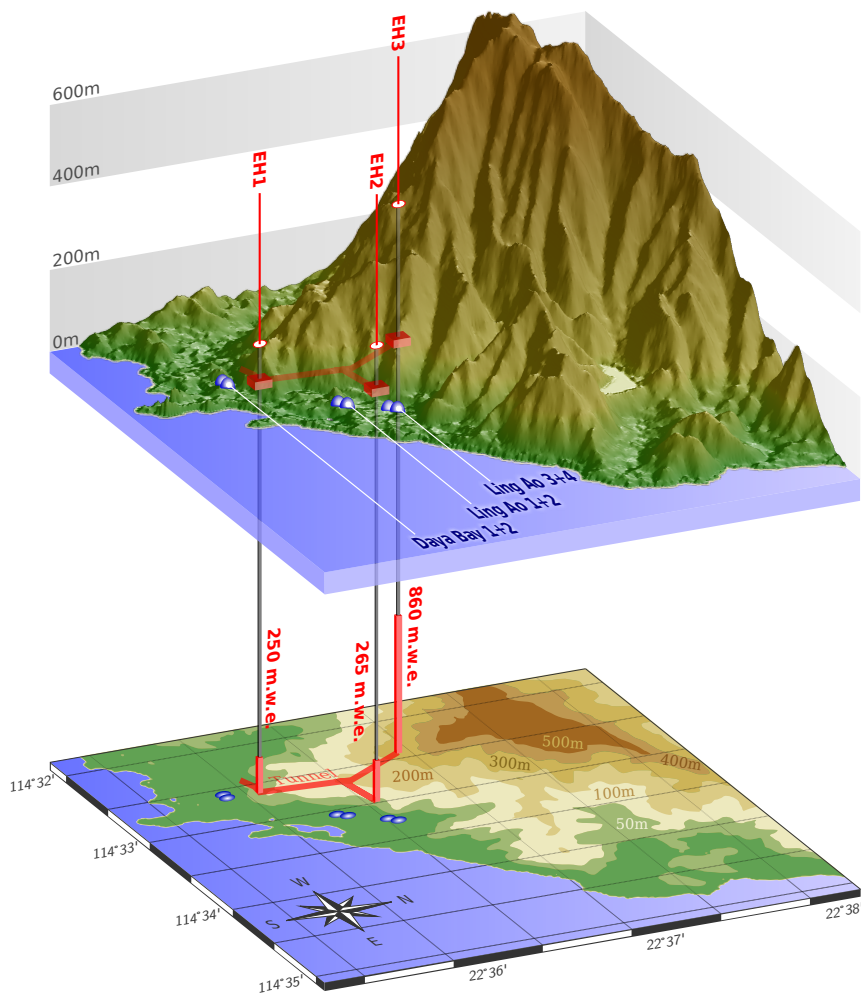


Figure 2.1 Elevation profile of the mountain above the experimental and the depth meter water equivalent (m.w.e.) of each hall. (From Ref.^[84]).

The overburden in each hall could reduce the muon flux of cosmic rays, reducing muon-induced spallation neutrons and short-lived isotopes that can mimic IBD events. The overburden depth, muon flux, and the average energy for each EH are summarized in Table 4.2^[85].

3. Near-far relative measurement

Table 2.1 Summary of the overburden, muon flux, and average energy for each EH. The muon flux and average energy are from simulation and the uncertainty of flux is about 10%. (Table data from Ref.^[85]).

EH	Overburden [m]	Overburden [m.w.e]	Muon rate [Hz/m ²]	\bar{E}_μ [GeV]
EH1	93	250	1.27	57
EH2	100	265	0.95	58
EH3	324	860	0.056	137

The reactor-related correlation error is about 2%. The Daya Bay experiment placed two detectors near the Daya Bay reactors and Ling Ao reactors as the near-site detectors and placed four detectors at the optimal baseline as the far-site detectors. Suppose we adopt the near-far relative measurement, design the identical detectors, and optimize the baseline. In that case, we will expect cancellations for the correlation error and most of the non-correlation errors of the reactors and the correlation errors between the detectors. Figure 2.2 shows the layout of detectors in Daya Bay.

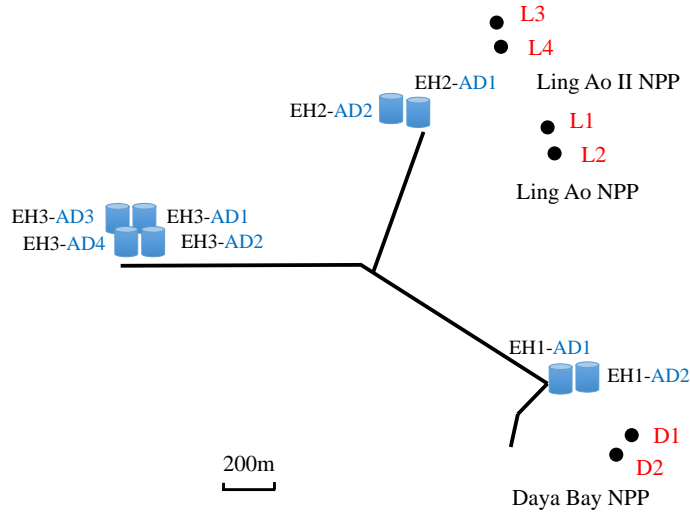


Figure 2.2 Layout of eight detectors and six reactor cores in the Daya Bay reactor neutrino experiment. The black line represents the tunnels that connect each EH. The red points stand for the reactor cores in each NNP. (From Ref.^[86]).

4. Optimal baseline selection

The reactor neutrino experiment measures the survival probability of $\bar{\nu}_e$ at the neu-

trino energy range of 1.8 MeV to 8 MeV at a distance of several hundred meters to several kilometers, ignoring the matter effect. The survival probability can be calculated as follows,

$$P_{\text{sur}} = 1 - P_{12} - P_{13} \quad (2-2)$$

$$\simeq 1 - \sin^2 2\theta_{12} \sin^2 \frac{\Delta m_{21}^2 L}{4E_\nu} - \sin^2 2\theta_{13} \sin^2 \frac{\Delta m_{31}^2 L}{4E_\nu}$$

Equation (2-2) implies that P_{13} is dominant when the baseline $L \simeq 2$ km and P_{12} will be dominant when the baseline $L \simeq 60$ km, which corresponds to the short-baseline neutrino experiment and long-baseline neutrino experiment, respectively. Figure 2.3 shows the relationship between the oscillation probability and the baseline length^[87], indicating that the first oscillation maximum is around 2 km. Table 2.2 summarizes the detailed baselines^[88] from the center of six reactor cores to eight detectors.

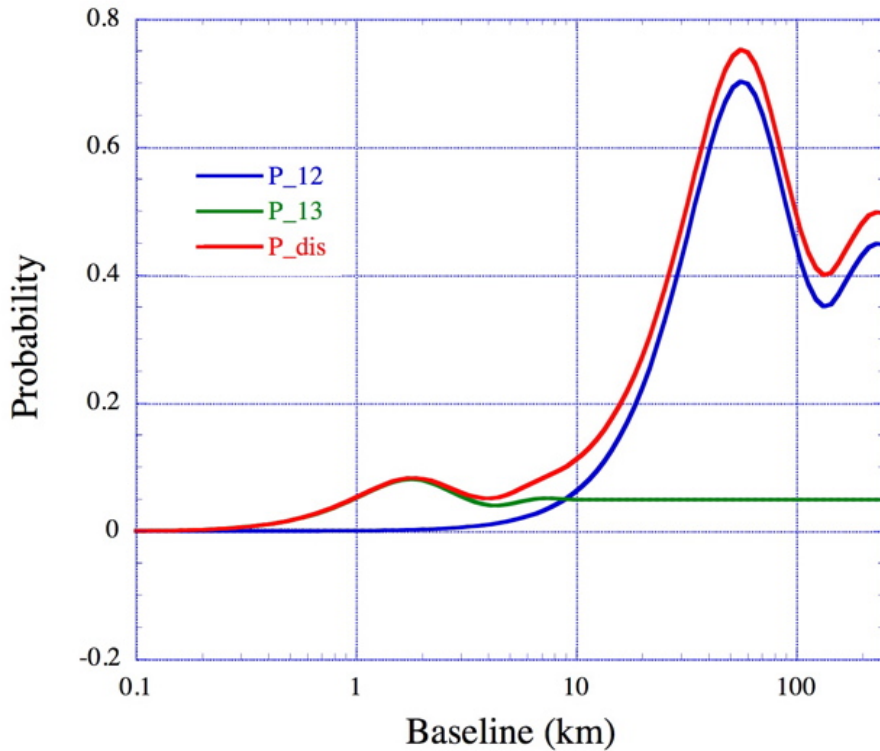


Figure 2.3 Reactor anti-neutrino disappear probability as a function of distance from the source. $P_{\text{dis}} = P_{12} + P_{13}$ is the total disappearance probability. (From Ref.^[87]).

4. Detector design

A three-layer concentric cylindrical structure is adopted to design the neutrino detector. The innermost layer is the target material of gadolinium-doped liquid scin-

Table 2.2 Detailed baselines from the center of six reactor cores to eight detectors. The distances are measured by the combination of station electronic theodolite and GPS with the precision of 18 mm. (Table data from Ref.^[88]).

Unit: m	D1	D2	L1	L2	L3	L4
EH1 AD1	362.38	371.76	903.47	817.16	1353.62	1265.32
EH1 AD2	357.94	368.41	903.35	816.90	1354.23	1265.89
EH2 AD1	1332.48	1358.15	467.57	489.58	557.58	499.21
EH2 AD2	1337.43	1362.88	472.97	495.35	558.71	501.07
EH3 AD1	1919.63	1894.34	1533.18	1533.63	1551.38	1524.94
EH3 AD2	1917.52	1891.98	1534.92	1535.03	1554.77	1528.05
EH3 AD3	1925.26	1899.86	1538.93	1539.47	1556.34	1530.08
EH3 AD4	1923.15	1897.51	1540.67	1540.87	1559.72	1533.18

tillator (GdLS), as a detection medium for neutrinos. The middle layer is the liquid scintillator (LS), which is used to collect photon energy and improves the neutron detection efficiency. The outermost layer is a protective layer of mineral oil (MO), shields the natural radioactive background from the photomultiplier tube (PMT), and the stainless steel vessel (SSV). The detector's detection threshold can get down to the lowest positron deposition energy, leading to about 100% of the positron selection efficiency. In the meantime, the detector's three-layer structure can clearly define the target mass and confine the IBD events in the central layer, which avoids the additional efficiency uncertainty brought by events by-point selection in the CHOOZ and KamLAND neutrino experiment.

5. Identical detector modules

Identical detectors in the near and far sites can cancel the correlation uncertainty of the detection efficiency. Furthermore, multiple detectors in the same EH can check each other.

2.3 Anti-neutrino detector

The Daya Bay reactor neutrino experiment detects $\bar{\nu}_e$ by the IBD interaction:



Fig. 2.4 shows whole process of the IBD reaction. The e^+ generated by the IBD interaction carries more than 99% of kinetic energy and then annihilates with e^- to generate two back to back γ 's of 0.511 MeV. Part of the e^+ 's will deposit their kinetic energy

that converts into other energies during the flight, so the γ 's total energy is greater than 2×0.511 MeV. This process lasts only a few nanoseconds, so it is called a prompt signal. The neutron is captured by Gd (nGd) or H (nH) after a typical time of about $28 \mu\text{s}$ in the GdLS region or $216 \mu\text{s}$ in the un-doped LS region and then released into a γ cascade with a total energy of about 8 MeV or a single 2.2 MeV γ , respectively. The signal captured by a neutron is called a delay signal. The coincident measurement of prompt and delay signals is effective for eliminating background and determining anti-neutrinos.

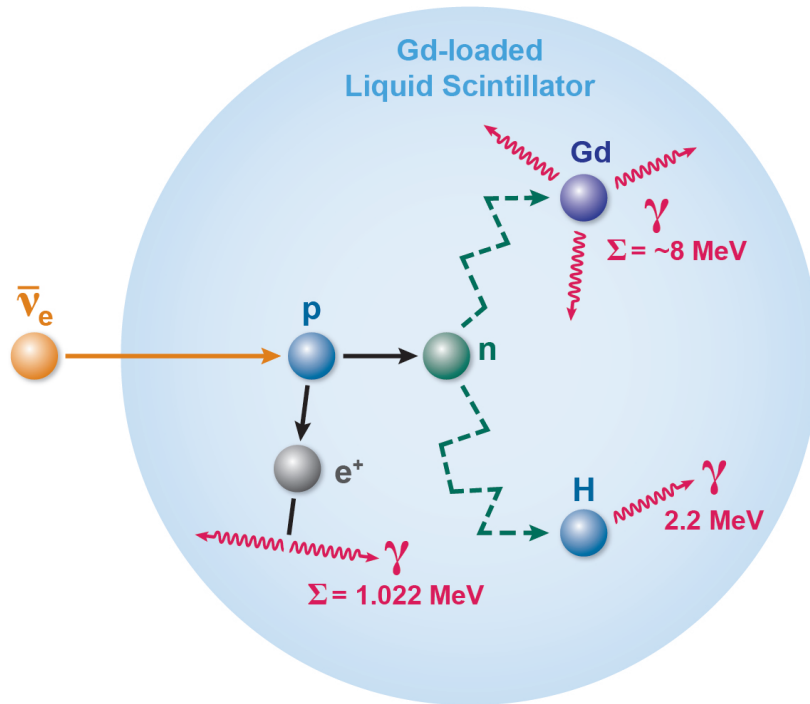


Figure 2.4 Diagram of prompt and delayed generation in IBD interaction. (From Ref.^[89]).

The Daya Bay reactor neutrino experiment has eight identical antineutrino detectors (ADs)^[86,88], and each AD consists of three layers of concentric cylinders, as shown in Fig. 2.5. There is 20 t of Gd-doped (0.1% by mass) liquid scintillator in an inner acrylic vessel (IAV) with a diameter and a height of 3 m used to detect $\bar{\nu}_e$. The middle layer contains a 22 t un-doped LS in an outer acrylic vessel (OAV) with a diameter and a height of 4 m to improve the tagging of γ 's that escape from the IAV. The outermost layer is 40 t of MO, packed in an SSV with a diameter and a height of 5 m, and used to shield the radioactive background from PMTs and SSV. All the LS were mixed in a vessel and then filled one by one. There are a total of 192 20-cm PMTs (Hamamatsu R5912) installed around the inner surface of the SSV by 24 columns \times 8 rings inside the MO volume.

Reflectors with highly reflective $> 98.5\%$ are placed on the top and bottom of the 4 m OAV instead of the PMTs installation. The two reflectors' material is ESR (Enhanced Specular Reflector, 3M[®]). This design increases the photocathode coverage by about 12% and reduces the number of PMTs by 50% without significantly lowering the energy and position resolution^[88].

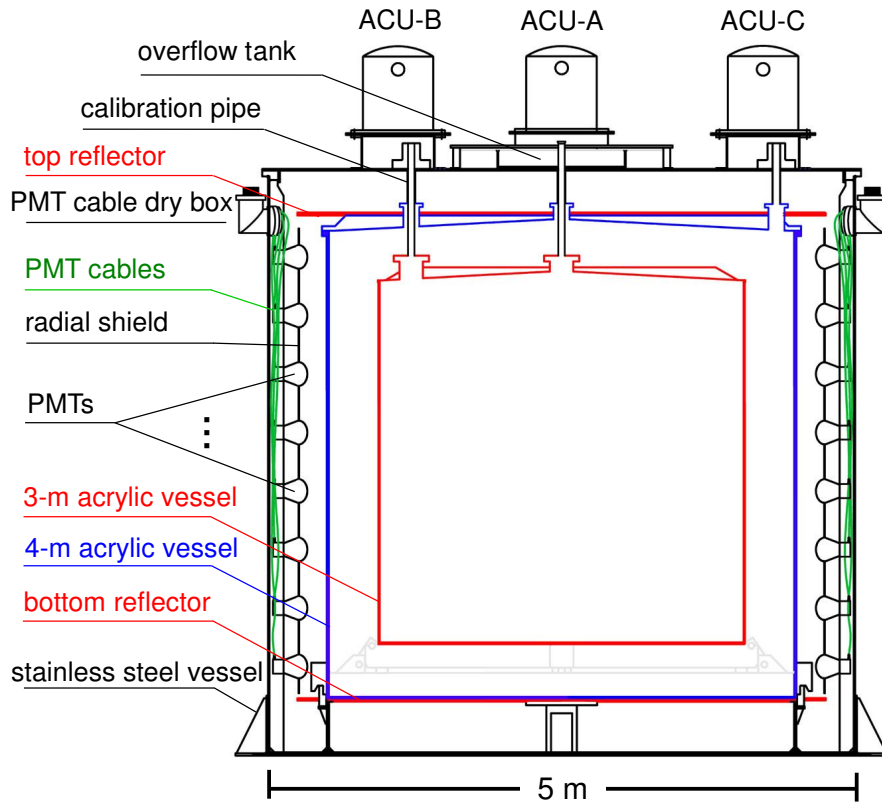


Figure 2.5 Schematic for a Daya Bay antineutrino detector. (From Ref.^[86]).

Three automatic calibration units (ACU) are installed on the top of the detector to calibrate the detector's energy response. The three ACUs locate the detector center, the edge of the GdLS ($R = 135$ cm), and the LS region ($R = 177$ cm). Each ACU contains several sets of calibration sources: LED (Light-Emitting Diode), $^{241}\text{Am} - ^{13}\text{C}$, ^{60}Co , and ^{68}Ge . Each source can be moved freely in the vertical direction.

2.4 Muon veto system

The background of the Daya Bay reactor neutrino experiment mainly comes from the cosmic rays muon (μ) and the secondary particles produced by the μ . The overburden in the lab serves as a passive shielding to this background. In the meantime, the surrounding rocks emit lots of γ 's and neutrons. Placing ADs in the water pool can reduce the γ flux

by 10^6 ^[88]. The water can also block most of the fast neutrons from surrounding rocks. Besides, the ultra-pure water separates the detectors from air to avoid the background caused by radon in the air.

The muon veto system consists of a water Cherenkov detector and an array of the RPC detector for each EH. Figure 2.6 illustrates the muon veto system in the near site, in which the two ADs are in a pool filled with 2000 t of ultra-pure water and separated by at least 1 m of water. Moreover, the distance between the ADs and the pool surface is at least 2.5 m. The near-site pool is an octagon with $16\text{ m} \times 10\text{ m} \times 10\text{ m}$ ensuring that no dead angles in the water circulation without sacrificing detection performance. The far-site pool is an octagon with $16\text{ m} \times 16\text{ m} \times 10\text{ m}$. The ultra-pure water pool is separated by the White Tyvek[®] sheets on the stainless steel frame structure, divided into the inner water shield (IWS) and the outer water shield (OWS). The OWS is 1-m thick. There are 288 of 20-cm PMTs in EH1, EH2, and 384 of 20-cm PMTs in EH3^[85] installed on the steel frame structure (PMT coverage rate 0.8%). The IWS and OWS not only serve as independent water Cherenkov detectors but also mutual detection performance. After a period of operation, the muon detection efficiency in IWS is $99.98 \pm 0.01\%$, and the muon detection efficiency in OWS is higher than 97% ^[85], which all exceed the pool design index of 95%.

The RPC that covers the water pool for each hall consists of $2\text{ m} \times 2\text{ m} \times 8\text{ cm}$ modules, which extend 1 m beyond the pool in all directions. Each RPC module is composed of four layers of RPC made from non-oiled Bakelite sheets^[90-91]. The four-layer RPC can reach a greater than 98% detection efficiency through a logical selection of three out of four. The reconstruction accuracy of the vertices of the muon passing through can reach 15 cm. The RPC detector and the Cherenkov detector $99.5\% \pm 0.25\%$ of the combined detector efficiency, which reaches the design requirement. The muon veto system composed of water Cherenkov detector and RPC detector could tag the muon events and removes the backgrounds induced by the muons.

2.5 Calibration and energy reconstruction

Event reconstruction needs calibrated energy and arrival time information from PMTs. Below is the description for the calibration of these two measurements.^[85,92]

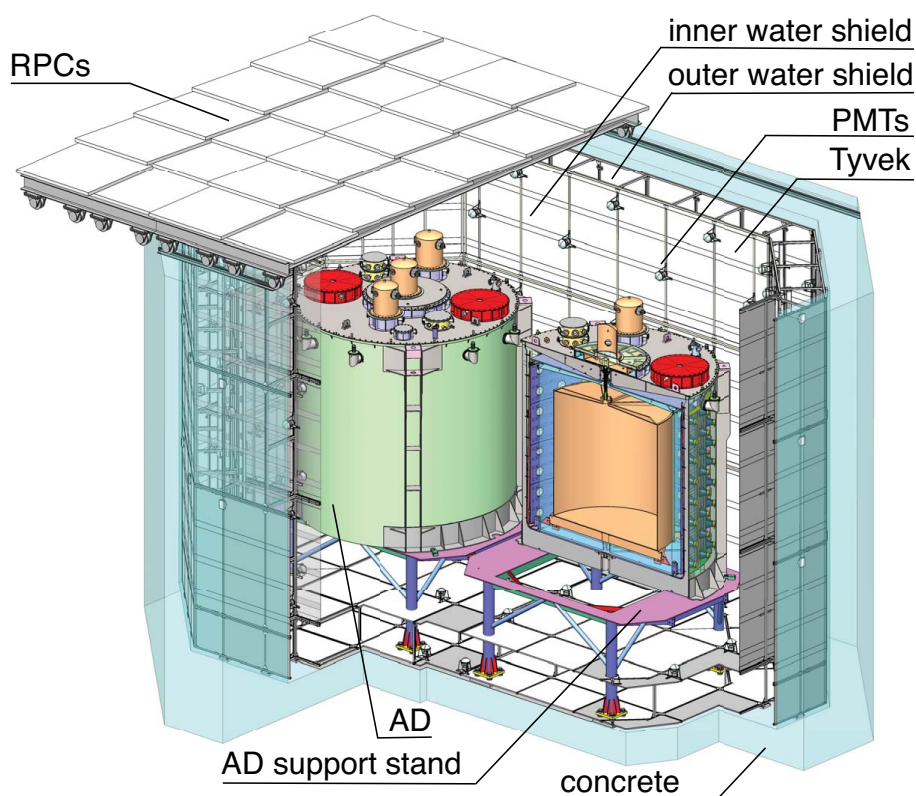


Figure 2.6 Structure of the Daya Bay reactor neutrino experiment in the near-site. It consists of the central detector, the water Cherenkov detectors, and the RPC detector. (From Ref.^[86]).

2.5.1 Time calibration

For each AD, the time accuracy for resolving two triggers was 25 ns. The LEDs were put in a single AD to calibrate the relative time response of PMTs. A light intensity function was applied to fit the time delays for LED-to-PMT distances, and then the fitting time was adopted to correct each channel (PMT). The time calibration was performed for each AD periodically.

2.5.2 Energy reconstruction

The ADC (Analog to Digital Converter) gain calibration was performed for each PMT channel and validated by two independent methods. One was to calibrate the detector using the low-intensity LED pulses. The other one was to calibrate the detector by fitting the single photoelectron peak using a Poisson-Gaussian convolution^[88] in the PMT dark noise spectrum.

Each detector's energy scale is the factor that converts photoelectrons to the energy (~ 170 PE/MeV). Two independent calibration sources verified the energy scale calibra-

tion. One was to scale by the 2.506 MeV gamma-ray peak of ^{60}Co at the detector center. The gamma source was deployed in the ACU A once a week. The other one was to use the muon-induced neutrons captured by two Gd isotopes ^{157}Gd and ^{155}Gd , which release γ -cascades of 7.94 MeV and 8.54 MeV, respectively.

This position reconstruction used charge-pattern templates derived from a Monte Carlo simulation^[86]. The average charge distribution in 192 PMTs was determined for $20 \times 20 \times 24$ divisions, corresponding to 9600 voxels in r^2 , z , and ϕ . The reconstruction should have the smallest χ^2 for each event to ensure the position of the event occurred. The resolution of 2.2 MeV γ was about 12 cm in the $r - \phi$ plane and 13 cm along the z axis^[93].

2.5.3 Energy resolution

The energy resolution of detectors can be described as follows^[94],

$$\frac{\sigma_E}{E_{\text{rec}}} = \sqrt{a^2 + \frac{b^2}{E_{\text{rec}}} + \frac{c^2}{E_{\text{rec}}^2}}, \quad (2-4)$$

where the parameters $a = 0.016$, $b = 0.081 \text{ MeV}^{1/2}$, and $c = 0.026 \text{ MeV}$ reflect the impact on resolution from detector non-uniformity, photoelectron counting statistic, and noise, respectively. Figure 2.7 shows the energy resolution as a function of reconstructed energy for various calibration sources. The photoelectron counting statistics determine the total resolution. The detector resolutions among eight detectors were consistent within the uncertainties.

2.6 Data taking

2.6.1 Detector operation

The stable operation of the Daya Bay experiment started in December 2011, as shown in Fig. 2.8. At the beginning of the operation, the experiment only had six ADs, namely two ADs in EH1, one AD in EH2, and three ADs in EH3, respectively. The last two ADs were placed in EH2 and EH3 between July 2012 to October 2012. All ADs were in operation from November 2012 to December 2016. From December 2016 to January 2017, the target material (Gd-LS) of one detector in EH1 was replaced by the purified LS used to study the light yields for the next neutrino experiment (JUNO neutrino experiment). The remaining seven ADs have been running since January 2017.

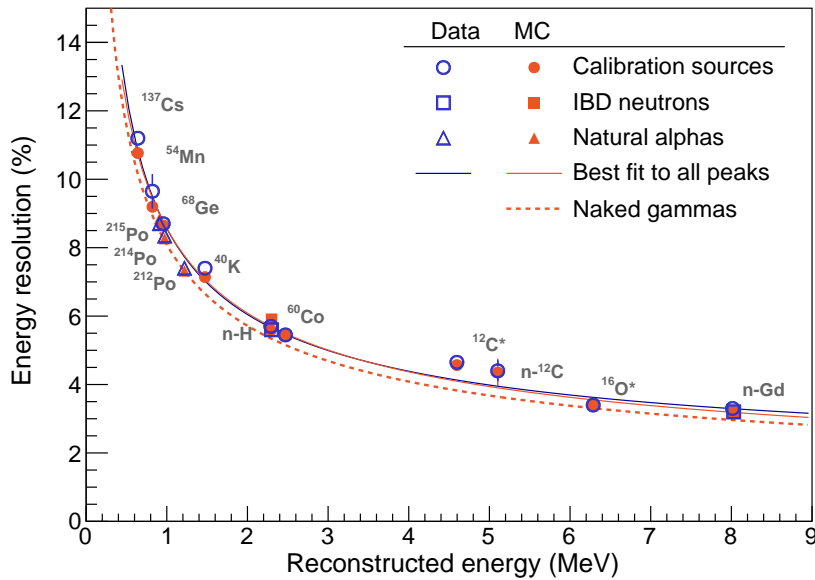


Figure 2.7 The open blue makers represent the energy resolution measured by calibration sources, IBD neutrons, and natural α particles. The blue solid line represents the limits of resolution given by the statistical uncertainty of photoelectron counting. The solid orange markers reveal that the resolutions are consistent with the Monte-Carlo simulation. The dashed orange shows that the predicted from the simulation is better than estimated for the calibration sources. The open blue triangles represent the resolutions for natural α particles. (From Ref.^[94]).

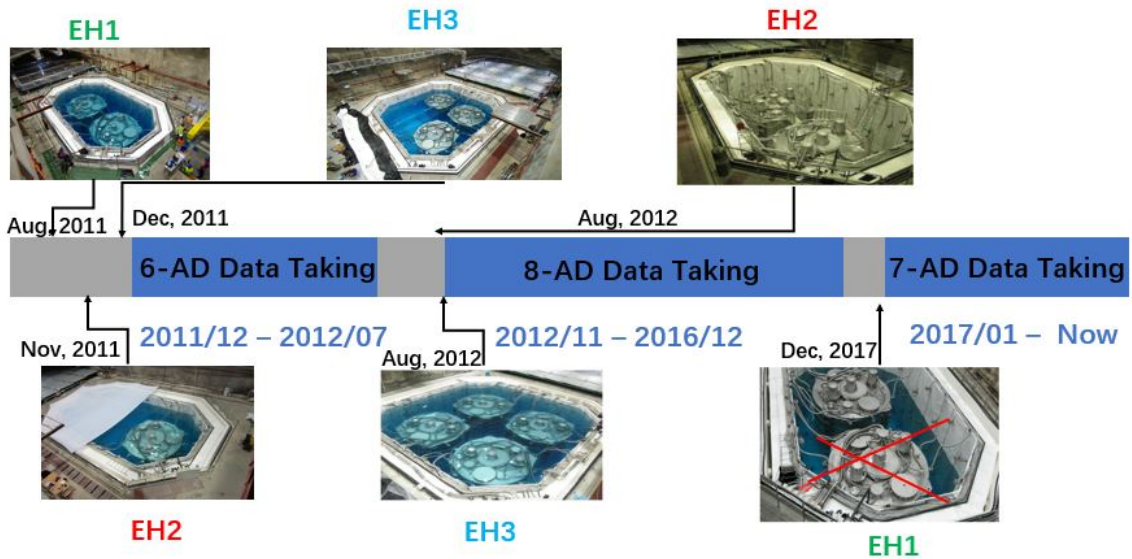


Figure 2.8 Time line of Daya Bay data taking and AD installation.

2.6.2 Reconstructed data production

Based on the Daya Bay experiment's analysis requirements, the production of data was processed several times. In this thesis, we adopted the data production P17B for the GW analysis and P17B+P19A for the GRB analysis. Below are a brief introduction to all the data productions.

P12A: The reconstructed data of EH1 from September 2013 to December 2014 for comparative study with two detectors in EH1.

P12B: Three sites θ_{13} analysis samples.

P12C: Six ADs analysis samples.

P12D: Reprocessed 2012 MCS sample.

P12E: Final six ADs analysis and calibration samples.

P13A: Eight ADs samples.

P14A: Six and eight ADs samples from 2011.12.24 to 2013.11.30.

P15A: Oscillation analysis for neutrino 2016 conference from 2011.12.24 to 2015.08.09.

P17A: Special calibration samples from 2017.01.01 to 2017.02.16.

P17B: Oscillation analysis for neutrino 2018 conference from 2011.12.24 to 2017.08.31.

P19A: Oscillation analysis for neutrino 2020 conference from 2017.9.1 to 2019.3.13.

Chapter 3 Neutrino energy and fluence

This chapter focuses on the studies of neutrino energy conversion and neutrino fluence calculation. We first introduce the relationship between the neutrino energy E_ν and the prompt energy E_p of the IBD reaction. Then we present how to derive the neutrino fluence associated with GWs or GRBs.

3.1 Energy conversion

The relationship is essential between the $\bar{\nu}_e$ energy and the reconstructed prompt energy. According to the energy conservation, E_ν is derived as follows,

$$E_\nu + m_p = E_k(e^+) + m_{e^+} + E_k(n) + m_n, \quad (3-1)$$

where m_p is the proton mass, $E_k(e^+)$ is the positron's kinetic energy. m_{e^+} is the positron mass. $E_k(n)$ is the neutron's kinetic energy. m_n is the neutron mass. Furthermore, after assuming the proton in stationary and ignoring neutrino mass, we have

$$E_\nu = E_p + E_k(n) + 0.78 \text{ MeV}. \quad (3-2)$$

For the Daya Bay oscillation analysis, the neutrino energy E_ν is about ~ 10 MeV. The neutron kinetic energy is negligible. The relation by $E_\nu = E_p + \delta E$ holds, where $\delta E = 0.78$ MeV. However, as the E_ν energy increases, the neutron kinetic energy becomes significant. In the IBD process, the recoiling neutron will share part of the neutrino energy and transfer to the proton by scattering.

The scintillation light yield will be quenched for given energy when a nuclear recoil happened. *i.e.*, when compared with an electron recoil of the same energy, the scintillation output observed is reduced. This difference's significant contribution comes from the heat associated with the atomic cascades due to nuclear recoils^[95]. A semi-empirical formula was developed to describe this relation by Birks^[96], as follows:

$$\frac{dL}{dr} = \frac{S \frac{dE}{dr}}{1 + kB \frac{dE}{dr}}, \quad (3-3)$$

where dL/dr is the scintillation yield per unit path length r , S is the scintillation efficiency, dE/dr is the specific energy loss for charge particle per unit mass thickness,

BdE/dr is the density of excitation centers along the recoil ionization track, k is the quenching factor. The kB is treated as a single parameter (Birks factor). Here we used $kB = 0.0125 \text{ gMeV}^{-1} \text{ cm}^{-2}$ ^[97] in the simulation at Daya Bay.

We studied the performance of the neutron energy quenching effect in the simulation. We first generated a flat neutrino energy spectrum from 1.8 MeV to 100 MeV in the GdLS + LS volume. Figure 3.1 shows the actual kinetic energy of positron distribution in the simulation. The broadening of positron kinetic energy is due to the angle between positrons and neutrinos.

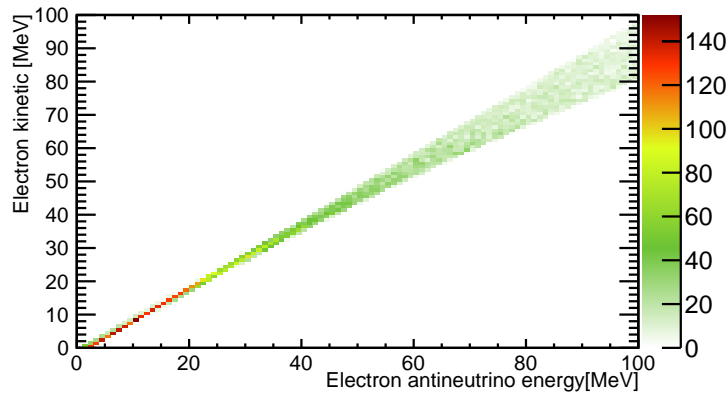
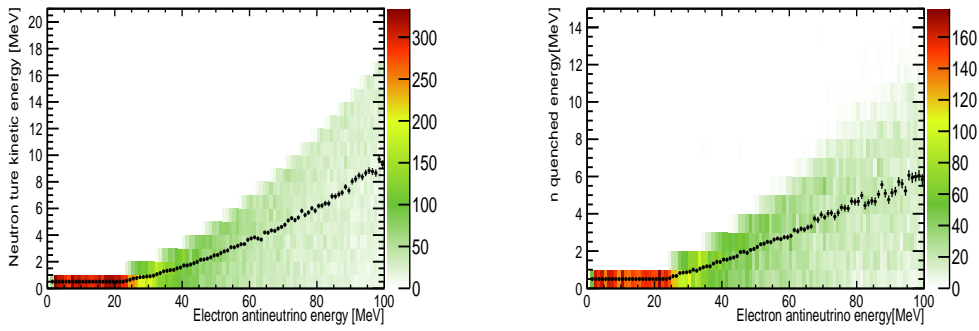


Figure 3.1 Relationship between true kinetic energy of positrons and neutrinos in the simulation.

We also investigated the actual neutron's kinetic energy in the simulation in addition to the actual positron's kinetic energy. Figure 3.2(a) shows the distribution of actual neutron's kinetic energy. The maximum and average neutron energies are 17 and 10 MeV, respectively, for neutrino energy at 100 MeV. Figure 3.2(b) shows the quenching energy loss of neutrons in the simulation. We noted that more than half of recoiled neutron kinetic energy can be detected in the liquid scintillator and added to the positron energy and form the prompt energy. In our analysis, we have considered the quenching effect and detector response in the simulation.



(a) True kinetic energy of neutrons in the simulation. (b) Quenching energy loss of neutrons in the simulation.

Figure 3.2 Distributions of true kinetic energy and quenching energy loss of neutrons in the simulation.

As shown in Fig. 3.3, we simulated several neutrino energy points of $E_\nu < 100$ MeV in the detector of Daya Bay. A simple fitting function illustrates the relation between the neutrino energy and the mean reconstructed prompt energy, $E_p = A \times E_\nu^2 + B \times E_\nu + C$, where $A = -0.001 \text{ MeV}^{-1}$, $B = 1.01$, $C = -0.73 \text{ MeV}$. When the neutrino energy $E_\nu = 0$, the energy calculated is approximate to the mass difference between protons and neutrons, plus the mass of positrons. In this thesis work, the neutrino energies between 1.8 MeV and 100 MeV corresponds to the prompt energies between 0.7 MeV and 90 MeV.

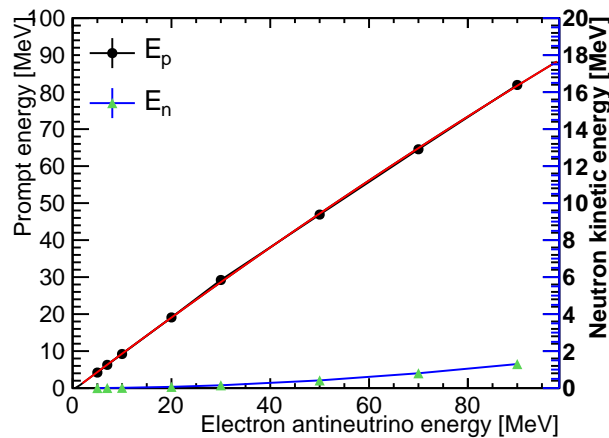


Figure 3.3 Relation between neutrino energy and prompt energy. The black line represents the prompt energy. The red line represents the fitting result of the prompt energy. A simple fitting was adopted. $E_p = A \times E_\nu^2 + B \times E_\nu + C$, where $A = -0.001 \text{ MeV}^{-1}$, $B = 1.01$, $C = -0.73 \text{ MeV}$. The blue line represents the average kinetic energy of neutrons.

3.2 Neutrino fluence

The merger of BH-BH or NS-NS should have an accretion disk that may produce $\bar{\nu}_e$, which the majority fall well below 100 MeV^[98]. Therefore, our analysis focuses on the energy of less than 100 MeV. The neutrino fluence $F(E_\nu)$ can be given assuming the Fermi-Dirac spectrum from the below equation.

$$F(E_\nu) = \frac{N_\nu}{N_T \int \sigma(E_\nu) \varepsilon(E_\nu) \lambda_{\text{FD}}(E_\nu) dE_\nu}, \quad (3-4)$$

where N_ν is the total amount of background subtracting $\bar{\nu}_e$'s in a specific energy interval in the Daya Bay experiment. $N_T = (3.15 \pm 0.02) \times 10^{30}$ is the number of proton targets in a single AD. $\sigma(E_\nu)$ is the IBD cross-section. And $\varepsilon(E_\nu)$ is the detector efficiency. $\lambda_{\text{FD}}(E_\nu)$ is the normalized neutrino energy spectrum. Figure 3.4 shows the normalized Fermi-Dirac energy spectrum $\lambda_{\text{FD}}(E_\nu)$, which is given for zero chemical potential and pinching factor $\eta = 0$:

$$\lambda_{\text{FD}}(E_\nu) = \frac{1}{T^3 F_2(\eta)} \frac{E_\nu^2}{e^{E_\nu/T} + 1}, \quad (3-5)$$

where the complete Fermi-Dirac integral function $F_2(\eta)$ is given by

$$F_2(\eta) = \int_0^\infty \frac{x^2}{e^{x-\eta} + 1} dx. \quad (3-6)$$

The temperature $T = \langle E \rangle / 3.15$. The average energy $\langle E \rangle$ is 12.7 MeV^[99]. The average energy of the accretion disk model has a negligible effect on the Fermi-Dirac spectrum.

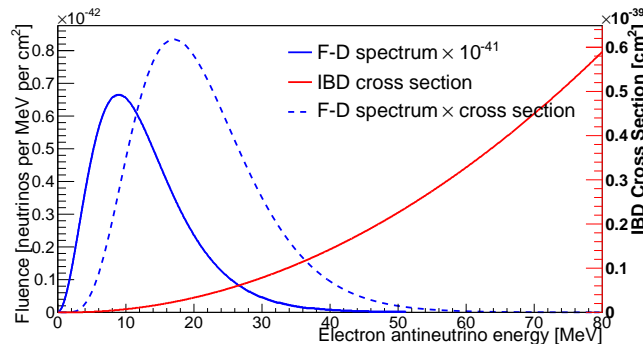


Figure 3.4 Fermi-Dirac energy and flux spectra for the electron anti-neutrinos

We also estimated the neutrino fluence $F_D(E_\nu)$ at several discrete energies below 100

MeV as,

$$F_D(E_\nu) = \frac{N_\nu}{N_T \sigma(E_\nu) \epsilon(E_\nu)}, \quad (3-7)$$

We depict a flow chart of the neutrino generation from GWs or GRBs to the Daya Bay detectors in Fig. 3.5, including related parameters to calculate the neutrino fluence. The main background for our analysis is reactor neutrinos and fast neutrons.

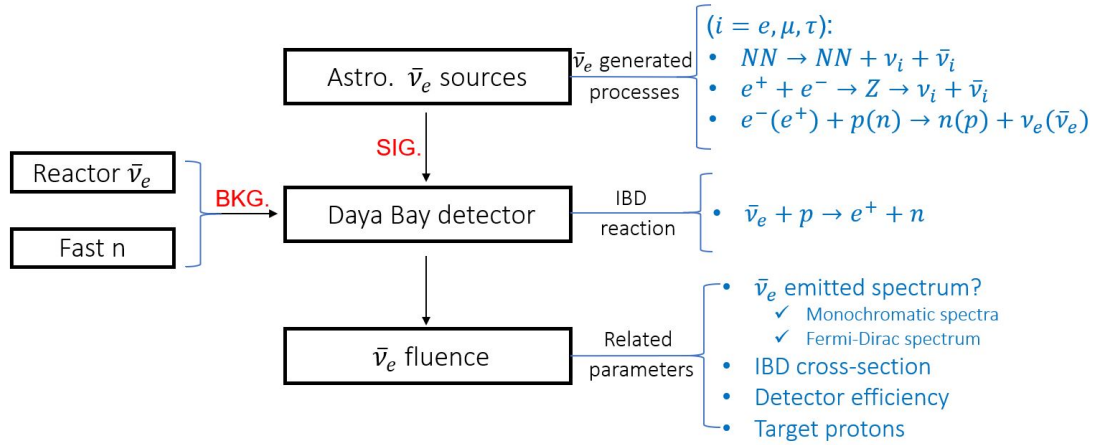


Figure 3.5 Schematic flow of the neutrino generation from GWs or GRBs to the Daya Bay detectors. Furthermore, it also provides the neutrino fluence calculation and the main background sources for our analysis.

Chapter 4 Simulation studies

This chapter focuses on the simulation studies of the Daya Bay detector. We first give an introduction to the IBD cross-section in the simulation generator. We then present our comparison results for neutron simulation with different libraries for thermalization processes and capture cross-sections. In the end, we report the capture fraction of IBD neutron simulation in the detector.

4.1 IBD cross-section

An electron anti-neutrino interacts with a nucleon through the charge-current process, which can be calculated with a precision relying on the expansion in powers of the inverse mass of nucleon.

4.1.1 IBD cross-section formulae

In Daya Bay's oscillation analysis, the reactor neutrino energy is below 10 MeV. Vogel and Beacom provided the energy-dependent IBD cross-section that used at Daya Bay^[69]. Figure 4.1 shows the total IBD cross-section and the average scattering angle $\langle \cos \theta \rangle$ between the neutrino and positron as a function of neutrino energy, under different expansions in powers of $1/M$ (nucleon mass: M), respectively. They also provided the result from the general form of the cross-section (for reference, one can see Eq.(3.18) in Ref.^[100]). We can observe that the general form did not consider the IBD threshold, leading to a slightly lower cross-section. (See the plot for more details).

However, the above function is only accurate for neutrino energy for a few of ten MeV, which is not applicable for our analysis. Strumia and Vissani studied the quasi-elastic antineutrino/proton and neutrino/neutron scatterings^[101]. They considered the higher-order terms of $1/M$ in order to extend neutrino energies up to 200 MeV, which covers the neutrino energy range of 1.8 - 100 MeV. Therefore, we adopted Strumia and Vissani's IBD cross-section in our study.

Since Strumia and Vissani did not provide a simple function except for numerical calculations at several discrete energy points, we had to calculate the cross-section using their formula for continuous neutrino energy from 20 MeV to 200 MeV. Table 4.1 lists

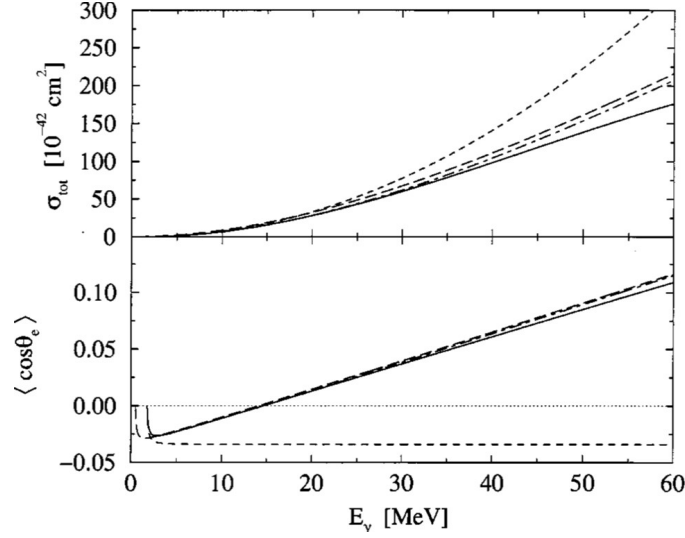


Figure 4.1 Upper panel is the total cross-section for $\bar{\nu}_e + p \rightarrow e^+ + n$. The bottom panel is the average $\langle \cos\theta \rangle$. The solid line is the result at first order in $1/M$ where M is the nucleon mass and the short-dashed line is result at zeroth order in $1/M$. The long-dashed line is the result of Eq.(3.18) of Ref.^[100]. The dot-dashed line is the result after considering the contributions of the threshold ($E_\nu = 1.806$ MeV) effects. (From Ref.^[69]).

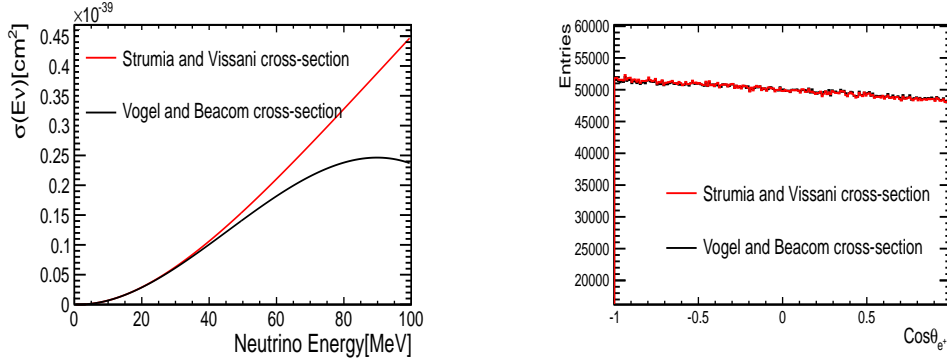
the difference of IBD cross-section and the average cosine of the scattering angle $\langle \cos\theta \rangle$ between the two calculations. We found that the relative deviation was less than 0.4%, which was due to numerical calculation precision. We ignored this difference since it is much precise than our research accuracy.

Table 4.1 Verification of our repeat calculation with Strumia and Vissani’s results of $\sigma(\bar{\nu}_e p \rightarrow ne^+)$. The unit of cross-section is 10^{-41} cm^2 . The “ σ_P ” represents the cross-section from Strumia and Vissani’s results. The “ σ_R ” represents the cross-section repeated by this thesis work. The “ $\langle \cos\theta_P \rangle$ ” represents the average cosine of the scattering angle from Strumia and Vissani’s results. The “ $\langle \cos\theta_R \rangle$ ” represents the average cosine of the scattering angle repeated from our work.

E_ν	σ_R	σ_P	$ \frac{\sigma_P - \sigma_R}{\sigma_P} $	$\langle \cos\theta_R \rangle$	$\langle \cos\theta_P \rangle$	$ \frac{\langle \cos\theta_P \rangle - \langle \cos\theta_R \rangle}{\langle \cos\theta_P \rangle} $
21.2	3.24	3.24	0	0.015	0.015	0
66.9	25.0	25.0	0	0.132	0.131	0.76%
104	47.3	47.4	0.21%	0.228	0.225	1.33%
160	81.0	80.2	0.12%	0.363	0.361	0.55%
200	102	101.6	0.39%	0.447	0.442	1.13%

To see the improvement with the high order correction, we compare the total cross-section and $\cos\theta$ between Vogel et al., and Strumia et. al in Fig. 4.2. One can see that the total IBD cross-sections are almost identical at low energies and start to depart as the

neutrino energy increases. Both of the $\cos \theta$ distributions are also identical for neutrino energy at 10 MeV.



(a) Total IBD cross-section within the $\bar{\nu}_e$ energy range < 100 MeV. (b) $\cos \theta$ of neutrino energy 10 MeV between $\bar{\nu}_e$ and positron direction.

Figure 4.2 Distribution of total cross-section versus neutrino energy below 100 MeV and distribution of $\cos \theta$ of neutrino energy 10 MeV.

4.1.2 IBD cross-section in GW and GRB analyses

We calculated the monochromatic spectra and the Fermi-Dirac spectrum using Strumia, and Vissani's cross-section function. For the monochromatic spectra, we selected some discrete neutrino energy points, namely 5 MeV, 7 MeV, 10 MeV, 20 MeV, 30 MeV, 50 MeV, 70 MeV, and 90 MeV to represent the whole energy < 100 MeV. The IBD cross-section is a vital parameter to derive the fluence. Table 4.2 lists the detailed IBD cross-section for the monochromatic spectra and the average cross-section, $\bar{\sigma}(E_\nu)$, for the Fermi-Dirac spectrum. The average cross-section, $\bar{\sigma}(E_\nu)$, is determined by integrating the IBD cross-section from 1.8 to 100 MeV over the neutrino spectrum.

Table 4.2 IBD cross-section for discrete energy points and the average IBD cross-section, $\bar{\sigma}(E_\nu)$, for the Fermi-Dirac spectrum.

E_ν (MeV)	5	7	10	20	30	50	70	90
$\sigma(E_\nu) (\times 10^{-42} \text{ cm}^2)$	1.27	2.96	6.76	28.9	63.0	156	268	389
$\bar{\sigma}(E_\nu) (\times 10^{-42} \text{ cm}^2)$	14.7							

4.2 Study of the neutron databases in Geant4

For high-energy IBD, since neutrons can have significant recoiled kinetic energy, understanding how a neutron is slow down, thermalized, and eventually captured by a

nucleus is critical in evaluating the detector efficiency. We wrote a fast simulation code to estimate the effect of different neutron databases in Geant4.

4.2.1 Geant4 simulation for neutrons

Geant4 is a software package that can simulate the passage of particles through matter^[102]. After several years of development of Geant4, the physics model in the simulation becomes more mature. Currently, the latest Geant4 version upon the end of the thesis work is Version 10.6, with the neutron database updated from Version 9 series to Version 10 series. Below are the changes described by Ref.^[103].

- (i) New Neutron data set version from G4NDL.4.2 to G4NDL.4.5.
- (ii) Enable to use of dynamically-generated materials.
- (iii) *G4NeutronHPFinalState*: the added capability to disable adjustment of final state photons in the capture.

4.2.2 The fast simulation framework

We summary the neutron simulation framework in Fig. 4.3 and introduce several steps to study neutron simulation. First, an example of Geant4 itself named Hadr04 was used to carry out the simulation. Then, we studied two physical lists of Geant4 versions, namely Geant4 Version 9.6 and 10.3, separately. We constructed a simplified geometry, placed neutrons of different energies in the GdLS, and studied their properties, including flight time, flight distance, and neutron capture fraction.

Figure 4.4 shows the cylindrical detector geometry set-up, GdLS, LS, and MO layers. The simulation used a physical list with only the *neutronHP* package, which has registered physical processes, such as neutron elastic process (including thermal scattering), inelastic process, neutron nuclear capture process, and neutron-induced fission process. Appendix A and B give the physical list in Geant4 Version 9.6 and 10.3, respectively.

4.2.3 Simulation results

We performed a comparison study using different neutron databases in Geant4 to estimate the detector efficiency impact. In the analysis of this thesis work, the neutron energy range we were interested in is less than 20 MeV, estimated from the $E_\nu < 100$ MeV. We scanned some discrete neutron kinetic energies to understand the impact of Geant4 versions, namely 1 eV, 1 keV, 1 MeV, 5 MeV, and 15 MeV, respectively.

In the simulation, we uniformly put neutrons into the GdLS region and let them

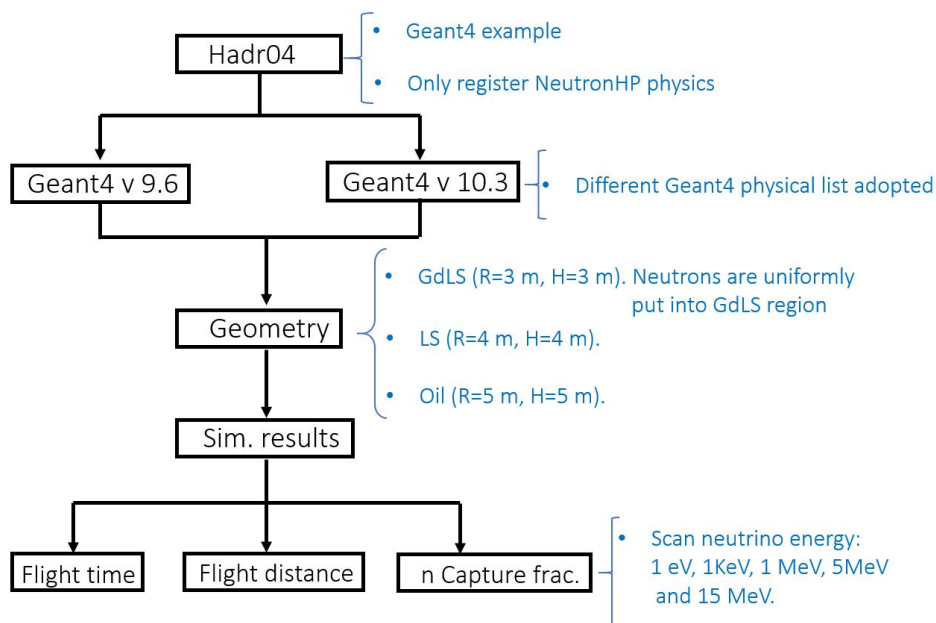


Figure 4.3 Summary of neutron simulation processes to study the influence brought by different Geant4 physical lists. “Sim.” means simulation. “frac.” means fraction.

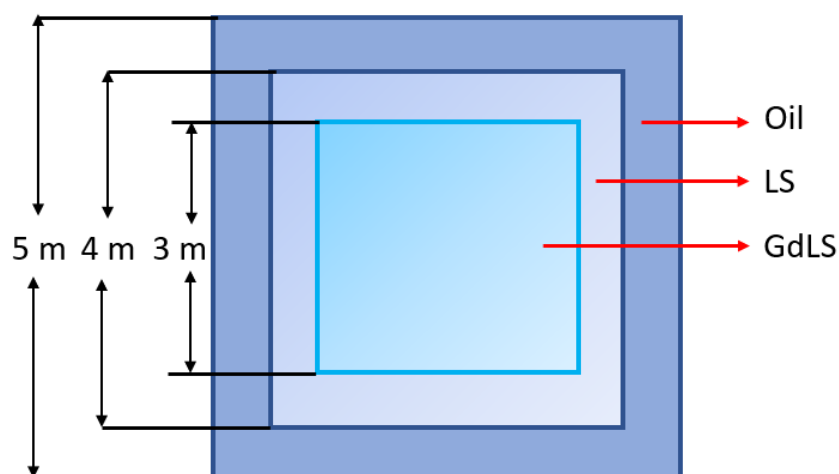


Figure 4.4 Schematic view of the detector in the simulation. Neutrons generated uniformly in the GdLS region.

isotropic emitted. And then, we studied the neutron’s flight time and flight distance, respectively. Figure 4.5 and 4.6 shows the simulation results of flight time and flight distance, respectively. As the neutron energy increases, the neutron’s flight time has a slight difference between the two Geant4 versions. However, there is no apparent difference between the flight distances. We concluded that we could neglect the effect due to the two different neutron databases in the Geant4.

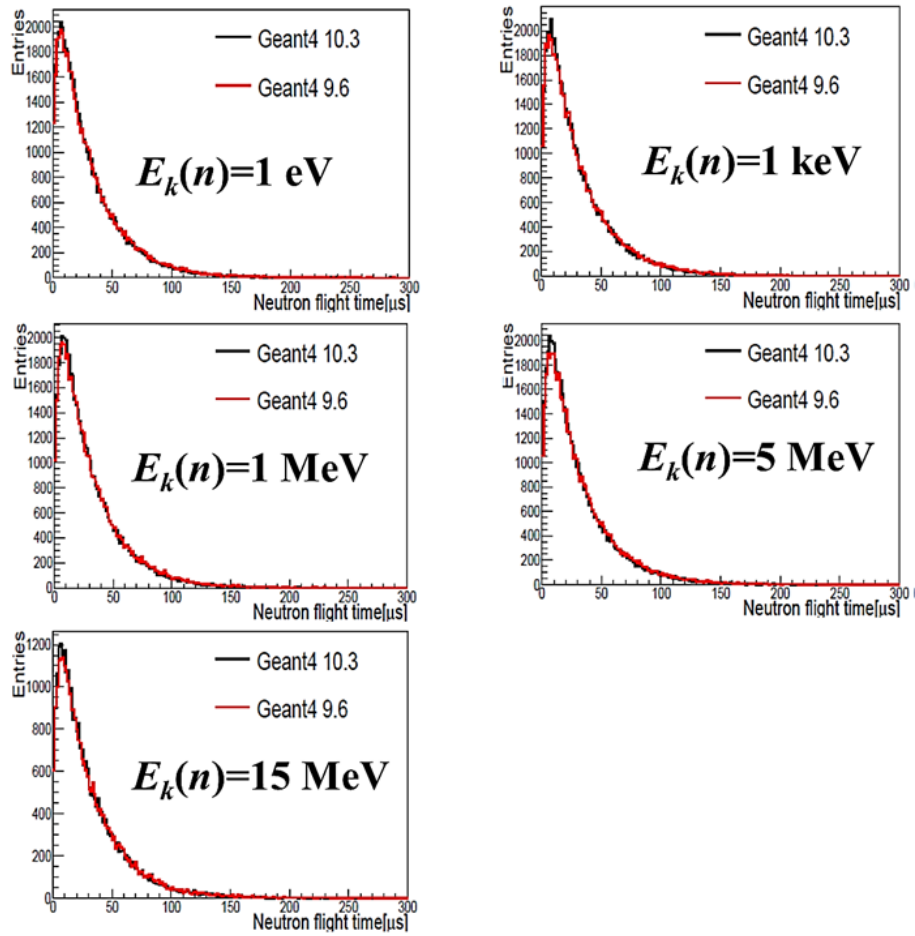


Figure 4.5 Neutron's flight time until captured in the GdLS. Several discrete neutron kinetic energies were selected and simulated in the two different Geant4 versions, respectively. Neutrons are put into the GdLS region and isotropic emitted.

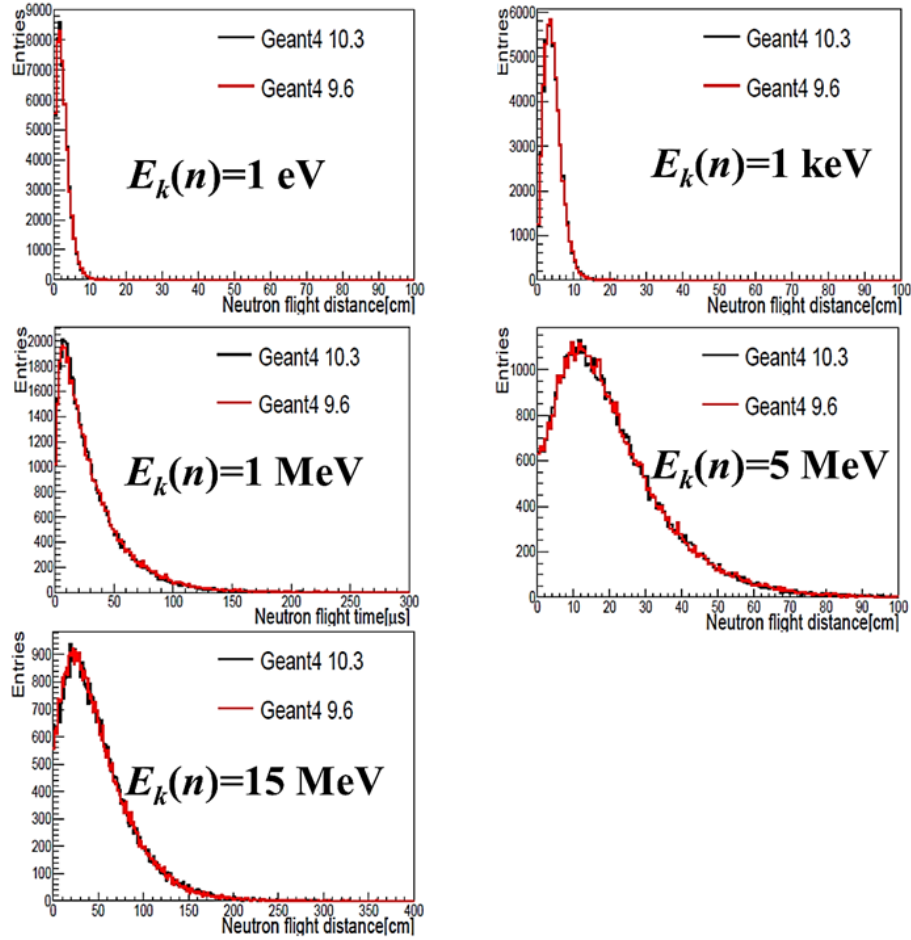


Figure 4.6 Neutron's flight distance until captured in the GdLS. Several discrete neutron kinetic energies were selected and simulated in the two different Geant4 versions, respectively. Neutrons are put into the GdLS region and isotropic emitted.

Besides the flight distance and the flight time, neutron capture fractions were estimated. Table 4.3 lists the neutron capture fractions at some specific neutron energies in the two Geant4 versions. One can see that the difference of neutron capture fraction between the two versions is also negligible. After considering the neutron flight time, distance, and capture fraction, we concluded that the different neutron databases in the Geant4 Version 9 and 10 series did not affect our analysis.

Table 4.3 Neutron capture fractions in the two different Geant4 versions for several specific neutron energies. The uncertainties are only statistical.

$E_k(n)$	1 eV	1 KeV	1 MeV	5 MeV	15 MeV
Geant4 v 9.6	100%	100%	100%	98.15±0.06%	57.93±0.22%
Geant4 v 10.3	100%	100%	100%	98.18±0.06%	58.42±0.22%

4.3 Full simulation package for the Daya Bay experiment

The Daya Bay Collaboration developed a full simulation and reconstruction package – Neutrino at Daya Wan (NuWa), and its main detector simulation based on Geant4^[104]. It was validated by the comparisons to data^[105]. A few key improvements were given, for instance, the Daya Bay customized the gamma spectra captured by Gd based on the NNDC database. Furthermore, the neutron data file used in Version 9.02 is G4NDL.3.11. Figure 4.7 shows the simulation processes in NuWa at Daya Bay.

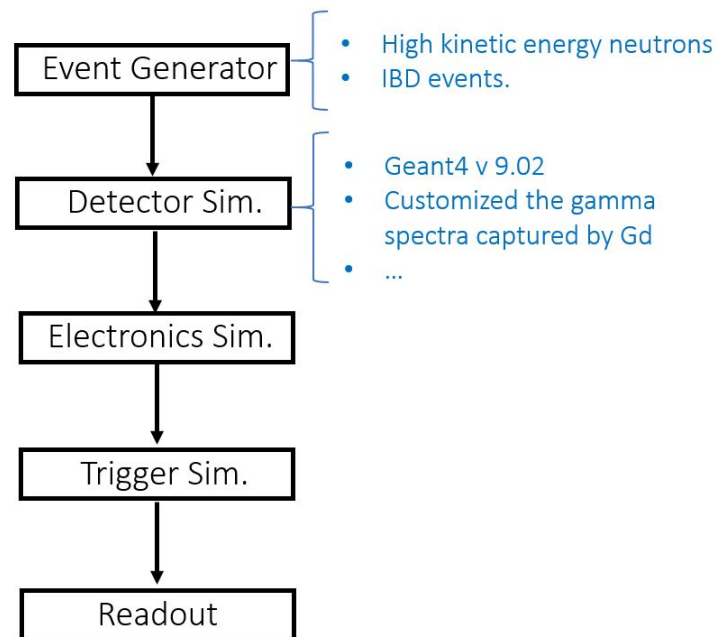


Figure 4.7 Block diagram for the simulation processes in NuWa at Daya Bay.

4.4 The capture fraction of IBD neutrons

The IBD neutron's energy can vary according to its emitting angle, even for fixed neutrino energy. The Daya Bay experiment cannot measure this angle. Instead, the experiment can only measure the gamma energy released by neutron capture on a nucleus. When neutrons from the IBD process, they might encounter an inelastic process, producing secondary neutrons as a consequence. The carbon in the liquid scintillator can also absorb the IBD neutron and form a compound nucleus, which then emits an alpha particle and beryllium. This process is referred to as to (n, α) as shown below,



We simulated a 90 MeV neutrino case in the GdLS target volume at NuWa. Fig. 4.8 shows the detailed reaction processes. We only recorded the neutron tracks in the simulation because it is the delayed signal for IBD events. It shows that most of the secondary neutrons generated by the inelastic scattering can still be captured. Only a few percentages of neutrons happen to the (n, α) process.

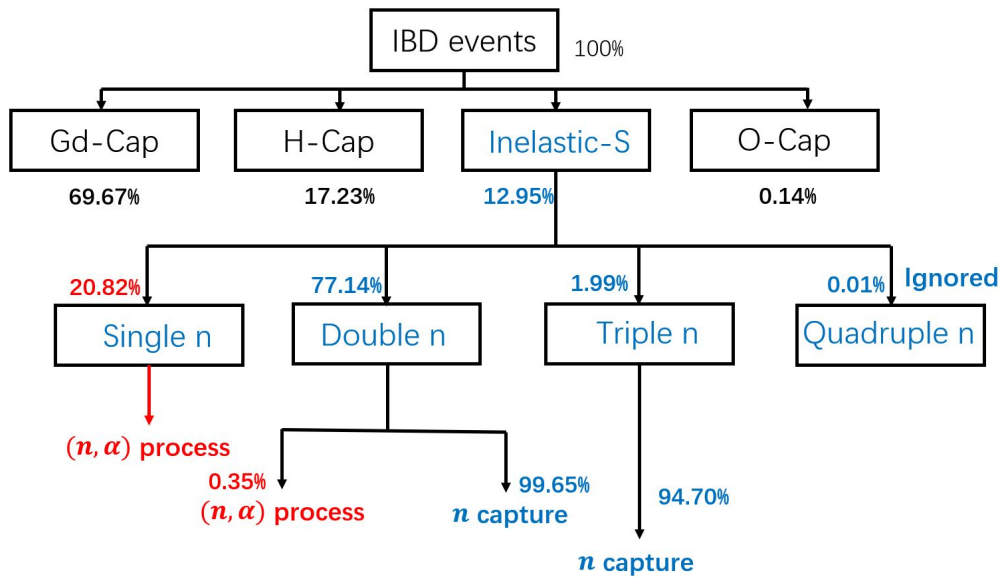


Figure 4.8 Detailed simulation processes for a 90 MeV neutrino case at NuWa. The numbers in the flow chart are the branching ratio of IBD events. “Gd-Cap” represents the physical process of Gd-captured. “H-Cap” represents the physical process of H-captured. “O-Cap” represents the physical process by other nuclei captured. “Inelastic-S” represents the inelastic scattering physical process. We only recorded the neutron tracks in the simulation because it is the delayed signal for IBD events.

We simulated IBD events at several discrete neutrino energies in the GdLS volume

and calculated the fraction of neutrons captured by different target elements, e.g. H, Gd, C, etc. The detailed results are given in Table 4.4. The (n, α) physical process is seen to increase as the neutrino energy increases.

Table 4.4 Neutron captured fractions by different target elements in the GdLS volume is calculated.

E_ν	5 MeV	7 MeV	9 MeV	20 MeV	30 MeV	50 MeV	70 MeV	90 MeV
H	15.76%	15.76%	16.09%	16.37%	17.04%	17.94%	19.28%	19.68%
Gd	84.11%	84.09%	83.78%	83.48%	82.82%	81.90%	79.91%	77.34%
C and O	0.12%	0.12%	0.12%	0.12%	0.12%	0.14%	0.24%	0.34%
(n, α)	0.01%	0.03%	0.02%	0.03%	0.02%	0.02%	0.57%	2.64%

4.5 Chapter summary

In this chapter, we focused on discussing the detector simulation. The first study was IBD cross-section. Previously, Vogel and Beacom's cross-section was only applicable to the neutrino energy for a few of ten MeV at Daya Bay, but not our interesting energy range (below 100 MeV). Therefore, Strumia and Vissani's cross-section we adopted in the analysis extended the neutrino energy up to 200 MeV.

We studied the impact brought by different Geant4 neutrino databases in the simulation. We constructed a fast simulation framework and found that the influence caused by different versions can be ignored in our analysis.

Then, we studied the capture fractions of IBD neutrons by the full simulation package for the Daya Bay experiment, NuWa. We found that the (n, α) physical process is seen to increase as the neutrino energy increases.

Chapter 5 Events selection criteria and efficiency

In this chapter, we first introduce the IBD events selection criteria in this analysis under two neutrino energy spectra, namely the monochromatic spectra and the Fermi-Dirac spectrum. Then, we define the detection efficiency for nGd and nH samples. In the end, we provide the energy-dependence detection efficiency for the entire studied energy range.

5.1 Events selection criteria

Table 5.1 lists the IBD selection criteria for the nGd and nH analyses. Just for a reminder, we added a few minor modifications of the standard selection criteria^[106-107].

Table 5.1 IBD selection criteria for the nH and nGd analyses. The details in the text.

Class	nH	nGd
AD trigger	$N_{\text{PMT}} \geq 45$ OR $Q_{\text{SUM}} \geq 65$ p.e.	
20-cm PMT flash	Ellipse < 1	
AD muon (μ_{AD})	> 100 MeV	
Showering AD muon (μ_{sh})	> 2.5 GeV	
WS muon (μ_{WS}) [IWS/OWS]	$N_{\text{PMT}} > 12/15$	$N_{\text{PMT}} > 12/12$
AD muon veto	(0, 800) μs	
Pool muon veto	(0, 600) μs	
Shower muon veto	(0, 1) s	
Coincidence time (T_c)	[1, 400] μs	[1, 200] μs
Delayed energy (E_d)	Peak $\pm 3\sigma$	[6, 12] MeV
Coincidence distance (D_c)	< 1000 mm	N/A
Prompt energy (E_p)	Signal searching region	

AD events caused by spontaneous light emission from any one of 192 20-cm PMTs were removed by $Ellipse = \sqrt{\text{Quadrant}^2 + (q_{\text{max}}/0.45)^2} < 1$, where q_{max} represents the largest fraction of total charge from one single PMT in an AD event, and $\text{Quadrant} = Q_3/(Q_2 + Q_4)$ in which Q_i represents the total charge in AD azimuthal quadrant i and Q_1 is the quadrant centered around the PMT with q_{max} . The efficiency for this criterion was estimated with Monte Carlo simulation^[105] to be $> 99.99\%$.

We rejected the delay-like event following a muon within a veto time of t^{veto} . Several

types of muon veto t^{veto} are described below in detail.

- (i) Shower AD muon: Some of the muons with high energy ($\sim\text{GeV}$) in the ADs always induce significant neutron emission and secondary particles. The high yield scintillation light exceeds the expectations of minimum-ionizing muons, so-called muon showers. For the energy of AD muon shower above 2.5 GeV, we give a time veto window of $t_{\text{shower}}^{\text{veto}} = 1$ s.
- (ii) Pool muon: When the PMTs (at least 12) got fired in either IWS or OWS, these muons were tagged. It is necessary to set a time cut to remove the neutrons produced through muon interaction with water, reaching the target material. A veto time of $t_{\text{WS}}^{\text{veto}} = 600 \mu\text{s}$ was used to reject most of these neutrons.
- (iii) AD muon: On average, muon deposits about 0.6 GeV in the AD. The time veto window of $t_{\text{AD}}^{\text{veto}} = 800 \mu\text{s}$ was sufficient to reject such a background.

Cuts on muons could cause a dead time to the neutrino event detection, which was quantified as an effective contribution ε_{μ} to the $\bar{\nu}_e$ selection efficiency for each detector. The efficiency was measured from the data using

$$\varepsilon_{\mu} = \left(\sum_i t_i^s \right) / t_{\text{DAQ}}, \quad (5-1)$$

where t_i^s is the individual segments i of the livetime between each vetoed period in a detector. The total data taking livetime, t_{DAQ} , is the whole time from the first to the last signal in the DAQ period.

We required the coincident time of the prompt and delayed energy to be higher than $1 \mu\text{s}$, and less than $200 \mu\text{s}$ and $400 \mu\text{s}$ for nGd sample and nH sample, respectively. The delayed energy is more than 6 MeV for nGd sample and around 3σ of 2.2 MeV gamma peak for nH sample. A cutoff of the coincident distance of 1000 mm was applied to the nH sample. Furthermore, we set the prompt energy cut based on the different searching energy region below,

- For the Fermi-Dirac spectrum, the IBD events with prompt signal energies < 90 MeV were used to search for the coincident $\bar{\nu}_e$ signals associated with GWs or GRBs at Daya Bay. We classified the raw data into low-energy and high-energy due to the reactor neutrino background's major energy below 10 MeV. For low-energy data, the prompt energy range included nH:(3.5,10) MeV and nGd: (0.7,10) MeV. The 3.5 MeV lower bound in the nH sample was used to remove the significant accidental background. For high-energy data, the prompt energy range is (10, 90)

MeV for both nGd and nH.

- For the monochromatic spectra, we chose several neutrino energies, namely 5, 7, 10, 20, 30, 50, 70, 90 MeV to represent the whole energy range of less than 100 MeV. For these discrete neutrino energies, the prompt energy search window was $E_p \pm \Delta$, where Δ defined as follows:

$$\Delta = 5 \times \sqrt{a^2 \times E_p^2 + b^2 \times E_p + c^2}, \quad (5-2)$$

where the parameters, $a = 0.016$, $b = 0.081 \text{ MeV}^{1/2}$, and $c = 0.026 \text{ MeV}$, which simply come from the detector resolution equation to define signal window.

5.2 Definition of detection efficiency

The simulation framework at Daya Bay is based on NuWa introduced in the previous section. We exploited the nGd and nH IBD events in the detector of 4 m-tank (GdLS+LS+Acrylic) for both GW and GRB analyses, which slightly differed from the oscillation analysis at Daya Bay. For the detection efficiency ε_{det} in the whole detector volume, the definition is as follows:

$$\varepsilon_{\text{det}} = \varepsilon_{\mu} \cdot \varepsilon_m \cdot \varepsilon_{\text{other}}, \quad (5-3)$$

with

$$\varepsilon_{\text{other}} = \sum_v (N_{p,v} \cdot \varepsilon_{E,v} \cdot \varepsilon_{D_c,v} \cdot \varepsilon_{T_c,v}) / \sum_v N_{p,v}. \quad (5-4)$$

ε_{μ} is the muon veto efficiency, and ε_m is the multiplicity cut efficiency, which is determined by the experimental data. The multiplicity cut efficiency ε_m is derived using the coincidence time and uncorrelated singles rate described in detail in reference^[108]. Moreover, the efficiency $\varepsilon_{\text{other}}$ includes $\varepsilon_{E,v}$, $\varepsilon_{T_c,v}$, $\varepsilon_{D_c,v}$, which correspond to the energy (prompt and delayed energy), coincident time, and coincident distance (only for the nH data sample) efficiency, respectively. Since the efficiency $\varepsilon_{\text{other}}$ relies on the assumed energy spectra, we will calculate it in the next subsection. The index, v , represents different target volumes, namely GdLS, LS, Acrylic (Ac). $N_{p,v}$ is the number of free protons in each volume. The proton ratio in the three target volumes is $P_{\text{GdLS}} : P_{\text{LS}} : P_{\text{Ac}} = 1 : 1.077 : 0.1273$ ^[109].

We treated the muon veto efficiency differently for the GW and GRB analyses. For the GW analysis, the evaluation of muon veto efficiency was for the data during the ± 5

days of each GW arrival time. For the GRB analysis, the evaluation was an average for the data from December 2011 to March 2019. Appendix Table C.1 gives the muon veto efficiencies for all the GW and GRB events.

We used the same method to estimate the multiplicity cut efficiency ε_m for the GW and GRB analyses, respectively, as given in Appendix C.2.

We determined the prompt energy efficiency, the delayed energy efficiency, the time selection efficiency, and the distance selection efficiency from simulations with the monochromatic spectra or the Fermi-Dirac spectrum, respectively, introduced in the next subsection.

5.3 Efficiency for the monochromatic spectra

The detection efficiency of each volume was studied carefully in the simulation of several specific neutrino energies under the monochromatic spectra.

Figure 5.1(a) shows the trends of the efficiency with two features: For high-energy neutrino points, more and more neutrons escaped from the GdLS volume to the LS volume. Furthermore, the proportion of neutron capture processes replaced by inelastic scattering (n, α) process increased as the neutrino energy increased. Combining both the features resulted in a decrease in efficiency as neutrino energy increases.

Figure 5.1(b) shows the IBD efficiency for the nH signal in the GdLS volume. In the simulation, more and more high energy neutrons spilled out from the GdLS volume to the LS volume and then captured by hydrogen as the neutrino energy increased, leading to a slow increase in the total efficiency in the GdLS volume.

Figure 5.1(c) shows the IBD efficiency for the nGd signal in the LS volume. In the simulation, the total efficiency in the LS volume increased slowly. More and more neutrons spilled in the GdLS volume from the LS volume and then captured by Gd as the neutron energy increased, leading to a slow increase in the total efficiency.

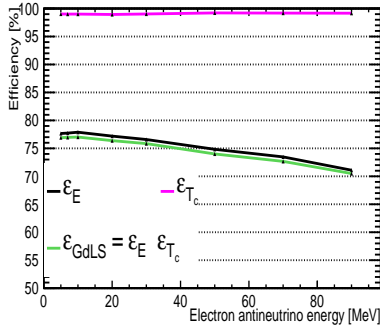
Figure 5.1(d) shows the IBD efficiency for the nH signal in the LS volume. The total efficiency of low-energy neutrino points was lower than other energy points due to the cut of $E_p > 3.5$ MeV. For the high-energy neutrino points, more and more neutrons escaped from the LS volume to MO volume. However, the MO was not the material that could be triggered. Furthermore, the high-energy neutron (n, α) process fraction increased, which also decreased efficiency.

Figure 5.1(e) shows the IBD efficiency of nGd in the Ac volume. For the low-energy

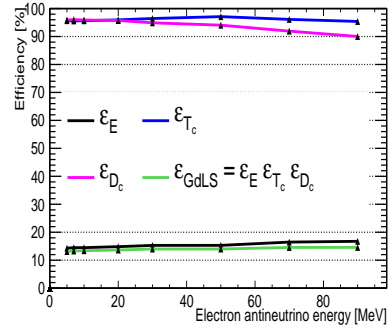
neutrino points, most of the events generated in the acrylic did not fire the trigger. The total efficiency increased slowly.

Figure 5.1(f) shows the IBD efficiency for the nH signal in the Ac volume. For the low-energy neutrino points, most of the events generated in the acrylic also did not fire the trigger. The low energy points had a lower efficiency than the nGd efficiency in acrylic because of $E_p > 3.5$ MeV. The total efficiency was increasing as the neutrino energy increased.

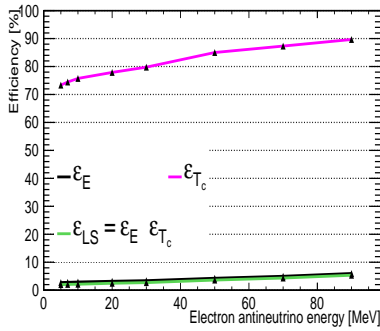
The efficiency trend in different volumes indicates that neutron's physical properties are critical in detectors, especially the high-energy ones. The spill in/out effect of high-energy neutrons determines the detection efficiency. Figure 5.2 illustrates the actual capture vertex of a neutron in the simulation. One can see that more and more neutrons spill out from the original volume as the neutron energy increases, especially in the LS volume because of its thickness. The thickness for LS volume is only 50 cm from GdLS volume to MO volume. It means that the high-energy neutrons are more natural to escape from other volumes from LS volume.



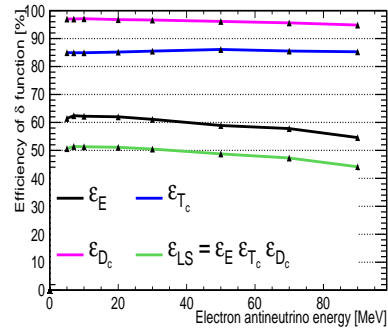
(a) Simulated efficiency of nGd data in the GdLS volume.



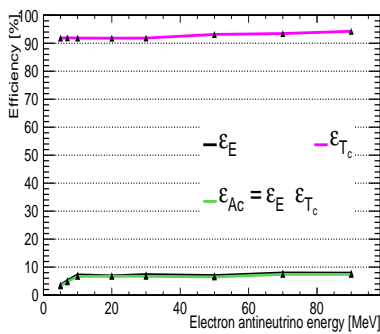
(b) Simulated efficiency of nH data in the GdLS volume.



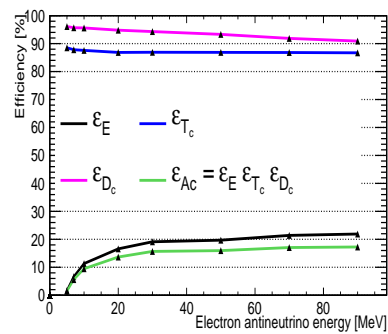
(c) Simulated efficiency of nGd data in the LS volume.



(d) Simulated efficiency of nH data in the LS volume.

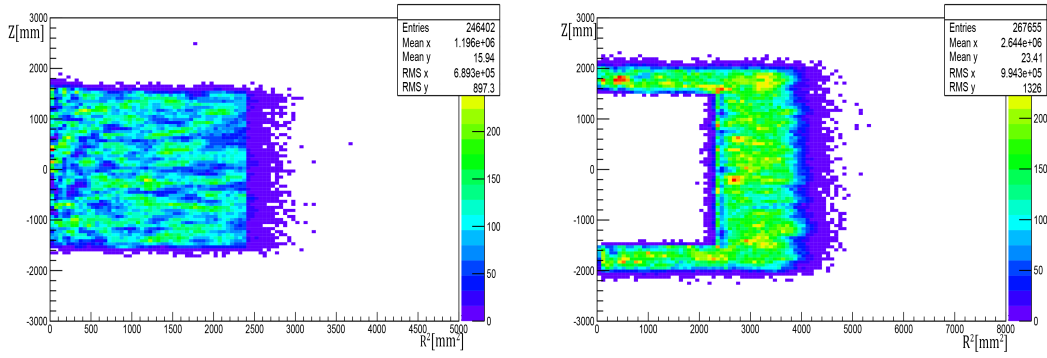


(e) Simulated efficiency of nGd data in the Ac volume.

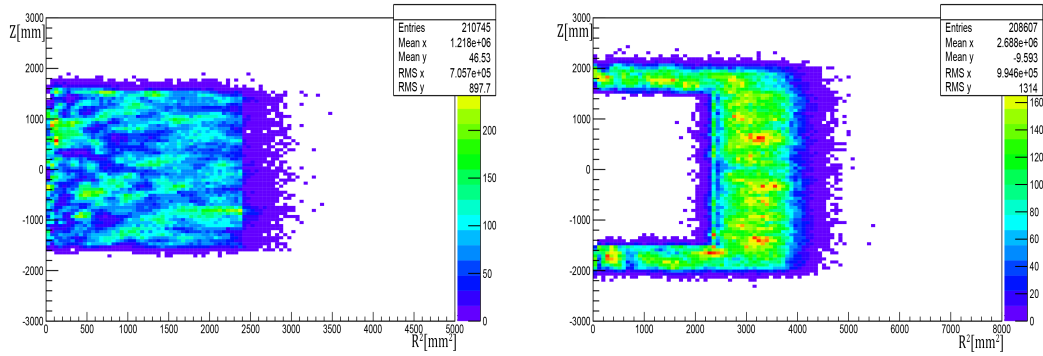


(f) Simulated efficiency of nH data in the Ac volume.

Figure 5.1 Simulated efficiency of nH and nGd data in the detector simulation.



(a) Distribution of the actual capture vertex of neutron for 7 MeV neutrinos simulated in the GdLS volume. (b) Distribution of the actual capture vertex of neutron for 7 MeV neutrinos simulated in the LS volume.

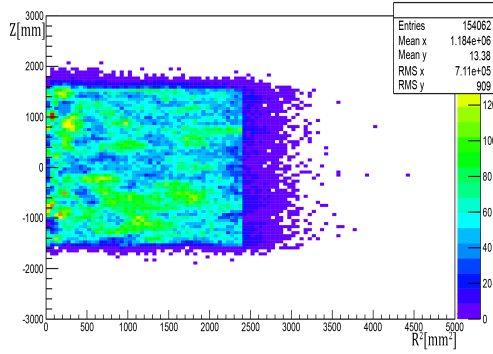


(c) Distribution of the actual capture vertex of neutron for 30 MeV neutrinos simulated in the GdLS volume.. (d) Distribution of the actual capture vertex of neutron for 30 MeV neutrinos simulated in the LS volume.

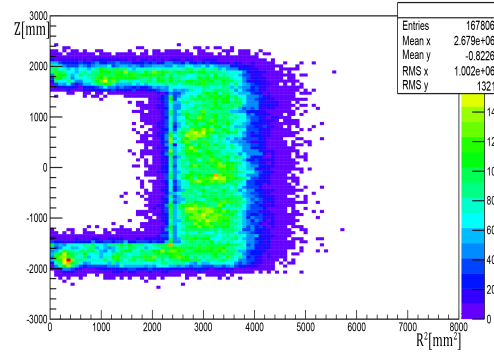
Figure 5.3 shows the IBD efficiency as a function of the anti-neutrino energy for the monochromatic spectra. The changes in the two efficiency curves have been explained in Fig.5.1.

5.4 Efficiency for the Fermi-Dirac spectrum

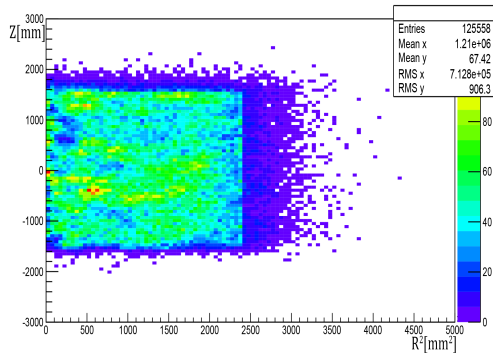
In Chapter 5, we have already shown the Fermi-Dirac energy spectrum and the flux spectrum in the simulation in Fig. 3.4. Table 5.2 gives the IBD selection efficiency results evaluated by simulation for both nGd and nH samples.



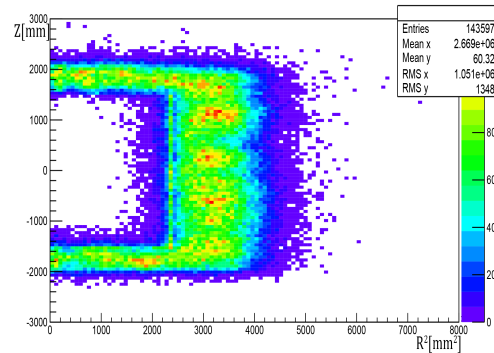
(e) Distribution of the actual capture vertex of neutron for 50 MeV neutrinos simulated in the GdLS volume.



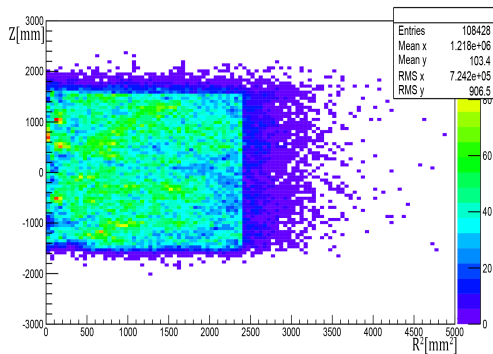
(f) Distribution of the actual capture vertex of neutron for 50 MeV neutrinos simulated in the LS volume.



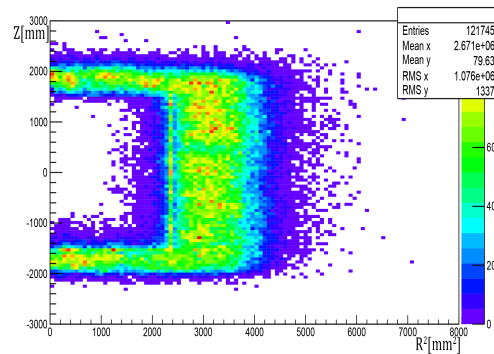
(g) Distribution of the actual capture vertex of neutron for 70 MeV neutrinos simulated in the GdLS volume.



(h) Distribution of the actual capture vertex of neutron for 70 MeV neutrinos simulated in the LS volume.



(i) Distribution of the actual capture vertex of neutron for 90 MeV neutrinos simulated in the GdLS volume.



(j) Distribution of the actual capture vertex of neutron for 90 MeV neutrinos simulated in the LS volume.

Figure 5.2 Distribution of the actual capture vertex of neutron in the GdLS and LS volume.

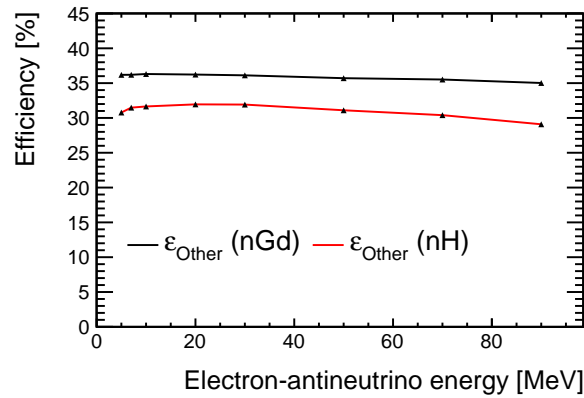


Figure 5.3 IBD selection efficiency, ϵ_{other} , from the MC simulation as a function of the electron anti-neutrino energy.

Table 5.2 Summary of the efficiencies under the assumption of the Fermi-Dirac spectrum. ϵ_{other} is the total IBD selection efficiency evaluated by Monte Carlo for the whole detector including GdLS, LS and Acrylic.

Data sample	nGd sample		nH sample	
	ϵ_{GdLS}	ϵ_{other}	ϵ_{LS}	ϵ_{other}
Low energy	ϵ_{GdLS}	8.72 %		1.66 %
	ϵ_{LS}	0.38 %	4.28 %	6.93 %
	ϵ_{Ac}	2.38 %		3.97 %
High Energy	ϵ_{GdLS}	68.06 %		12.47 %
	ϵ_{LS}	2.11 %	32.18 %	44.00 %
	ϵ_{Ac}	4.73 %		9.41 %

5.5 Chapter summary

This chapter introduced the IBD events selection criteria for two neutrino energy spectra and studied the detection efficiency at Daya Bay. The data sample analyzed in the thesis included the nGd and nH data. When calculating the detection efficiency for different data samples, we selected the 4 m tank consisting of GdLS, LS, and Ac as our target volume. The detection efficiency consists of the muon veto efficiency ϵ_{μ} , the multiplicity cut efficiency ϵ_m , and the other efficiency ϵ_{other} determined by the simulation. ϵ_{other} includes the energy selection efficiency ϵ_E , the coincident distance selection efficiency ϵ_{D_c} , and the coincident time selection efficiency ϵ_{T_c} .

When considering the ϵ_{other} , we carefully discussed the efficiency, ϵ_E , ϵ_{D_c} , and ϵ_{T_c} of GdLS, LS, and Ac, respectively, which could help us understand the efficiency of ϵ_{other} in detail. We used the detection efficiency in calculating the neutrino fluence, as described in the next two chapters.

Chapter 6 Measurement of $\bar{\nu}_e$ associated with GWs

This chapter introduces the measurement of $\bar{\nu}_e$ associated with GWs. Firstly, we present our analysis strategy. Then we give a detailed description of the GW data analysis. In the end, we report how to derive the upper limits for the neutrino fluence and luminosity from the observed candidates.

6.1 Analysis strategy

Here, we describe the likelihood-based statistical tests based on the profile likelihood method^[110] to search for anti-neutrinos from GWs or GRBs. The focus of this section is to discuss the analysis method we adopted.

6.1.1 Validation of likelihood function

To verify the method, we constructed a simple likelihood function of the Poisson distribution, $P(s, b)$.

$$P(s, b) = \frac{(s + b)^n}{n!} e^{-(s+b)}, \quad (6-1)$$

where s is the number of signal events that we interested, b is the number of expected background events, n is the number of observed events. To test a hypothesized value of s , we consider the profile likelihood ratio,

$$\lambda(s) = \frac{P(s)}{P(\hat{s})}, \quad (6-2)$$

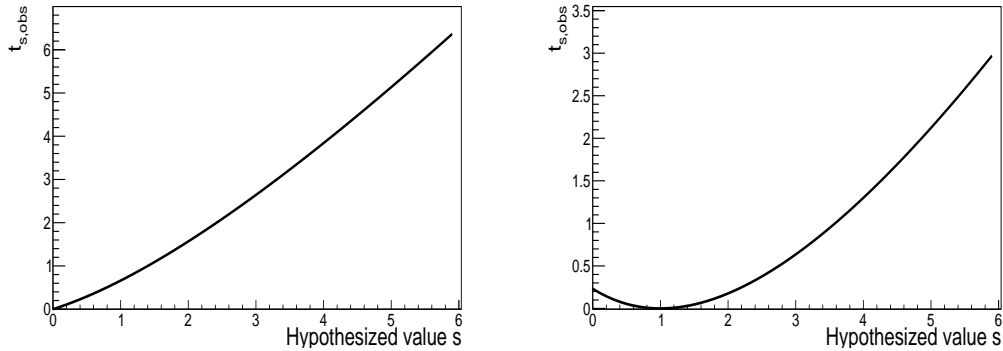
where \hat{s} is the maximum likelihood (ML) estimator. Then, we constructed a test statistic t_s

$$t_s = -2 \ln(\lambda(s)) = \begin{cases} -2 \ln\left(\frac{P(s)}{P(\hat{s})}\right) & \hat{s} \geq 0 \\ -2 \ln\left(\frac{P(s)}{P(0)}\right) & \hat{s} < 0, \end{cases} \quad (6-3)$$

In this work, the value of a physical signal should not be negative. When the MC estimator of signal \hat{s} is negative, we set the value of signal \hat{s} to be zero rather than negative.

We calculated the observed $t_{s,obs}$, as shown in Fig. 6.1. Two simple examples were used to validate the analysis method. We scanned the hypothesized value from 0 to 6 and

fitted the data to get the best values. The result shows that the likelihood-based analysis method can work properly.



- (a) Expected background events: $b = 4$ and observed events: $n = 3$. The background is higher than the observed signal candidates. The signal of fitting result is close to 0.
- (b) Expected background events: $b = 4$ and observed events: $n = 5$. The background is less than the observed signal candidates. The signal of fitting result is close to 1.

Figure 6.1 Two simple examples validate the likelihood-based function used in the thesis.

We defined a test for a hypothesized value of s by using the statistic t_s directly to measure the discrepancy between data and hypothesis. The higher values of t_s corresponded to the more significant disagreement. To quantify the level of disagreement, we computed the p -value,

$$p_s = \int_{t_{s,obs}}^{\infty} f(t_s|s) dt_s, \quad (6-4)$$

where $t_{s,obs}$ is the statistic observed, while $f(t_s|s)$ denotes the pdf of t_s under the assumption of the signal s . Figure 6.2 illustrates the sketch map. A more detailed description is as follows. Firstly, we got a maximum likelihood estimated from the data. Secondly, we calculated the p -value using the pdf $f(t_s|s)$. Thirdly, we scanned different s values and got a series of $t_{s,obs}$. In the meantime, the pdf $f(t_s|s)$ was also changing with the s value. Finally, we got an s value that could lead to the $p_s = 10\%$ in the pdf $f(t_s|s)$.

Besides the simple verification discussed above, our results are comparable with those used Feldman method^[111], as seen in Table 6.1. Both are consistent.

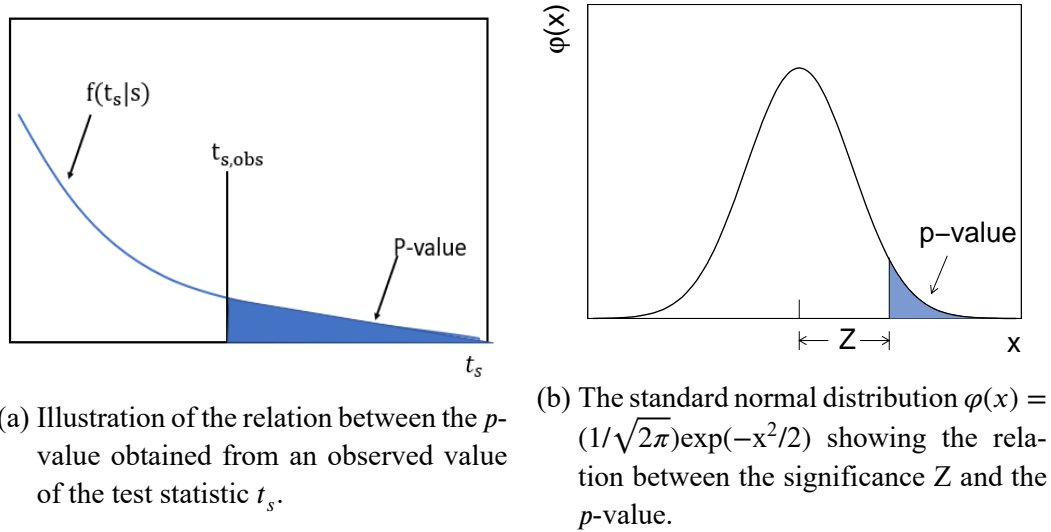


Figure 6.2 Illustration of the relation between the p -value and the observed t_s and also with the significance Z .

Table 6.1 The 90% C.L. and 95% C.L. intervals for the Poisson signal mean s (for total observed events n , and known mean background b ranging from 0 to 7). Our results s are indicated by the “P-L”, and Feldman’s result^[111] s are by the “F-C”, respectively.

(n,b)	Method	(0,0)	(1,1)	(2,2)	(3,3)	(4,4)	(5,5)	(6,6)	(7,7)
90% C.L.	P-L	2.4	3.3	3.9	4.4	4.6	5.0	5.5	5.5
	F-C	2.4	3.4	3.9	4.4	4.6	5.0	5.5	5.5
95% C.L.	P-L	3.1	4.1	4.7	5.2	5.7	6.2	6.7	6.8
	F-C	3.1	4.1	4.7	5.3	5.8	6.3	6.8	6.8

6.1.2 Maximum likelihood fitting

In the analysis, Figure 6.3 shows the data flow structure we used to calculate the neutrino fluence. The IBD data consists of the nGd and nH samples, each of which includes the data from eight ADs at Daya Bay. There are a total of sixteen data sources for the monochromatic spectra. What is more, for the Fermi-Dirac spectra, the sample is divided into two parts: low-energy ($E_p < 10$ MeV) and high-energy ($E_p > 10$ MeV). There are a total of thirty-two data sources for the Fermi-Dirac spectrum. We combined multiple data sources to calculate the neutrino fluence, mainly based on the following considerations.

- Improve the statistics by combining both the nH and nGd samples.
- Feature of multiple ADs located in the separated locations at Daya Bay.
- Suppress the effect brought by reactor neutrinos using $E_p > 10$ MeV.

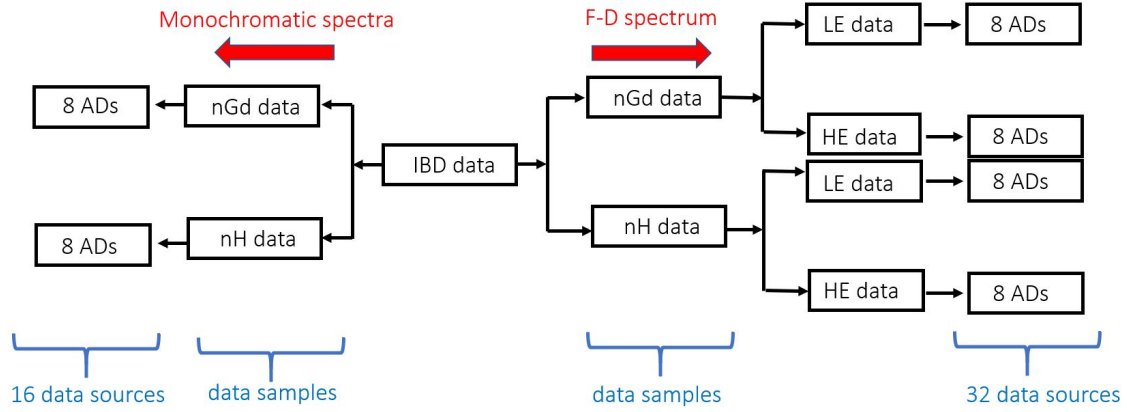


Figure 6.3 Data sources and structure in the analysis. “LE” represents low energy region ($E_p < 10$ MeV). “HE” represents high energy region.

Fig. 6.4 shows the summary flow chart to calculate the upper limits of $\bar{\nu}_e$ fluence in the analysis.

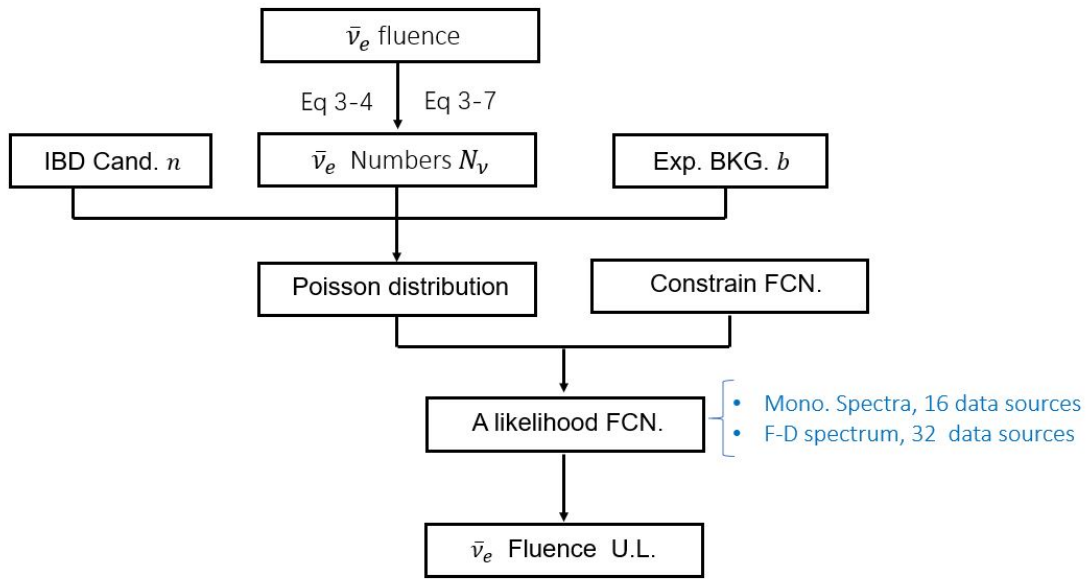


Figure 6.4 Flow chart of the $\bar{\nu}_e$ fluence calculation. “IBD. Cand.” represents observed IBD candidates. “Exp. BKG.” represents expected background events. “FCN” represents function. “U.L.,” represents upper limit.

Equation (3-4) and (3-7) were used to calculate the neutrino fluence under two energy spectra. We created a Poisson distribution using the fluence $F(E_\nu)$ for each data source.

$$P(F(E_\nu)) = \frac{(N_\nu + b_i^t)^{n_i}}{n_i!} e^{-(N_\nu + b_i^t)}, \quad (6-5)$$

where N_ν is the number of $\bar{\nu}_e$ s' within the specific energy interval, b_i is the number of predicted background events, b_i^t is the number of actual background events, and n_i is the number of observed IBD candidates.

To constrain the nuisance parameters, we introduced $C(b_i^t)$,

$$C(b_i^t) = \frac{1}{\sqrt{2\pi\sigma_i^2}} e^{-\frac{(b_i-b_i^t)^2}{2\sigma_i^2}}, \quad (6-6)$$

where σ_i is the statistical error for the predicted background. The likelihood function is the product of Poisson distribution and Gaussian constraint distribution for all data sources.

$$L(F(E_\nu), b_i) = \prod_{i=1}^N P(F(E_\nu)) \times C(b_i^t), \quad (6-7)$$

where N is 16 for the monochromatic spectra and 32 for the Fermi-Dirac spectrum. If the maximum likelihood estimator, $\hat{F}(E_\nu) < 0$, we set $F(E_\nu) = 0$. We then constructed a test statistic:

$$t_{F(E_\nu)} = \begin{cases} -2 \ln \frac{L(F(E_\nu), \hat{b}_i(F(E_\nu)))}{L(\hat{F}(E_\nu), \hat{b}_i)} & \hat{F}(E_\nu) \geq 0 \\ -2 \ln \frac{L(F(E_\nu), \hat{b}_i(F(E_\nu)))}{L(0, \hat{b}_i(0))} & \hat{F}(E_\nu) < 0, \end{cases} \quad (6-8)$$

where $\hat{b}_i(F(E_\nu)), \hat{b}_i(0)$ refer to the conditional maximum-likelihood estimators of b_i ^[110]. As was done with the statistic $t_{F(E_\nu)}$, we quantified the level of disagreement between the data and the hypothesized value of $F(E_\nu)$ with the p -value.

$$p_{F(E_\nu)} = \int_{t_{F(E_\nu),obs}}^{\infty} f(t_{F(E_\nu)}|F(E_\nu)) dt_{F(E_\nu)}, \quad (6-9)$$

where $t_{F(E_\nu),obs}$ is the value of the statistic, $t_{F(E_\nu)}$, observed from the data, and $f(t_{F(E_\nu)}|F(E_\nu))$ denotes the pdf of $t_{F(E_\nu)}$ under the assumption of the signal strength, $F(E_\nu)$. Finally, we obtained the fluence of anti-neutrinos.

6.2 Data analysis

Firstly, we checked the Daya Bay experiment shift records during the GW events burst time and expected to exclude the possibilities of non-physical events. For the GW150914, GW151012, and GW151226, the experiment was in regular operation. For the GW170104 event, EH1 was under the calibration process, and the signal rate was unstable, so we had to remove it from our analysis. During GW170608, GW170814, and GW170817, other experiments were using AD1 in the EH1. Until now, only the rest 7 ADs are in the right working conditions. From September 2015 to August 2017, there are a total of seven GWs analyzed in the thesis. Fig. 6.5 shows the IBD candidates observed for each GW within ± 1000 s. The GW events time distribution in our analysis can be seen in the plot.

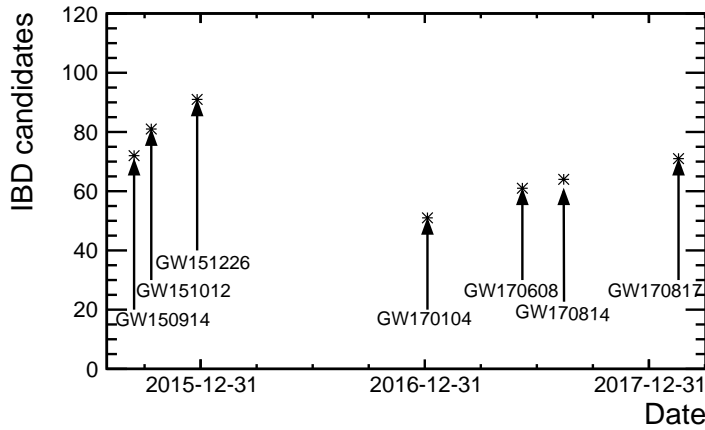


Figure 6.5 Distribution of IBD candidates of each GW within ± 1000 s.

6.2.1 Search time windows

The emitting sequence of neutrinos and GWs is not clear, and the duration of the neutrino burst is also uncertain because of the absence of neutrino emission information. We decided to exploit the multiple time windows to search for neutrino signals associated with GWs. We adopted three different search time windows, namely ± 10 s, ± 500 s, and ± 1000 s according to different physical motivations. We described how to determine the search time window in detail below.

- **± 10 s** The observation of supernova neutrino SN1987A is a well-known astrophysical event. It is the only time to measure the neutrinos up to now. Core-collapse supernovae would emit a tremendous number of neutrinos on a time scale of 10

seconds. Although we are not clear about the physical mechanism of BH mergers, we suspected that they might have the same physical process. We adopted a time window of ± 10 s to search for the neutrino candidates.

- **± 500 s** The neutrino signals were assumed to be within ± 500 s around the GW detection time, which comes from the time difference^[112] between GW events emission and neutrino emission predicted. Figure 6.6 shows a summary emission process for the time window ± 500 s. Before the GRB broke out or a precursor happened, there is a 100 s time window to activate the central engine. After the activity of the central engine, there is a 250 s precursor emission time window. Moreover, the duration time of most GRBs is about 150 s. Both neutrinos and GWs emission are possible within the whole time window ± 500 s.

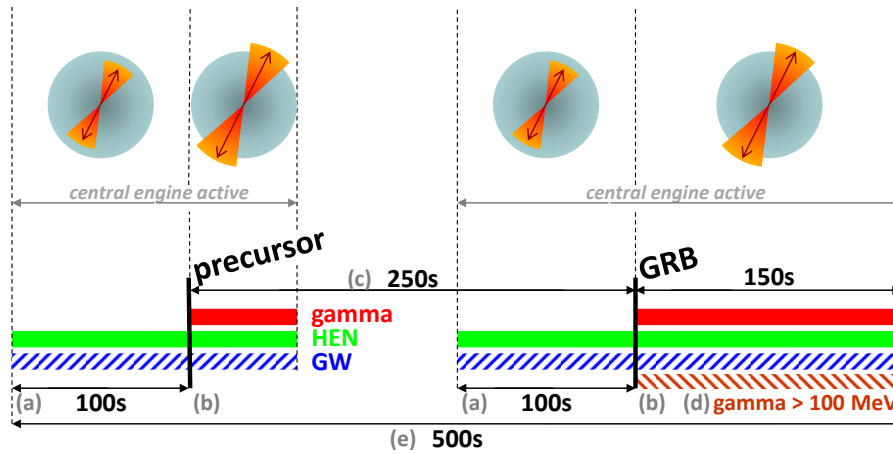


Figure 6.6 Summary of the coincidence time of the neutrinos and the GW emission. (a) There is a 100 s time window to activate the central engine before breaking out. (b) The relativistic jet breaks out from the envelope. (c) The duration time has 250 s precursor before the GRB breaks out. (d) The main GRB burst time window is ~ 150 s. (e) The whole time is ± 500 s when both neutrinos and GWs emission may happen. (From Ref.^[112]).

- **± 1000 s** We chose an even large window of ± 1000 s to account for most long GRB events that lasted less than 1000 s. The duration time T_{90} of GRBs detected by BATSE is shown in Fig. 1.10. GRBs may accompany the generation of neutrinos at any time. This window can avoid missing important information because of the unknown of BH-BH.

6.2.2 Data sample

The raw data came from P17B data reconstructed with the AD-simple method in the background analysis. Figure 6.7 draws a detailed IBD candidate selection flow chart, while Table 5.1 summarizes selection criteria. We have described the evaluation of the detection efficiency adopting the selection criteria in the previous chapter.

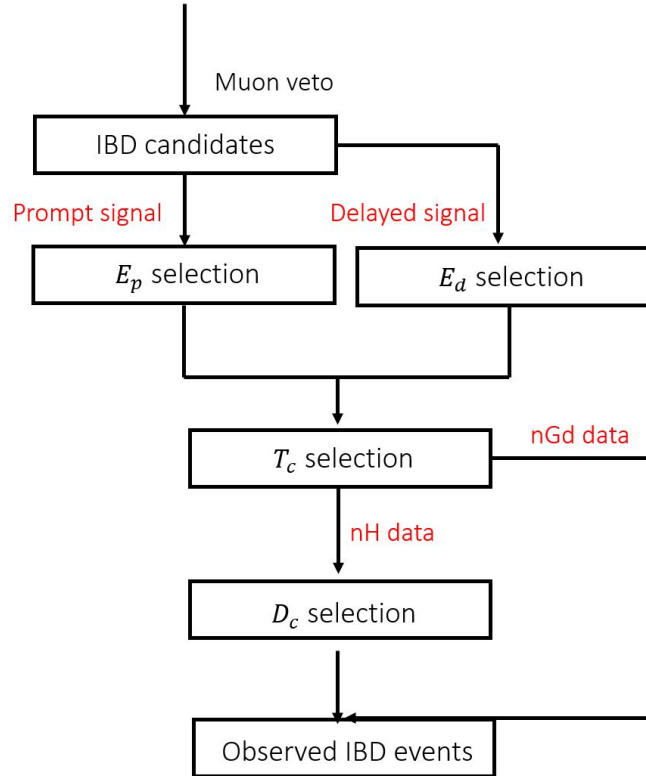


Figure 6.7 Observed IBD events survived from the IBD selection criteria at Daya Bay.

The data samples in all three halls were processed together. Figure 6.8 shows the distribution of prompt energy and delayed energy for both the nGd and nH samples, while Figure 6.9 shows the coincidence time between the prompt and delayed signals. For the nGd and nH sample, the coincident time windows T_c is $[1, 200] \mu\text{s}$ and $[1, 400] \mu\text{s}$, respectively. Figure 6.10 shows the distance D_c from the prompt and delayed signal vertexes. We only applied the coincidence distance cut for the nH sample because of more accidental backgrounds involved. We concluded that our analysis's selection criteria could reject most of the background and select the IBD candidates from these plots.

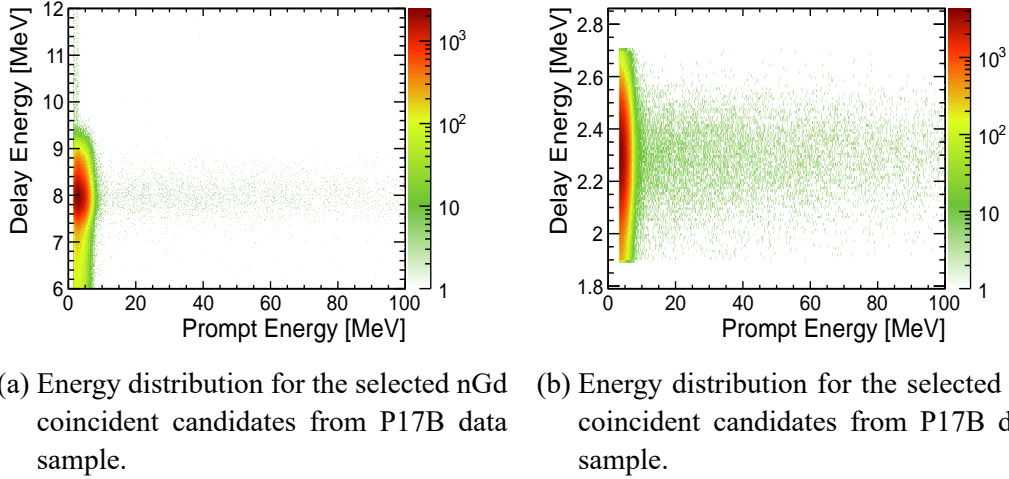


Figure 6.8 Energy distribution of the prompt energy versus the delayed energy from the P17B data sample.

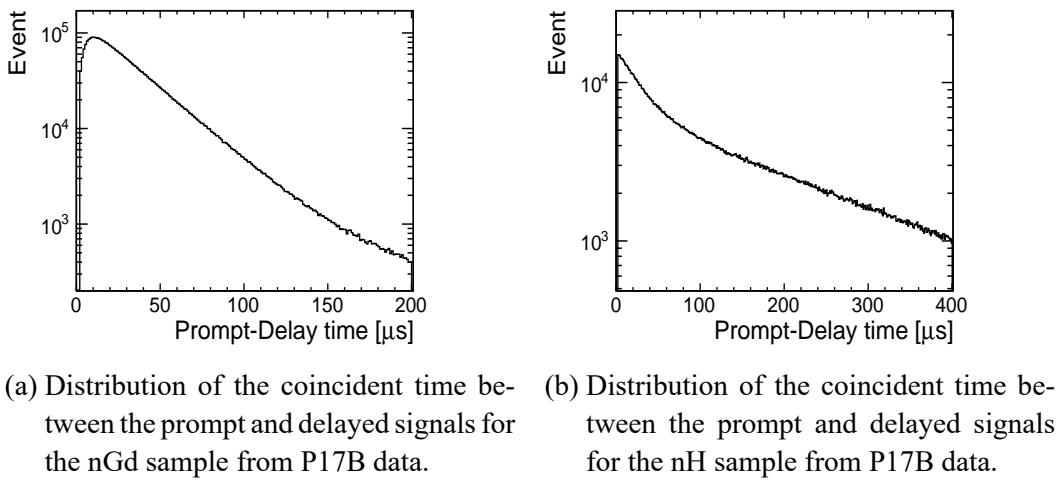


Figure 6.9 Distribution of the coincident time for the nGd and the nH.

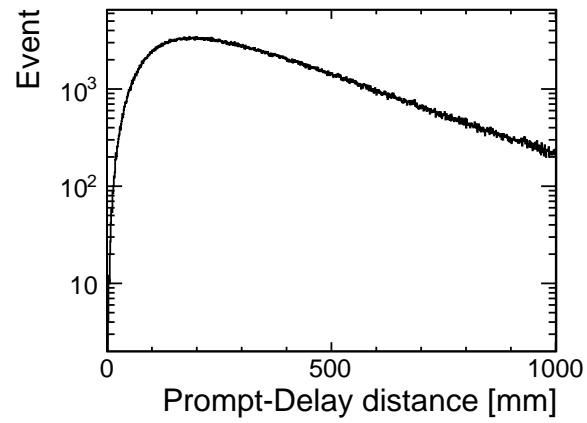


Figure 6.10 Distribution of the coincident distance between the prompt signal vertex and the delayed signal vertex for the nH from P17B data sample.

6.2.3 Background estimation

Because the GWs are the instantaneous events, we adopted a statistical background of the GW arrival time ± 5 days to estimate the background events. We first checked the stability of the IBD event rate within ± 5 days of each GW event. The data samples were divided into four parts to cover all the data we used, namely nGd low-energy ($0.7 \text{ MeV} < E_p < 10 \text{ MeV}$), nH low-energy ($3.5 \text{ MeV} < E_p < 10 \text{ MeV}$), nGd high-energy ($10 \text{ MeV} < E_p < 90 \text{ MeV}$), and nH high-energy ($10 \text{ MeV} < E_p < 90 \text{ MeV}$).

We listed the IBD event rates of GW150914, GW151012, GW151226, GW170104, GW170608, GW170814, and GW170817 in Fig. 6.11, 6.12, 6.13, 6.14, 6.15, 6.16, and 6.17, respectively. It can be seen that the IBD event rate is higher at EH1 and EH2 because of the closer distance to the reactors. For the GW170104, EH1 was not working normally and removed from the rate stability check. For the GW170608, GW170814, and GW170817, the rate in EH1 is lower than EH2 due to only one AD working. Furthermore, for the GW170814, there is a blank in the rate because of the detector switch. All IBD event rates associated with the GW events were stable and had no protrusions within a ± 5 days time window, which met our GW analysis requirement. For the GW170104 event, the time window was not ± 5 days, but $(-1, +5)$ days, because some data was missing at Daya Bay.

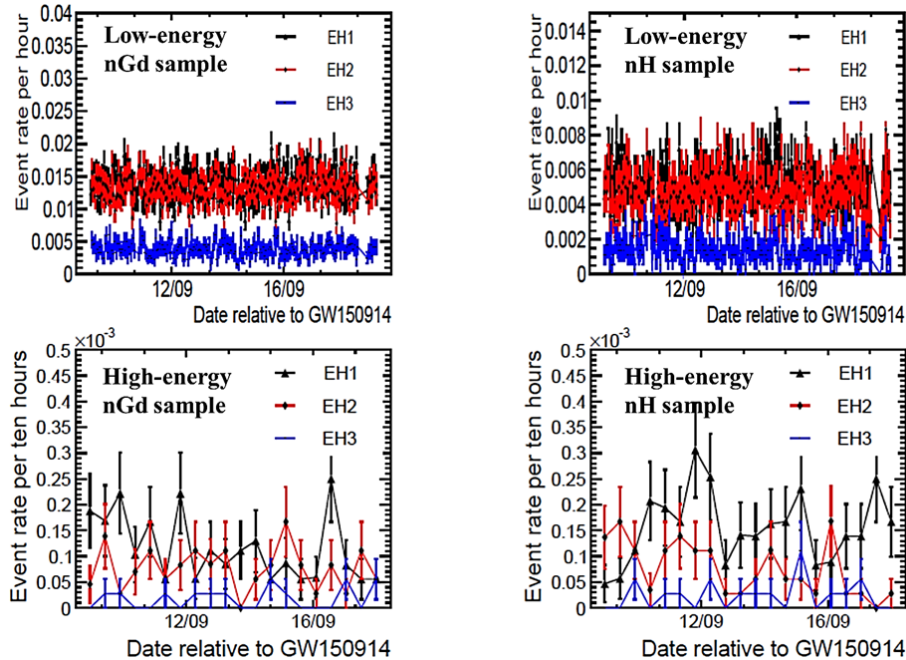


Figure 6.11 Distribution of the IBD event rates for the low-energy and high-energy events within ± 5 days of the GW150914 arrival time. The errors are statistical only.

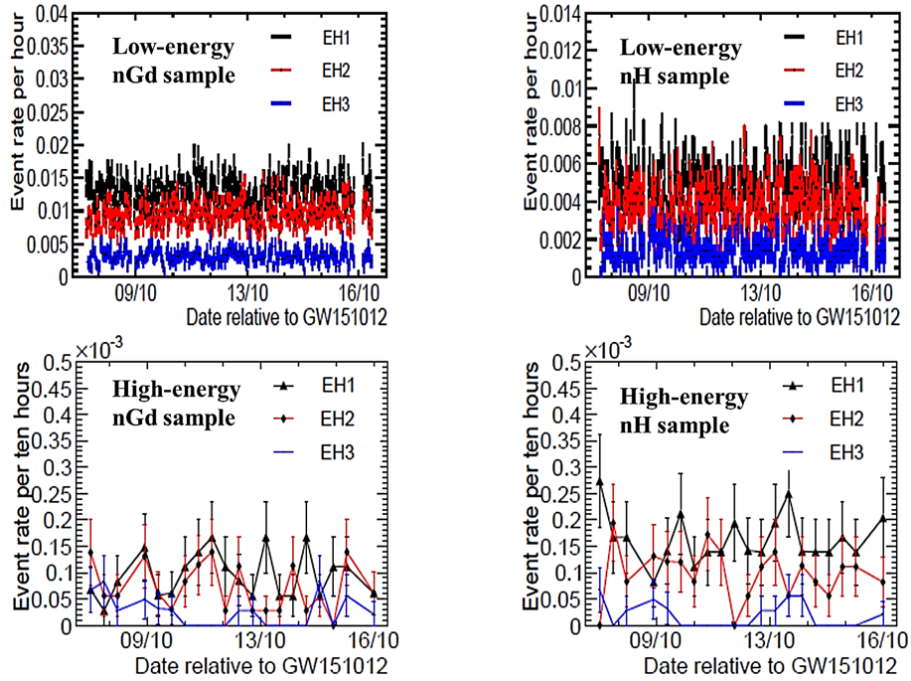


Figure 6.12 Distribution of the IBD event rates for the low-energy and high-energy events within ± 5 days of the GW151012 arrival time. The errors are statistical only.

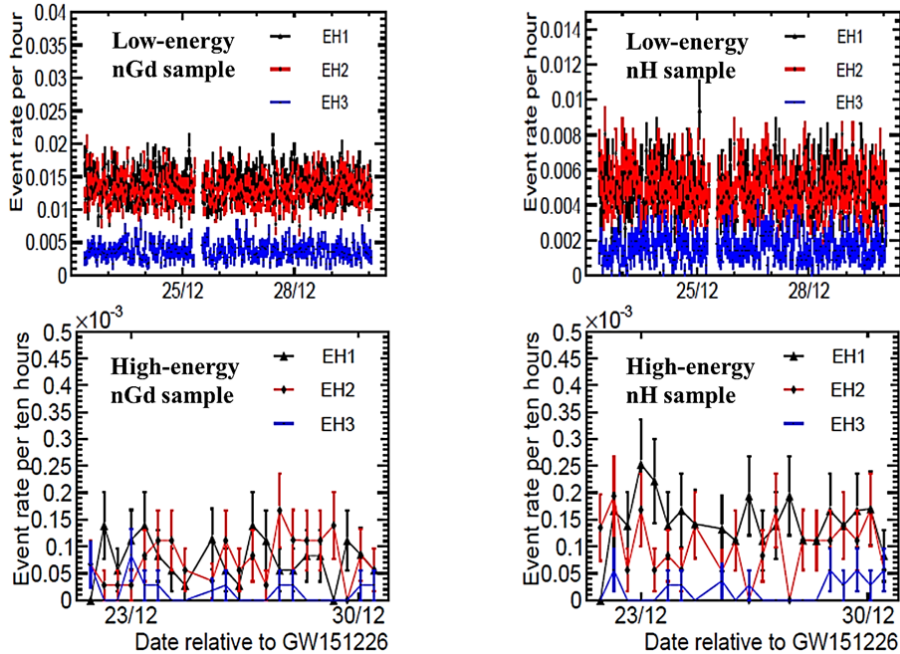


Figure 6.13 Distribution of the IBD event rates for the low-energy and high-energy events within ± 5 days of the GW151226 arrival time. The errors are statistical only.

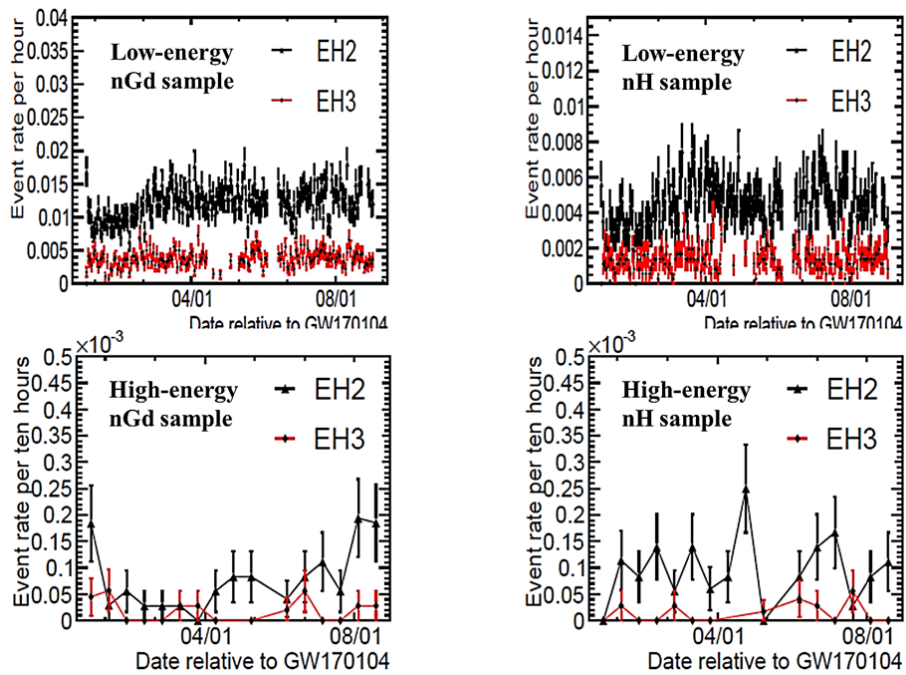


Figure 6.14 Distribution of the IBD event rates for the low-energy and high-energy events within (-1, +5) days of the GW170104 arrival time. Detectors were turned off for a few days, which lead to the absence of some data. Furthermore, EH1 was not working normally and removed from the rate stability check. The errors are statistical only.

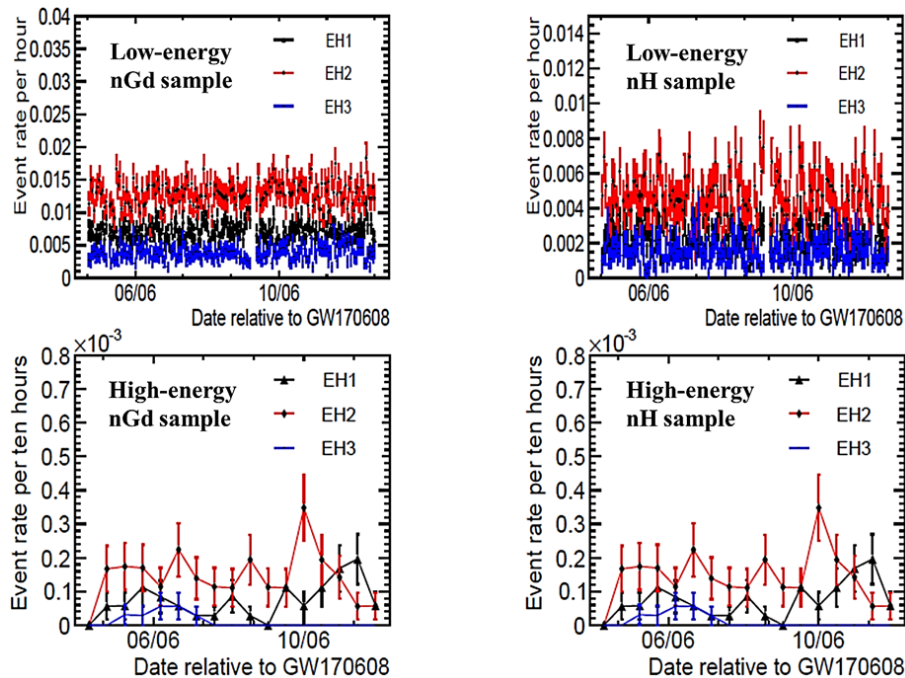


Figure 6.15 Distribution of the IBD event rates for the low-energy and high-energy events within ± 5 days of the GW170608 arrival time. The rate in EH1 is lower than EH2 due to only one AD working. The errors are statistical only.

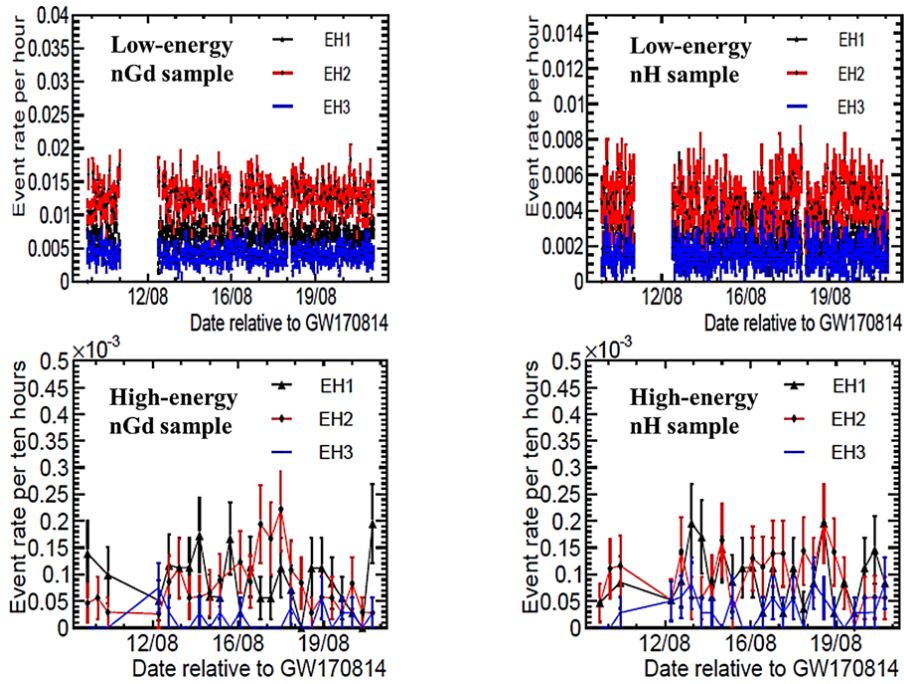


Figure 6.16 Distribution of the IBD event rates for the low-energy and high-energy events within ± 5 days of the GW170814 arrival time. The rate in EH1 is lower than EH2 due to only one AD working. There is a blank in the rate because of the detector switch. The errors are statistical only.

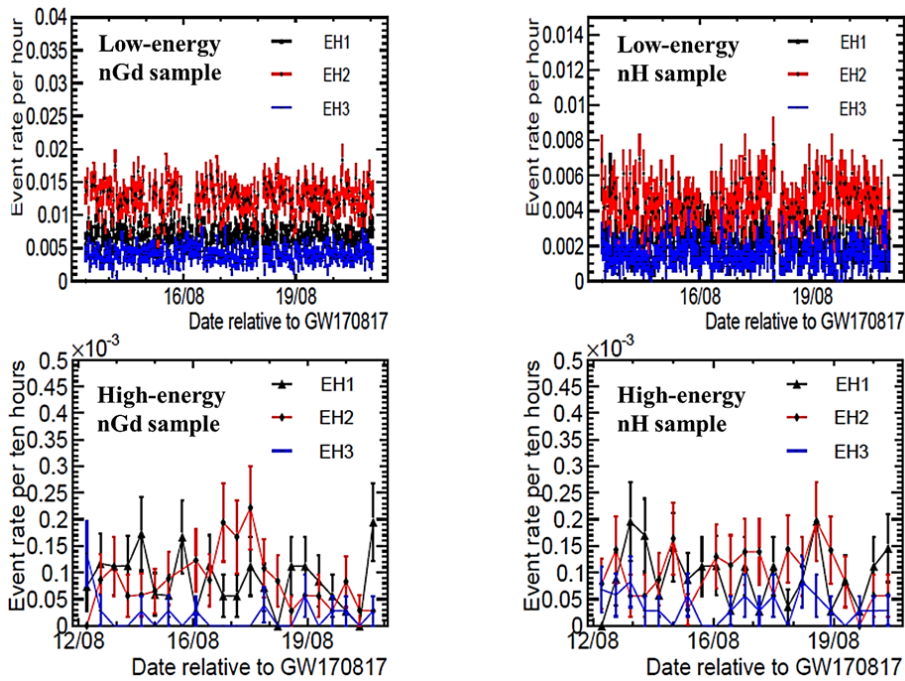


Figure 6.17 Distribution of the IBD event rates for the low-energy and high-energy events within ± 5 days of the GW170817 arrival time. The rate in EH1 is lower than EH2 due to only one AD working. The errors are statistical only.

In calculating the background rate, we removed the maximum signal search time of 1000 s within the ± 5 days. The expected number of background events in the specified time window was:

$$b_i = T_w \times R_i, \quad (6-10)$$

where T_w is the search time window, namely ± 10 s, ± 500 s, and ± 1000 s. R_i is the background event rate around the GW burst time, and b_i is the expected background numbers.

For a specified $\bar{\nu}_e$ energy of 5, 7, 10, 20, 30, 50, 70, 90 MeV, the search energy range was set to $E_p \pm 5\Delta$ under the monochromatic spectra. For the low-energy energy points, namely 5, 7, 10 MeV, the background rate of R_i was determined using the data collected around the GW arrival time within ± 5 days. For the high-energy points, namely 20 MeV, 30 MeV, 50 MeV, 70 MeV, and 90 MeV, the background rate was determined by integrating the energy range $E_p \pm 5\Delta$ using the prompt spectrum, as shown in Fig. 6.18, because of very few high-energy events existed within ± 5 days of GW related time.

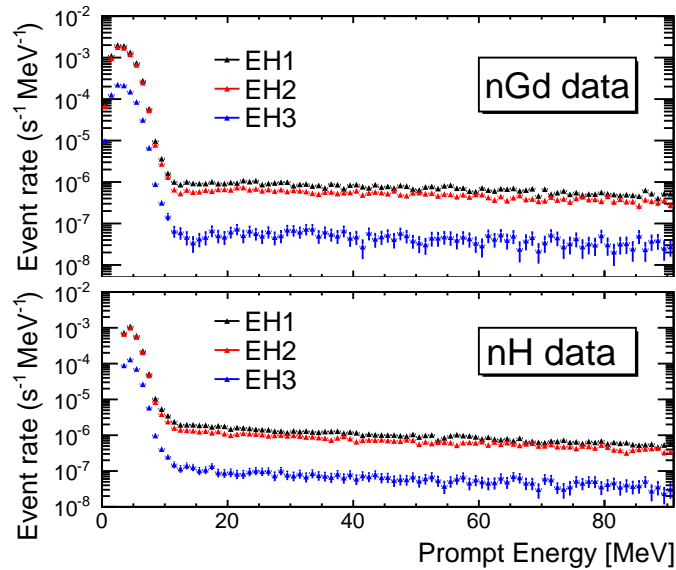


Figure 6.18 Prompt energy spectra of IBD candidates using the P17B data. The statistical uncertainty is considered.

For the Fermi-Dirac spectrum, the background rate of R_i was determined using the data correlated with GW events within ± 5 days. The expected background events were calculated for the low-energy, high-energy of the nGd and nH samples, respectively.

6.2.4 IBD candidates

We selected IBD candidates for monochromatic and the F-D spectra, respectively.

6.2.4.1 IBD candidates under monochromatic spectra

In this section, we give the search results assuming the monochromatic spectra. Figure 6.19 presents the search results of IBD candidates and the expected background events in all EHs. The black markers represent the number of IBD candidates observed at discrete neutrino energy under different time windows, while red markers represent the expected background levels. It is seen that the IBD candidates are consistent with the expected background events. The detailed results of 5, 7, and 10 MeV neutrinos within ± 500 s time window were listed in Appendix Table D.1, D.2, and D.3, respectively. For the high-energy points, namely 20 MeV, 30 MeV, 50 MeV, 70 MeV, and 90 MeV, no IBD candidates were observed, and the background is listed in Table D.4. We also give IBD candidates of ± 10 s and ± 1000 s time windows in Appendix Table D.5. The expected background events of ± 10 s and ± 1000 s time windows were obtained by multiplying the factors of 0.02 and 2 to the averaged ones of ± 500 s, respectively.

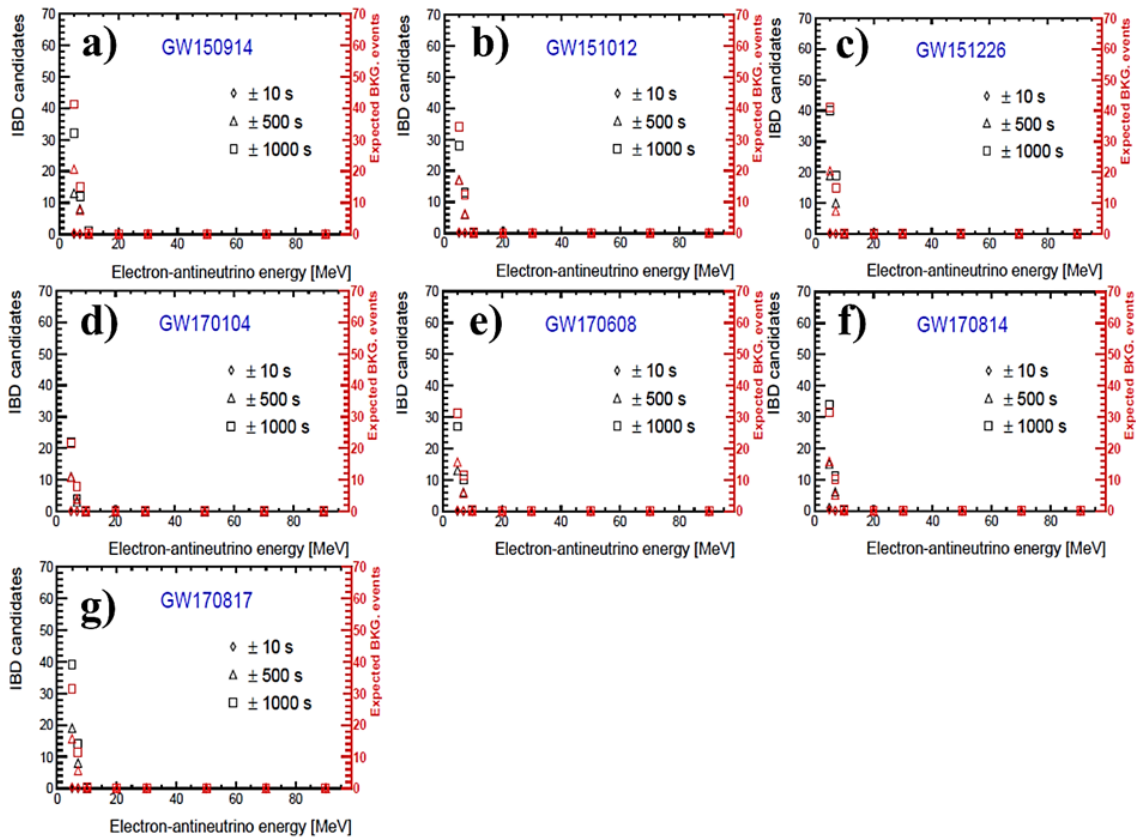


Figure 6.19 Energy distribution of IBD candidates and expected background events of all GW events assuming the monochromatic spectra

6.2.4.2 IBD candidates under the Fermi-Dirac spectrum

In the low-energy range ($E_p < 10$ MeV), the main background is the reactor neutrinos. In the high-energy ($E_p > 10$ MeV), the background is dominated by fast neutrons. We gave the average background rate over the ADs in each hall in Table 6.2. The detection time and IBD candidates met all data selection criteria of all GW events are shown in Fig. 6.20, 6.21, 6.22, 6.23, 6.24, 6.25, and 6.26.

Table 6.2 Average background rate (per second per antineutrino detector) for the studied energy spectrum (Low E: $E_p < 10$ MeV, High E: $E_p > 10$ MeV).

	EH1	EH2	EH3
nGd			
Low E	$(7.65 \pm 0.01) \times 10^{-3}$	$(6.82 \pm 0.01) \times 10^{-3}$	$(8.45 \pm 0.01) \times 10^{-4}$
High E	$(6.35 \pm 0.04) \times 10^{-5}$	$(4.32 \pm 0.04) \times 10^{-5}$	$(3.83 \pm 0.01) \times 10^{-6}$
nH			
Low E	$(28.75 \pm 0.04) \times 10^{-4}$	$(25.76 \pm 0.03) \times 10^{-4}$	$(3.25 \pm 0.01) \times 10^{-4}$
High E	$(9.20 \pm 0.01) \times 10^{-5}$	$(6.30 \pm 0.01) \times 10^{-5}$	$(5.65 \pm 0.01) \times 10^{-6}$

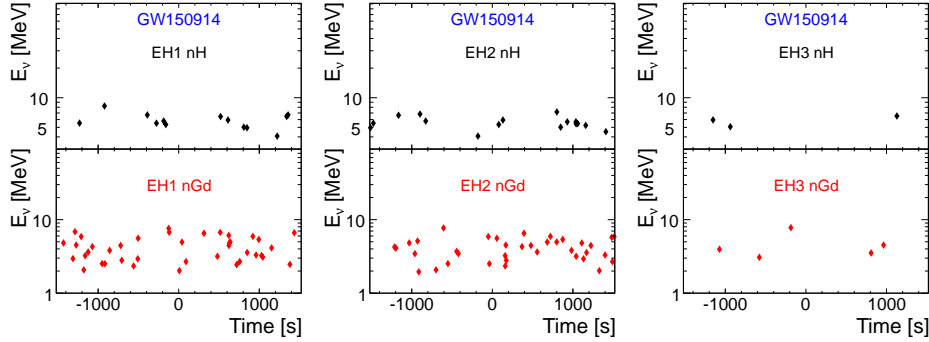


Figure 6.20 Neutrino energy and relative time distribution of IBD candidates for GW150914.

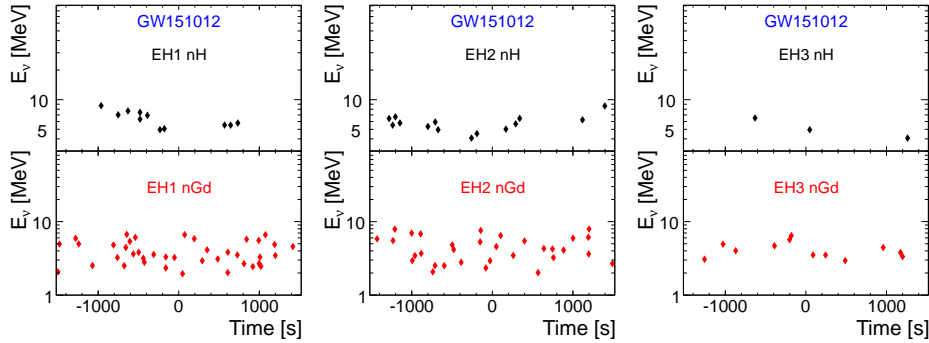


Figure 6.21 Neutrino energy and relative time distribution of IBD candidates for GW151012.

The detailed results of ± 500 s can be seen in Appendix Table D.6, Table D.7, D.8,

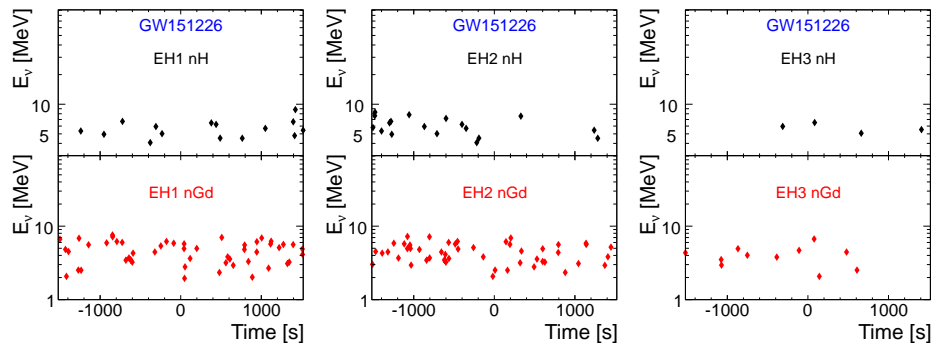


Figure 6.22 Neutrino energy and relative time distribution of IBD candidates for GW151226.

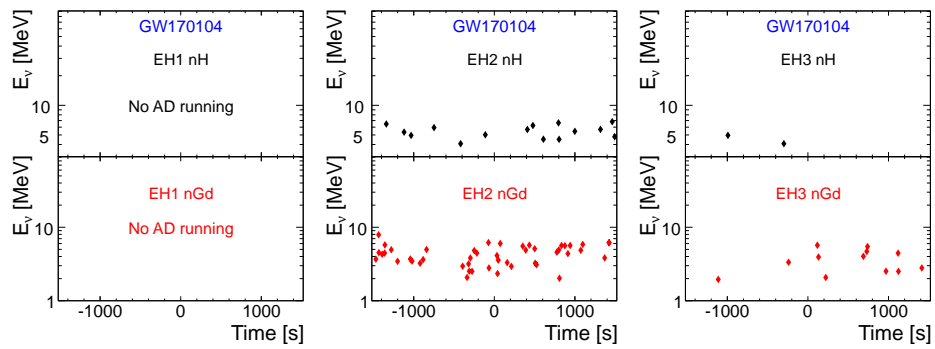


Figure 6.23 Neutrino energy and relative time distribution of IBD candidates for GW170104.

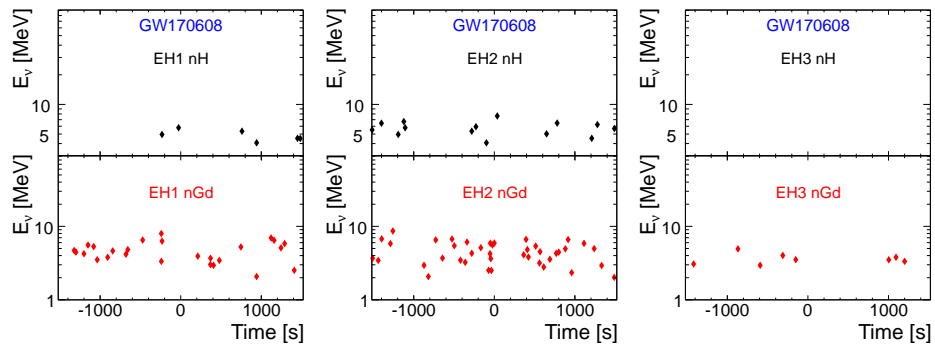


Figure 6.24 Neutrino energy and relative time distribution of IBD candidates for GW170608.

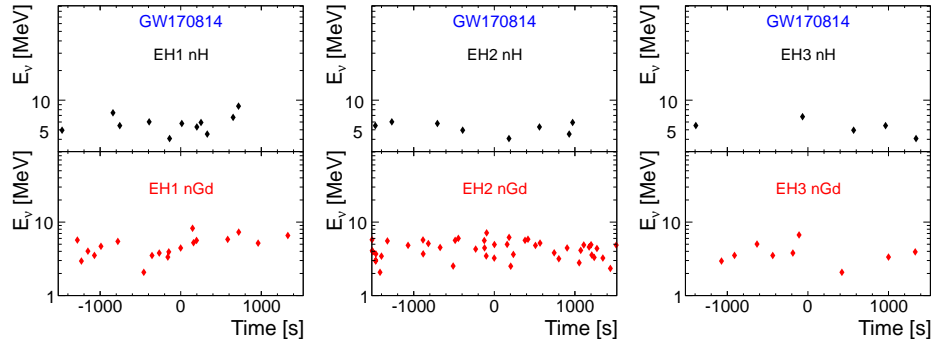


Figure 6.25 Neutrino energy and relative time distribution of IBD candidates for GW170814.

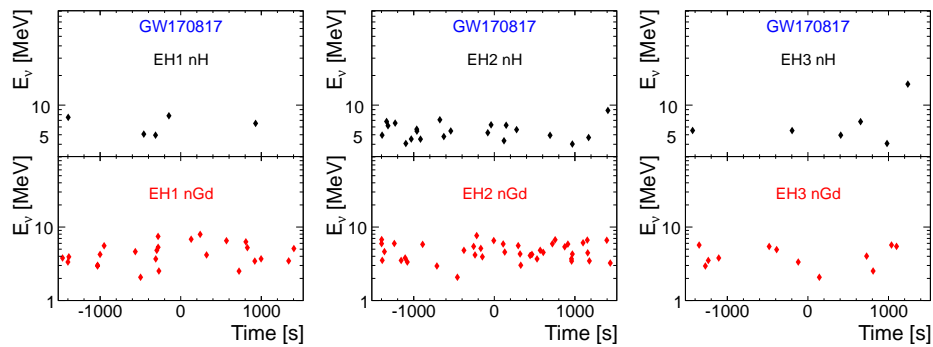


Figure 6.26 Neutrino energy and relative time distribution of IBD candidates for GW170817.

D.9, D.10, D.11, and D.12., each of which includes the observed IBD candidates and the expected background events for different data sources. The ± 10 s and ± 1000 s time windows were also adopted to search for IBD candidates. Appendix Table D.13 shows the IBD candidates of all GW events under two searching time windows in detail. The expected background events can be given by scaling the background events for the ± 500 s time window, which is the same as the background calculation under the monochromatic spectra. The background numbers for the ± 10 s and ± 1000 s time windows were from a multiplication of the factors of 0.02 and 2 using the averaged background numbers for the ± 500 s time.

6.2.5 Signal significance

This section focuses on the significance of the obtained GW signals. We first summarized all the GW events, as shown in Fig. 6.27. A time window ± 1500 s, which contains all three searching time windows, was selected to show all the neutrinos associated with all GW events. The origin of the x-axis represents the time when the GWs were detected. When the GWs occurred, the signals had not been observed, which exceeded the back-

ground events.

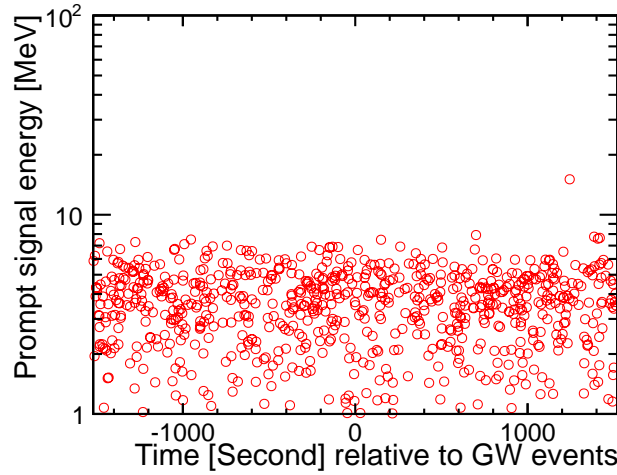


Figure 6.27 Summary of all the GW events within the time window ± 1500 s. The origin of the x-axis represents the time when the GWs were detected.

Also, we constructed a simple statistic to reflect the level of agreement between the observed and expected. There is no doubt that the most commonly used goodness-of-fit test is Pearson's χ^2 ,

$$\chi^2 = \sum_{i=1}^N \frac{(n_i - b_i)^2}{b_i}, \quad (6-11)$$

Where “ N ” is the number of combined data samples, as the same as the previous defined in equation 6-7, “ b_i ” is the expected background events, “ n_i ” is the number of candidates. For the low-energy data sample, the statistics will follow a χ^2 distribution. The hypothesis is that no neutrino signal comes from GW events. A larger χ^2 corresponds to a more significant discrepancy between the data and the hypothesis. The P -value or significance level is therefore given by integrating the χ^2 distribution from the observed χ^2 to infinity,

$$P = \int_{\chi^2}^{\infty} f(z; n_d) dz. \quad (6-12)$$

Where n_d is the degree of freedom. The larger χ^2 , the smaller p -value. In other words, the smaller p -value means the more significant signal. However, for low statistical data, one can not regard this as an observation of a χ^2 distribution variable to compute the p -value. The corrected p -values could be obtained by determining the distribution of the statistic with a Monte Carlo program. It was done by generating the Poisson values n_i for each

bin based on the mean values b_i . And then, we computed and recorded the χ^2 values.

In the thesis, we selected 5 MeV and 7 MeV data within the search time window of ± 500 s to calculate the p -values. As can be seen in Table 6.3 and Table 6.4. The p -values for both $E_\nu = 5$ MeV and $E_\nu = 7$ MeV indicated that the GW associated neutrino candidates are consistent with the background numbers. Therefore, the 90% C.L. upper limits of anti-neutrino fluence were considered and given.

Table 6.3 The p -values of signal significance for the $E_\nu = 5$ MeV energy points assuming the monochromatic spectra. The “nH+nGd” represents the combined of nH and nGd data.

p -value	GW	GW	GW	GW	GW	GW	GW
	150914	151012	151226	170104	170608	170814	170817
nGd	0.97	0.39	0.53	0.76	0.51	0.76	0.88
nH	0.74	0.98	0.47	0.62	0.91	0.21	0.69
nH+nGd	0.96	0.84	0.54	0.80	0.83	0.47	0.90

Table 6.4 The p -values of signal significance for the $E_\nu = 7$ MeV energy points assuming the monochromatic spectra. The “nH+nGd” represents the combined of nH and nGd data.

p -value	GW	GW	GW	GW	GW	GW	GW
	150914	151012	151226	170104	170608	170814	170817
nGd	0.14	0.81	0.64	0.37	0.01	0.02	0.21
nH	0.78	0.17	0.19	0.37	0.76	0.36	0.67
nH+nGd	0.34	0.37	0.56	0.60	0.14	0.28	0.38

6.3 Results of $\bar{\nu}_e$ searches

This section introduces the upper limits of neutrino fluence associated with GWs. We first present the upper limits within different time windows, assuming the monochromatic spectra. And then, we give the upper limits, assuming the Fermi-Dirac spectrum. In the end, we discuss the neutrino luminosity and compare our results with other neutrino experiments.

6.3.1 Limits on $\bar{\nu}_e$ fluence

For the low-energy points, the search results were consistent with the background numbers assuming the monochromatic spectra. For the high-energy points, we did not observe any GW neutrino events. We averaged all the IBD candidates and the background

numbers associated with GW events in three time windows. Upper limits of fluence at 90% C.L. for three time windows are shown in Table 6.5 and Fig. 6.28. For $E_\nu > 30$ MeV, the upper limit difference is far less than our scanning accuracy. Although three time windows will result in different numbers of background for $E_\nu > 30$ MeV, the upper limit difference is far less than the accuracy of our scanning. To facilitate the quick calculation and verification of our fluence results, we summarized all relevant parameters in Appendix Table E.1 and Appendix Table E.2 within the time window ± 500 s.

Table 6.5 Upper limits of fluence at 90% C.L. for three search time windows. The numbers of IBD candidates associated with the GW events and the background were averaged at Daya Bay.

$F_D(\bar{\nu}_e) (\times 10^{10} \text{ cm}^{-2})$	Monochromatic Spectra								
	E_ν (MeV)	5	7	10	20	30	50	70	90
± 10 s	11.2	3.5	1.3	0.25	0.16	0.05	0.02	0.01	
± 500 s	20.4	10.6	1.7	0.35	0.16	0.05	0.02	0.01	
± 1000 s	22.8	8.3	1.6	0.35	0.16	0.05	0.02	0.01	

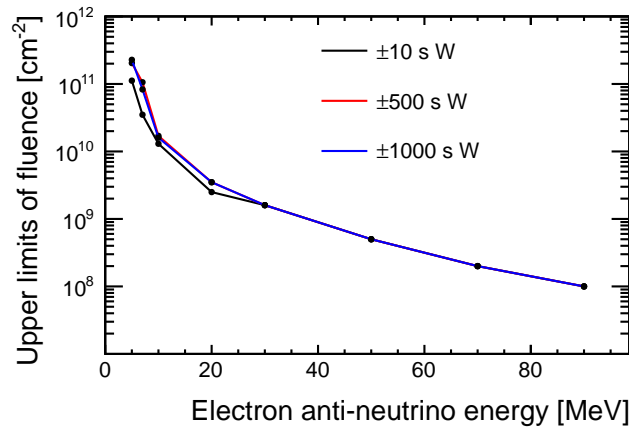


Figure 6.28 90% C.L. upper limit of the fluence of $\bar{\nu}_e$ from GW. The “W” in the plot means the time window.

For the Fermi-Dirac spectrum, within three time windows, ± 10 s, ± 500 s and ± 1000 s, the IBD candidates and the background numbers of all GW events were averaged to calculate the upper limits of fluences, as shown in Table 6.6. We summarized all the related-parameters within the ± 500 s time window in Appendix Table E.3.

Table 6.7 lists the detailed results of the ± 500 s search time window for the Fermi-Dirac spectrum. In the table of each GW event, the “nGd + nH” in the column of the low-energy (high-energy) represents the combination of nGd and nH data, which comes

Table 6.6 The 90% C.L. upper limits of neutrinos calculated by the averaged signal candidates and averaged background numbers of all GW events within three time windows assuming the Fermi-Dirac spectrum.

Time Window	± 10 s	± 500 s	± 1000 s
$F(\bar{\nu}_e)$	$0.55 \times 10^{10} \text{ cm}^{-2}$	$0.45 \times 10^{10} \text{ cm}^{-2}$	$0.42 \times 10^{10} \text{ cm}^{-2}$

from eight ADs. The “Low + High” in the nGd (nH) row represents the combination of low-energy and high-energy data. We concluded that as more data sources are combined, the upper limit is lower.

6.3.2 Limits on $\bar{\nu}_e$ luminosity

The upper limit on the total luminosity of electron anti-neutrinos is given by

$$L_{90} = F_{\bar{\nu}_e} \times 4\pi D_{\text{LIGO}}^2 \times \langle E_{\text{av}} \rangle, \quad (6-13)$$

where $F_{\bar{\nu}_e}$ is the neutrino fluence, D_{LIGO} is the distance from the source to the Earth, and E_{av} is the average neutrino energy, which corresponds to the specific energy for monochromatic spectra and 12.7 MeV for the Fermi-Dirac spectrum, respectively. In calculating the luminosity, we assumed that the $\bar{\nu}_e$ s are isotropic emissions, and all neutrino flavors emitted from sources have an equal contribution. In our thesis, we calculated the luminosity results of ± 500 s search time window assuming the Fermi-Dirac energy spectrum because of the convenient comparison with other neutrino experiments. Table 6.8 gives a detailed comparison with other experiments.

The different average energy of neutrinos used in various experiments leads to a little difference in upper limits. The average energy of neutrinos used in the KamLAND experiment was the same as ours at Daya Bay. The luminosity of the Borexino experiment was calculated, assuming $\langle E_{\nu} \rangle = 15.8$ MeV. In the experiment of Super-K, for GW150914 and GW151226 analysis, the Fermi-Dirac spectrum was replaced by a flat spectrum. The average energy of neutrinos was 40 MeV. For Super-K’s GW170817 analysis, the neutrino energy ranges from 3.5 MeV to 100 MeV, assuming the Fermi-Dirac spectrum, and the average energy was set to be 20 MeV. As indicated in Table 6.8, the sensitivity mainly depends on the target mass. Then, although the Daya Bay experiment’s target mass was only one-third of KamLAND’s target mass, our upper limits were still comparable with KamLAND’s ones: $\sim 0.4 \times 10^{10} \text{ cm}^{-2}$. This is because the Daya Bay experiment has multiple ADs, which can reduce the background induced by one single AD and improve

Table 6.7 Upper limits of $\bar{\nu}_e$ on 90% C.L. at Daya Bay associates with GW events based on the Fermi-Dirac spectrum within the search time window of ± 500 s (low-energy: $E_p < 10$ MeV, high-energy: $E_p > 10$ MeV). For each GW event, the values in the table are explained as follows. The “nGd + nH combine” in the column of the low-energy or high-energy represents the combination of nGd and nH data, which comes from eight ADs. The “Low + High combine” in the row of the nGd sample or nH sample represents the combination of low-energy and high-energy data. The final result in the last column and the last row for every GW event is calculated by the combination of low-energy nGd, low-energy nH, high-energy nGd, and high-energy nH.

GW Events	Fluence(cm^{-2}) $\times 10^{10}$	Low Energy	High Energy	Low + High combine
GW150914	nGd Sample	9.75	1.80	0.50
	nH Sample	8.80	2.07	0.74
	nGd+nH combine	4.05	0.90	0.24
GW151012	nGd Sample	82.5	1.70	1.80
	nH Sample	24.2	2.30	1.45
	nGd+nH combine	34.5	0.99	0.71
GW151226	nGd Sample	55.0	1.80	1.60
	nH Sample	40.2	2.10	1.84
	nGd+nH combine	32.5	0.90	0.69
GW170104	nGd Sample	75.0	2.30 *	2.18
	nH Sample	24.5	2.60 *	1.93
	nGd+nH combine	25.30	1.20	0.81
GW170608	nGd Sample	33.4	2.10 **	1.18
	nH Sample	9.8	2.30 **	0.89
	nGd+nH combine	7.10	0.99	0.32
GW170814	nGd Sample	58.7	1.99 **	1.71
	nH Sample	25.2	2.35 **	1.56
	nGd+nH combine	22.8	1.00	0.56
GW170817	nGd Sample	40.5	2.00**	1.47
	nH Sample	43.5	2.40**	2.07
	nGd+nH combine	28.7	1.00	0.65

*: For GW170104 event, the upper limit calculated by nH or nGd high energy data is higher than other GW events because of the GW170104 just has EH2 and EH3 data sample.

** : For GW170608, GW170814, GW170817 events, the upper limits calculated by nH or nGd high energy data are higher than the GW150914, GW151012, and GW151226. For GW170608, GW170814, and GW170817, EH1 just has one AD data sample.

the experiment's sensitivity significantly. It had been verified in Reference^[113]. The raw data was divided into low-energy and high-energy samples to exclude lots of reactor neutrino background. It also improves our sensitivity.

Table 6.8 Upper limits of luminosity (Unit: 10^{60} erg) on 90% C.L. associated with the GW events based on the Fermi-Dirac spectrum in the same time window ± 500 s. We summarized four experiment results. “–” represents that there are no experiments to calculate the neutrino fluence or luminosity.

Exp. E_ν	Daya Bay (1.8,100) MeV	KamLAND (1.8,111) MeV	Borexino (3.5,75) MeV	Super-K (3.5,75) MeV
GW150914 (410_{-180}^{+160} Mpc)	1.18	1.26	2.03	0.05
GW151012 (1100_{-500}^{+500} Mpc)	24.2	90.6	–	–
GW151226 (440_{-190}^{+180} Mpc)	4.19	1.71	2.35	0.03
GW170104 (880_{-390}^{+450} Mpc)	17.9	–	9.38	–
GW170608 (340_{-140}^{+140} Mpc)	1.07	–	–	–
GW170814 (540_{-210}^{+130} Mpc)	4.83	–	–	–
GW170817 (40_{-14}^{+8} Mpc)	0.03	–	–	4×10^{-4}

6.4 Chapter summary

In this chapter, to derive the upper limits of neutrino fluence associated with the GW events, we first verified the analysis method, which is consistent with the results published by Feldman results. Then we constructed a maximum likelihood method that can combine multiple data samples, namely nGd and nH samples, to calculate the upper limits of neutrino fluence at Daya Bay.

Three search time windows, namely ± 10 s, ± 500 s and ± 1000 s, were adopted due to different physical motivations, which allow us to avoid the uncertainty caused by the absence of neutrino emission from GW sources. The P17B data sample was checked to ensure the correctness of the IBD events selection in the thesis.

Subsequently, the background event rates were given around ± 5 days of each GW event under two neutrino energy spectra. Then we got the expected background event numbers and neutrino signal candidates. We constructed a simple Pearson's χ^2 to test the signal significance of the GW events. The results showed that there is no excess between the neutrino signal candidates and the expected background. The upper limits of neutrino fluence were given at a 90% confidence level.

We obtained the upper limits of neutrino fluence within three search time windows

under two energy spectra. The luminosity of GWs was also given and compared with other neutrino experiments within the search time window, ± 500 s. Although the target mass of Daya Bay is a sub-kilo-ton scale, we found that the upper limits were comparable with the kilo-ton scale neutrino experiments.

Chapter 7 Measurement of $\bar{\nu}_e$ associated with GRBs

This chapter details the analysis of GRB. We first present the GRB data set and their basic features observed during the operation of the Daya Bay experiment. Then we introduce search time windows of the GRBs and report search results of related-GRB IBD candidates under different assumptions of neutrino energy spectra. In the end, we give the upper limits on the $\bar{\nu}_e$ fluence.

7.1 Data analysis

7.1.1 GRBs data set

The detailed information of GRBs is from a system, namely GRBWeb^[114]. The system automatically receives and stores the GRBs from the GRB Coordinates of Network (GCN)^[115], which provides the GRBs' locations, the other transients information detected by the satellite experiments, and the reports of follow-up observations made by the ground-based and space-based instruments. The GRBWeb can provide per GRB burst information collected by the main GRB experiments. When a GRB is generated and detected by multiple satellites simultaneously, the definition of burst duration is from the most inclusive start and stop times^[116]. The satellite can determine each burst angular position and the small associated error. The parameters adopted to calculate the gamma-ray fluence are taken from Fermi^[117-118], Konus-Wind^[119], Suzaku^[120], Swift/BAT^[121] and INTEGRAL^[122].

During the operation time of the Daya Bay experiment, the reconstructed data of P17B and P19A are selected, which correspond to the time from December 2011 to March 2019. Table 7.1 provides the necessary information about the GRBs used in our study. For the GRB events observed, some recorded the burst duration time, T_{90} , and some recorded the redshift, z .

Table 7.1 Data summary for GRBs from December 2011 to March 2019. Numbers of GRBs with T_{90} were recorded in the GRBWeb. Numbers of GRBs with redshift z were recorded in the GRBWeb.

	All GRBs	GRBs with T_{90}	GRBs with z
Numbers	2225	1686	212

There are 1686 GRBs with the burst duration time T_{90} , including 930 long and 756 short ones. Figure 7.1 shows the distribution. The occurrence of the GRBs is uniform throughout the whole time axis, and there is no significant difference between the numbers of long and short GRBs.

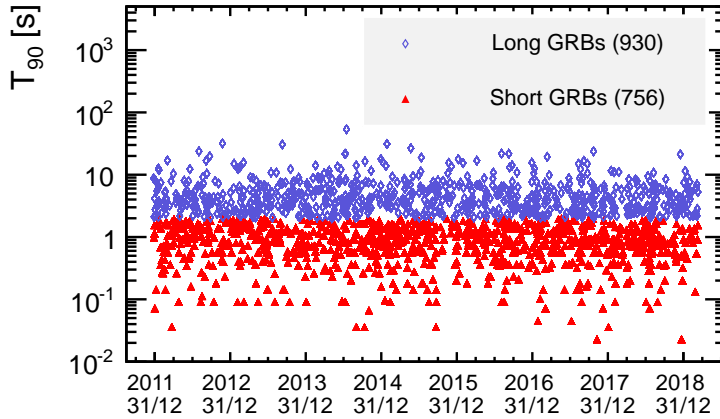
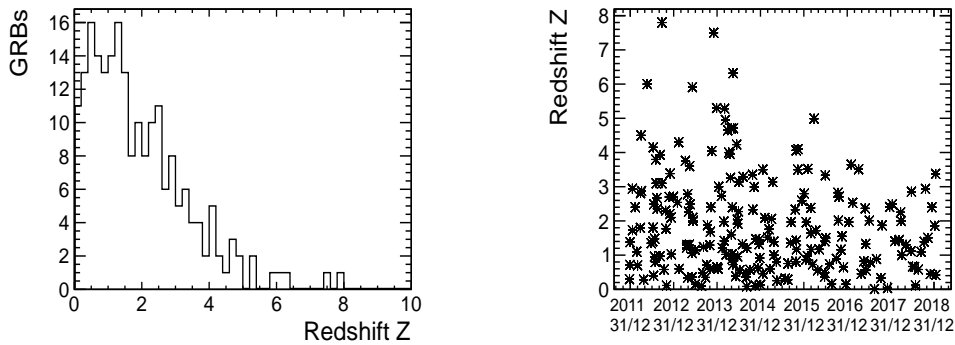


Figure 7.1 Distribution of 1686 GRBs with T_{90} from December 2011 to March 2019.

The redshift z is also an essential parameter for the GRB analysis, which is vital to determine the search time windows. Figure 7.2 shows the recorded redshifts and time for the 212 GRBs.



(a) Distribution of the 212 GRBs with redshift z . (b) Distribution of redshift z versus the date-time.

Figure 7.2 Redshift information of the 212 GRBs recorded. (a) shows the distribution of the 212 GRBs and (b) show the distribution of redshift versus the date-time.

The GRB redshift distribution indicates a peak at $z \approx 1$, and the average redshift is $z = 1.9$. Figure 7.3 shows the number of GRBs observed through the Daya Bay operation time, while Table 7.2 lists the detailed information of all detectors DAQ time and live-time.

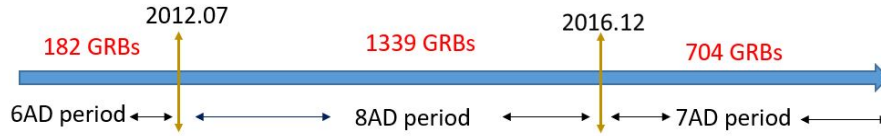


Figure 7.3 The number of GRBs observed in different Daya Bay operation time.

 Table 7.2 Running time of all detectors used in the GRB analysis during the Daya Bay operation time. T_f is the full-time of the detector operation. T_l is the live-time which has removed the detector dead time and the muon veto time, etc.

Days	Data	AD1	AD2	AD3	AD4	AD5	AD6	AD7	AD8
T_f	nGd	1544.41	2218.30	2224.28	2037.10	2225.48	2225.48	2225.48	2225.48
	nH	1544.41	2218.30	2224.28	2037.10	2225.48	2225.48	2225.48	2225.48
T_l	nGd	1234.49	1764.21	1860.69	1701.88	2186.31	2186.23	2185.85	2001.97
	nH	1186.20	1695.43	1805.77	1651.68	2179.81	2179.72	2179.35	1996.05

7.1.2 Search time windows

After obtaining all the GRBs data during the Daya Bay operation, we searched for the GRB-related IBD candidates. This section introduces three search time windows: two fixed time windows, namely ± 500 s and ± 1000 s, and a dynamic time window to search for the IBD candidates. We did not use the ± 10 s search time window adopted in the GW analysis because the GRB central region is opaque to gammas and transparent for neutrinos, leading to a more significant time difference between neutrino and gamma production.

7.1.2.1 Fixed time windows

- ± 500 s For the GRBs analysis, a search time window of ± 500 s is selected, which is determined by the time scale models and the neutrino flight time induced by the neutrino mass effect.

There are three models, including the core-collapse supernovae^[123-124], the neutron star merger^[125], and the cosmic string model^[56], which can generate the GRBs. All three models show that the time between neutrino emission and gamma emission is less than 10 s.

If we assume that the neutrinos and gammas can emit at the same time, we can express the delayed time of two signals as,

$$\frac{1}{2} \left(\frac{m_\nu}{E_\nu} \right)^2 \times T_{\text{gamma}}, \quad (7-1)$$

where T_{gamma} is the flight time of gammas. The sum of neutrino masses is limited to ≤ 0.23 eV by considering the cosmic microwave background (CMB), baryon acoustic oscillations, and CMB lensing^[126]. Moreover, the maximum mass is less than 0.087 eV from the neutrino oscillation experiments^[127-128]. A simple estimation of neutrino flight time is ~ 24 s for an 8 MeV neutrino from $z = 8.2$. Thus, a conservative time window of ± 500 s was chosen^[129].

- ± 1000 s We also selected another fixed search time window of ± 1000 s. The reason for choosing this time window is the same as the GW analysis. The longest GRB burst time is less than 1000 s, as shown in Fig. 1.10. Neutrino emission may occur at any time within this time window. Thus, we considered the most conservative time window of ± 1000 s.

7.1.2.2 Dynamic time window

In the previous analysis, the duration time of GRBs is between 0.01 s and 1000 s. When neutrino emission occurs at any time during the GRBs, choosing a dynamic time window related to the GRB duration rather than a fixed time window can significantly reduce the background. The coincident search time window, T_{DC} , which is determined by several terms, can be defined as follows^[72],

$$-t_p + T_{GRB} < T_{DC} < T_{GRB} + \Delta t_{GRB} + t_p + t_f(z), \quad (7-2)$$

where $t_p = 150$ s is the model-dependent time difference between neutrinos production and gamma production, T_{GRB} is the time detected by the detector on the earth, Δt_{GRB} is the GRB duration. $t_f(z)$ is the relativistic flight-time delay because of the non-zero neutrino mass,

$$t_f(z) = \frac{1}{2} \frac{m_{\bar{\nu}_e}^2}{E_{\bar{\nu}_e}^2} \int_0^z \frac{dz'}{(1+z')^2 H_0 \sqrt{\Omega_\Lambda + (1+z')^3 \Omega_m}}, \quad (7-3)$$

where cosmological observations, such as Wilkinson Microwave Anisotropy Probe (WMAP) and Sloan Digital Sky Survey (SDSS), give the absolute neutrino mass $m_{\bar{\nu}_e} = 0.6$ eV^[130]. The Λ CDM cosmological model parameters are: Hubble constant $H_0 = 69.6$ km/s/Mpc, the dimensionless matter densities $\Omega_M = 0.286$, and the dark energy densities $\Omega_\Lambda = 0.714$ ^[131]. The average neutrino energy $\langle E_{\bar{\nu}_e} \rangle = 12.7$ MeV, which have mentioned in Section 5. Fig. 7.4 shows all the GRBs recorded with the redshift, distribution of flight-time delay $t_f(z)$. The average redshift is $z = 1.9$, corresponding to the flight-time

delay $t_f(z) = 232.7$ s.

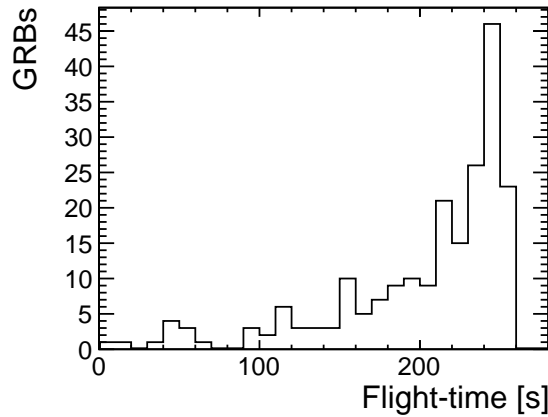


Figure 7.4 Relative flight-time delay distribution of the 212 GRBs recorded with the redshift.

In the analysis, we only used the GRBs recorded with the duration of burst time T_{90} . In such recorded 1686 GRBs, 99 GRBs have burst duration time T_{90} and redshift z . For the GRBs without redshift recorded, we adopted the average redshift instead.

7.1.3 Selected GRBs

This section introduces the signal window and the background window. Furthermore, we present how to define the overlap of different signal windows in the time axis.

As shown in Fig. 7.5, the search time window “Begin” corresponds to the different search time windows, -500 s, -1000 s, and $-T_{\text{Dyna}}$, respectively. The “End” represents the search time window, $+500$ s, $+1000$ s, and $+T_{\text{Dyna}}$, respectively. The “GRB trigger” represents the GRB burst time.

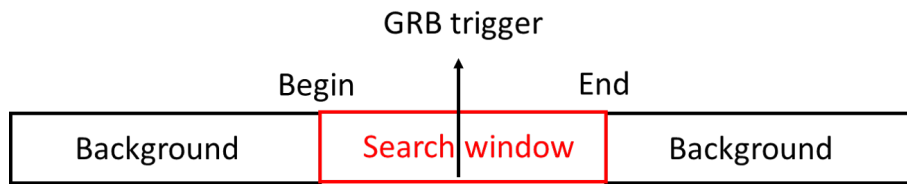


Figure 7.5 Signal time window is surrounded by the background time window. The GRB trigger is the trigger time fired by the detector on the earth.

We can observe GRB almost every day. However, there is a situation that several GRBs occur on the same day. Figure 7.6 demonstrates a time overlap between two GRBs. For two GRBs with overlapping search time windows, we only kept one of them. Table 7.3 lists the number of remaining GRBs after removing those with overlapping search time.

Except for the overlapped GRBs, there are still many GRBs at Daya Bay not recorded

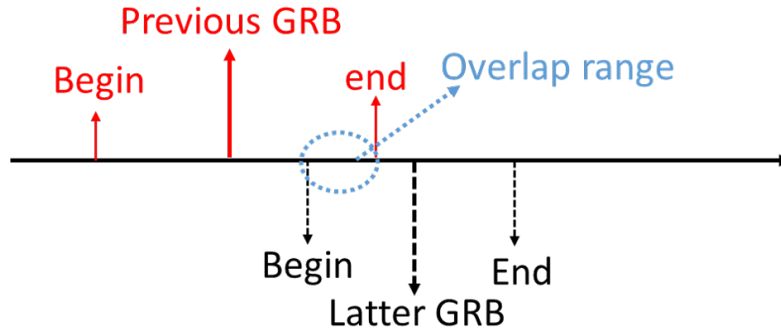


Figure 7.6 Definition of overlapping time between two GRBs.

in the data files due to various reasons. Table 7.3 lists the final number of GRBs used in the analysis.

Table 7.3 The number of GRBs under three time windows. “Initial” represents the initial number of GRBs. “Removed overlap” represents the remaining GRBs after removing the overlap search time window. “Observed by DYB” represents the final number of GRBs used in the analysis at Daya Bay. “ $\pm T_{\text{Dyna}}$ ” represents the dynamic time window.

GRBs	Initial	Removed Overlap	Observed by DYB
± 500 s	2225	2203	1720
± 1000 s	2225	2188	1734
$\pm T_{\text{Dyna}}$ s	1686	1682	1329

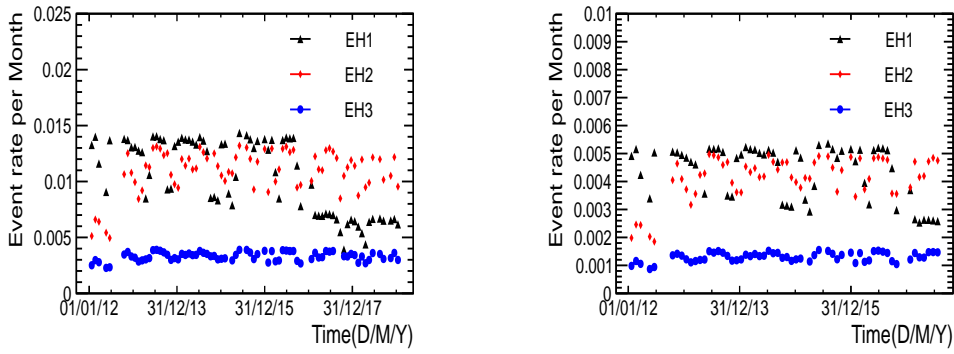
7.1.4 Background estimation

This section introduces the background estimation for the GRB analysis under two energy assumptions. Because the GRBs occur almost uniformly along the time axis during the Daya Bay operation, we did not adopt the GW analysis approach, which is correlated with each GW ± 5 days to calculate the background numbers. The event rate per month, as shown in Fig. 7.7 during the whole operation time, is relatively stable, only with little fluctuation.

The total background events N_{BKG} divided by the total live-time T_L , which has subtracted the search time windows, to obtain the background event rate. The average background rate is expressed as follows,

$$r_B = \frac{N_{\text{BKG}}}{T_L}. \quad (7-4)$$

Table 7.4 lists the average background event rates under the Fermi-Dirac spectrum



(a) Event rate per month for the nGd data sample in the three experimental halls. (b) Event rate per month for the nH data sample in the three experimental halls.

Figure 7.7 Event rate for the data sample in the three experimental halls. In different experiment periods, Daya Bay has different numbers of ADs, which result in the event rate fluctuation of each experimental hall.

assumption, while Table F.1 in Appendix gives those for the monochromatic spectra, respectively. The live-time used in the calculation removed the search time ± 1000 s of all GRBs, which is the most extended search time window of three search time windows. All dynamic time windows of the analyzed GRBs at Daya Bay are less than 1000 s. Then we calculated the expected background numbers when these GRBs occurred.

Table 7.4 Average background event rates during the Daya Bay live-time assuming the Fermi-Dirac spectrum. The live-time has removed the search time for all GRBs-related ± 1000 s, which is the most extended of the three time windows. (Low-energy: $E_p < 10$ MeV, High-energy: $E_p > 10$ MeV)

		Low energy (Rate: per second)		High energy (Rate: per second)	
		nGd ($\times 10^{-3}$)	nH ($\times 10^{-3}$)	nGd ($\times 10^{-5}$)	nH ($\times 10^{-5}$)
EH1	AD1	6.20 ± 0.01	2.28 ± 0.01	6.46 ± 0.07	8.19 ± 0.07
	AD2	6.22 ± 0.01	2.24 ± 0.01	6.44 ± 0.06	8.17 ± 0.07
EH2	AD1	5.72 ± 0.01	2.10 ± 0.01	4.04 ± 0.05	5.58 ± 0.06
	AD2	5.64 ± 0.01	2.06 ± 0.01	3.98 ± 0.07	5.51 ± 0.06
EH3	AD1	0.84 ± 0.01	0.33 ± 0.01	0.43 ± 0.02	0.63 ± 0.02
	AD2	0.84 ± 0.01	0.32 ± 0.01	0.43 ± 0.02	0.60 ± 0.02
	AD3	0.84 ± 0.01	0.32 ± 0.01	0.43 ± 0.02	0.61 ± 0.02
	AD4	0.84 ± 0.01	0.32 ± 0.01	0.47 ± 0.02	0.61 ± 0.02

In the end, the expected background events, N_B , can be calculated as follows,

$$N_B = r_B \times T_w \times O_{GRB}, \quad (7-5)$$

where r_B is the averaged background rate, T_w is the search time window, O_{GRB} is the number of observed GRBs at Daya Bay in Table 7.3. We adopted an average time window of 536 s to calculate the expected background events for the dynamic time window.

7.1.5 IBD candidates

After the expected background numbers estimation, the search for neutrino events is given in this section under two neutrino energy spectra assumed. For the monochromatic spectra, Figure 7.8 shows the distribution of IBD candidates under three time windows. The detailed results of ± 500 s, ± 1000 s, and T_{Dyna} are listed in Appendix Table F.2, F.3 and F.4, respectively.

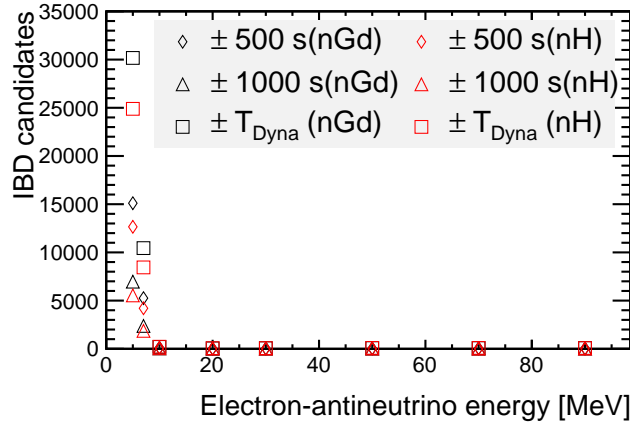
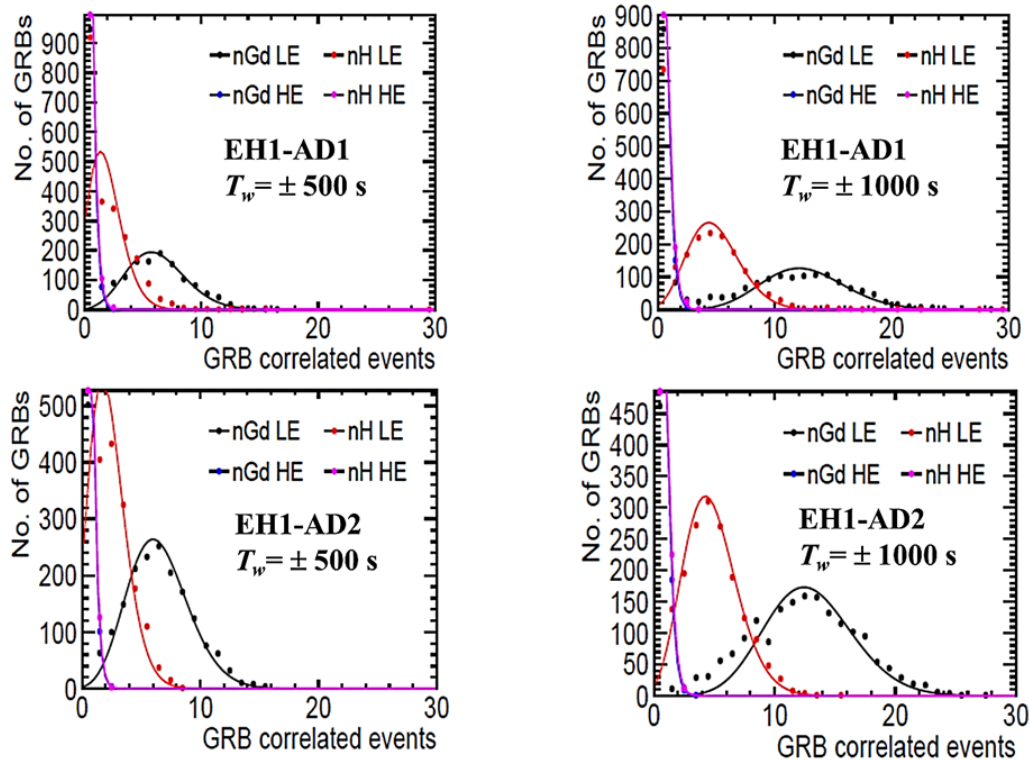


Figure 7.8 Distribution of total IBD candidates of all GRBs assuming the monochromatic spectra.

Table 7.5 lists the search results of GRB-correlated IBD candidates under three time windows for the Fermi-Dirac spectrum. The distributions of GRB-correlated IBD candidates within ± 500 s and ± 1000 s search time window are shown in Fig. 7.9, Fig. 7.10, and Fig. 7.11. We fitted the IBD candidates with a Poisson distribution. The fitting values in Table 7.6 and 7.7 show that the results of IBD candidates are consistent with the background level in Table 7.4. The signals did not significantly exceed the background level from the two fixed time windows' fitting results. Finally, the upper limits of GRB-correlated neutrino fluence are derived.

Table 7.5 The total IBD candidates correlated with GRBs are shown within three search time windows assuming the Fermi-Dirac spectrum (LE: $E_p < 10$ MeV, HE: $E_p > 10$ MeV).

Time window	E_ν	Data	EH1		EH2		EH3			
			AD1	AD2	AD1	AD2	AD1	AD2	AD3	AD4
± 500 s	LE	nGd	6986	10282	9616	8686	1408	1396	1359	1281
		nH	2442	3839	3501	3182	608	541	548	486
	HE	nGd	66	109	84	72	9	7	11	7
		nH	72	130	80	80	6	11	12	6
± 1000 s	LE	nGd	14008	20543	19003	17552	2778	2773	2752	2579
		nH	4901	7522	6960	6375	1123	1073	1063	924
	HE	nGd	141	206	160	131	17	11	25	11
		nH	164	249	169	158	19	19	17	14
$\pm T_{\text{Dyna}}$	LE	nGd	3223	4679	4402	3931	680	652	639	582
		nH	1007	1670	1615	1421	242	230	225	217
	HE	nGd	28	48	22	29	4	3	4	3
		nH	36	62	42	41	6	8	5	2


 Figure 7.9 Distributions of the number of GRBs correlated IBD candidates within the ± 500 s and ± 1000 s time window in EH1. The distribution of IBD candidates is fitted with a Poisson distribution.

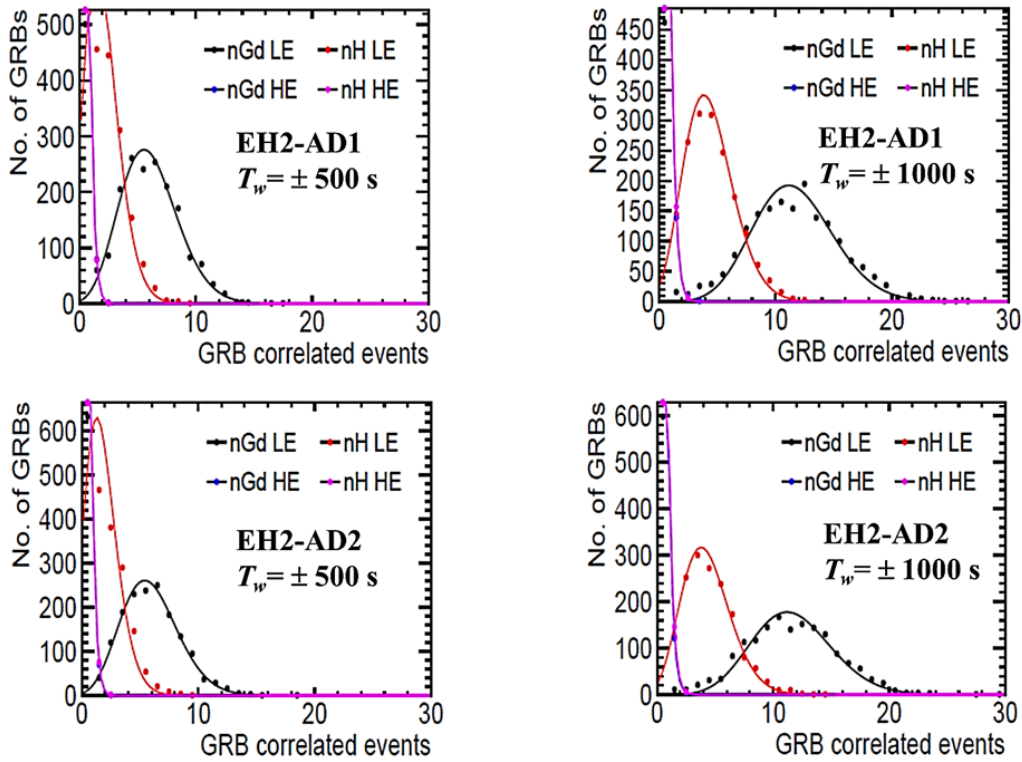


Figure 7.10 Distributions of the number of GRBs correlated IBD candidates within the ± 500 s and ± 1000 s time window in EH2. The distribution of IBD candidates is fitted with a Poisson distribution.

Table 7.6 Fitting values of the distribution of GRB-correlated IBD candidates using a Poisson distribution under a time window of ± 500 s. (Low-energy: $E_p < 10$ MeV, High-energy: $E_p > 10$ MeV)

$T_W = \pm 500$ s		Low energy		High energy	
		nGd	nH	nGd	nH
EH1	AD1	6.23 ± 0.09	1.91 ± 0.09	0.055 ± 0.006	0.078 ± 0.007
	AD2	6.51 ± 0.08	2.26 ± 0.05	0.073 ± 0.007	0.084 ± 0.007
EH2	AD1	6.06 ± 0.06	2.04 ± 0.05	0.057 ± 0.006	0.054 ± 0.006
	AD2	5.92 ± 0.07	1.82 ± 0.05	0.048 ± 0.005	0.054 ± 0.006
EH3	AD1	0.86 ± 0.03	0.39 ± 0.02	0.006 ± 0.002	0.004 ± 0.002
	AD2	0.84 ± 0.04	0.36 ± 0.02	0.005 ± 0.002	0.008 ± 0.002
	AD3	0.82 ± 0.04	0.36 ± 0.02	0.008 ± 0.002	0.008 ± 0.002
	AD4	0.82 ± 0.04	0.36 ± 0.02	0.008 ± 0.002	0.008 ± 0.002

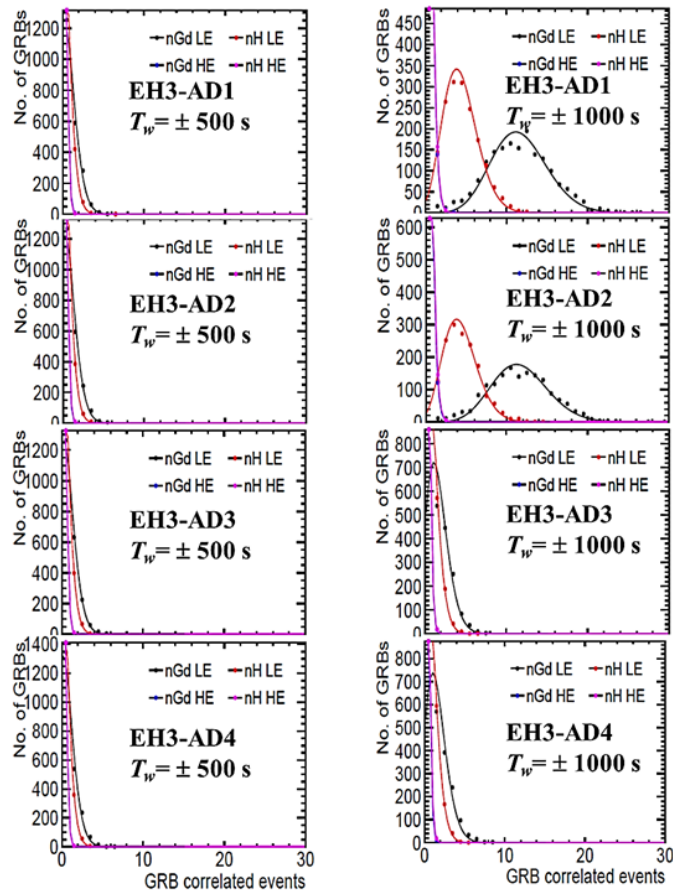


Figure 7.11 Distributions of the number of GRBs correlated IBD candidates within the ± 500 s and ± 1000 s time window in EH3. The distribution of IBD candidates is fitted with a Poisson distribution.

Table 7.7 Fitting values of the distribution of GRB-correlated IBD candidates using a Poisson distribution under a time window of ± 1000 s. (Low-energy: $E_p < 10$ MeV, High-energy: $E_p > 10$ MeV)

		Low energy		High energy	
		nGd	nH	nGd	nH
$T_W = \pm 1000$ s	EH1 AD1	12.58 ± 0.15	4.88 ± 0.08	0.12 ± 0.01	0.15 ± 0.01
	EH1 AD2	12.94 ± 0.12	4.77 ± 0.06	0.14 ± 0.01	0.17 ± 0.01
EH2	AD1	11.65 ± 0.10	4.37 ± 0.06	0.10 ± 0.01	0.10 ± 0.01
	AD2	11.71 ± 0.11	4.31 ± 0.06	0.09 ± 0.01	0.11 ± 0.01
EH3	AD1	1.62 ± 0.04	0.70 ± 0.02	0.012 ± 0.003	0.013 ± 0.003
	AD2	1.57 ± 0.04	0.75 ± 0.02	0.013 ± 0.003	0.013 ± 0.003
	AD3	1.59 ± 0.04	0.66 ± 0.02	0.017 ± 0.003	0.012 ± 0.003
	AD4	1.45 ± 0.05	0.58 ± 0.02	0.008 ± 0.003	0.010 ± 0.003

7.2 Results of $\bar{\nu}_e$ searches

This section focuses on the upper limits of the GRB neutrino fluence under two energy spectra assumed. The upper limits were calculated using the method, which is the same as the GW analysis. After obtaining the total neutrino fluence of all GRBs, the average fluence per GRB, $F_{\bar{\nu}_e}$, is as follows,

$$F_{\bar{\nu}_e} = \frac{F_{total}}{O_{GRB}}, \quad (7-6)$$

where F_{total} is the total neutrino fluence of all GRBs, and O_{GRB} is the number of observed GRBs at Daya Bay. The numbers of observed GRBs are 1720, 1734, and 1329 respectively, for three different time windows. The neutrino fluence $F_{\bar{\nu}_e}$ listed in Table 7.8 are the upper limits per GRB at Daya Bay. Figure 7.12 also shows the upper limits with the assumed monochromatic spectra.

Table 7.8 Upper limits of fluence at 90% C.L. for three search time windows assuming the monochromatic spectra and the Fermi-Dirac spectrum. The number of $\bar{\nu}_e$ candidates associated with the GRB events are averaged. The background events are also averaged.

$F_D \bar{\nu}_e (\times 10^7 \text{ cm}^{-2})$	Monochromatic Spectra								Fermi-Dirac (1.8, 100)	
	E_ν (MeV)	5	7	10	20	30	50	70		90
± 500 s		110.5	29.1	10.8	1.22	0.70	0.25	0.18	0.10	4.30
± 1000 s		50.7	20.8	3.51	0.81	0.48	0.27	0.14	0.08	2.08
$\pm T_{\text{Dyna}}$ s		2031	308.5	10.0	2.03	0.83	0.37	0.15	0.13	10.8

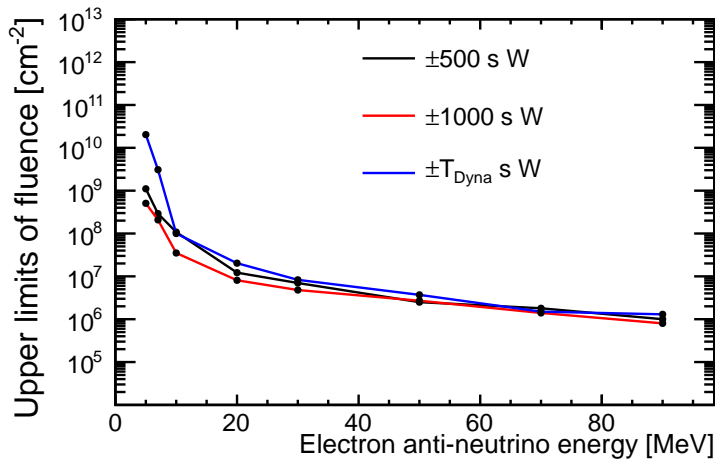


Figure 7.12 Fluence upper limits on $\bar{\nu}_e$ from GRBs as a function of neutrino energy within three search time windows.

7.3 Chapter summary

In this chapter, we have studied the GRB analysis process. There are a total of 2225 GRBs during the operation of the Daya Bay experiment from December 2011 to March 2019. It includes 212 GRBs recorded with redshift and 1686 GRBs recorded with a burst duration. Three time windows were selected, namely ± 500 s, ± 1000 s, and a dynamic window determined by the GRB redshift and burst duration. Here, we removed the GRBs that coincided in a search time window. Finally, we observed that the numbers of GRBs recorded and analyzed at Daya Bay for three search time windows were 1720, 1734, and 1329.

The background event rates were averaged from December 2011 to March 2019 scaled to the expected background during GRBs occurrence. We also searched for the IBD candidates within the GRB-related time windows. A Poisson distribution was adopted to fit the GRB-related IBD candidates in an AD at Daya Bay. The fitting results showed that the IBD candidates were consistent with the expected background events. We obtained the upper limits at a 90% confidence level under three search time windows and two energy spectrum hypotheses. We found that the upper limits at Daya Bay were comparable with the other published neutrino experiments' results.

Chapter 8 Conclusion

The astrophysical point sources are the distant objects that produce copious neutrinos, which are always accompanied by violent astronomical phenomena, such as GWs and GRBs. The joint observation of astrophysical phenomena will provide the key to know about the mechanism of such phenomena and the universe. In this thesis, we searched for the $\bar{\nu}_e$ signal candidates associated with GWs and GRBs in the Daya Bay.

For the GWs analysis or the GRBs analysis, the search for $\bar{\nu}_e$ energy is from 1.8 MeV to 100 MeV. When the neutrino energy exceeds tens of MeV, the kinetic of neutron generated by IBD reaction can not be ignored, which could not be described by the simple formula, $E_p = E_\nu - 0.78$ MeV. We simulated several discrete neutrino energies in the Daya Bay detector and got a more suitable relationship between the neutrino energy and mean reconstructed prompt energy, $E_p = A \times E_\nu^2 + B \times E_\nu + C$, with $A = -0.001$ MeV⁻¹, $B = 1.01$, $C = -0.73$ MeV. Then, we constructed the calculation of the neutrino fluence under two energy spectra, namely monochromatic spectra and the Fermi-Dirac spectrum.

When we studied neutrino (tens MeV) at Daya Bay, the first problem encountered was the IBD reaction cross-section. The Daya Bay neutrino experiment is dedicated to investigating the reactor neutrinos, which is mostly below 12 MeV. The Vogel and Beacom's IBD cross-section adopted at Daya Bay is appropriate for tens MeV in the detector simulation. To solve the problem, we adopted the IBD cross-section formula described by A. Strumia et al. The IBD cross-section formula extends the applicable neutrino energy up to ~ 200 MeV, which can cover the energy region in our study.

The physical properties of neutrons, in particular, the flight distance and flight time before captured by Gd or H, were essential in the study of the detection efficiency. The simulation package NuWa used in the Daya Bay is based on Geant Version 9.02. The Geant4 neutron simulation has updated many generations until now (the latest is Geant Version 10.06), especially in the neutron capture and moderation processes. We compared the difference caused by the neutron data files adopted in Geant4 in Version 9.6 and Version 10.3, and we found that the difference is insignificant due to the improvement of the neutron simulation in Geant4.

When we simulate the high-energy neutrinos, we found that the physical process of inelastic scattering (n, α) is increasing with the neutron kinetic energy increases.

When the neutrino energy $E_\nu = 90$ MeV, the contribution is about 2%. In the end, we discussed the detector efficiency under different energy spectra hypotheses using GdLS+LS+Acrylic as the target volume at Daya Bay.

The GW event observed by the LIGO experiment on September 14, 2015, confirmed the correctness of the general relativity. As messengers, neutrinos interact weakly with the matter and bring out the most primitive information from the sources. The astrophysicists expect to use neutrinos to know more about the mechanism of GWs generated by BH mergers or NS mergers. The complete GW events by now have been analyzed, namely, GW150914, GW151012, GW151226, GW170104, GW170608, GW170814, and GW170817. Two energy spectra were assumed due to the absence of the emitted neutrino energy spectrum information, namely the monochromatic spectra and the Fermi-Dirac spectrum. A total of three time windows, ± 10 s, ± 500 s, and ± 1000 s respectively, were adopted to search for the $\bar{\nu}_e$ associated with GW events. However, the signal candidates were consistent with the expected background levels. The correlation between neutrinos and the GWs was not found.

Finally, the neutrino fluence with a 90% confidence level was given. According to the characteristics of Daya Bay's unique spatial separation of multiple ADs, an approach of combining multiple ADs data was adopted to calculate the upper limits. When assuming the monochromatic spectra, the upper limits of $\bar{\nu}_e$ were given within three time windows, namely $(1.12 - 2.28) \times 10^{11} \text{ cm}^{-2}$ at 5 MeV to $1.0 \times 10^8 \text{ cm}^{-2}$ at 100 MeV. For a Fermi-Dirac spectrum, the upper limit of $\bar{\nu}_e$ at (1.8 MeV, 100 MeV) was $(4.2 - 5.5) \times 10^9 \text{ cm}^{-2}$ within three time windows. The upper limits of $\bar{\nu}_e$ luminosity were given and compared with the results published by other neutrino experiments assuming the Fermi-Dirac spectrum. We compared the upper limits of several major neutrino experiments at the order of tens MeV neutrinos. The neutrino fluence given by the Super-K (50-kiloton heavy water) was lower than other neutrino experiments due to its large target mass. Compared with the kiloton-scale KamLAND (5.98×10^{31}) and Borexino (4.79×10^{31}) neutrino experiments, the target mass of Daya Bay (2.52×10^{31}) is only one-third of them. However, the upper limits of neutrino fluence from the three experiments were comparable. This result depends on two reasons. One is the distribution of multiple ADs at Daya Bay. Although one single AD target mass is small, eight ADs were combined to reduce the impact from a single AD and improve the experimental sensitivity. Another reason is that we split the raw data into two parts, low-energy and high-energy, respectively. The

10 MeV selection criterion suppressed a large amount of neutrino background from the reactor. The upper limits of MeV-scale neutrino fluence associated with GWs observed at the Daya Bay experiment are not significant, consistent with the understanding of the BH-BH and NS-BS mergers physics. We hope that the upper limit of neutrino fluence at Daya Bay could constrain the theoretical neutrino models by combining other neutrino experiments' results.

GRBs are an active area of research since the discovery in 1968. GRBs are the most violent astronomical phenomenon in the universe, releasing energy up to $\sim 10^{52}$ erg. Searching for neutrinos generated by GRBs could provide more clear physical pictures of the inside source. Furthermore, the absolute mass of neutrino could be derived from the time difference of arriving in the detector between the γ -rays and neutrinos. We searched for a total of 2225 GRB events from December 2011 to March 2019. Besides the search time windows of ± 500 s and ± 1000 s mentioned by the previous GW analysis, a dynamic time window was proposed and determined by the duration T_{90} and the redshift Z of each GRB.

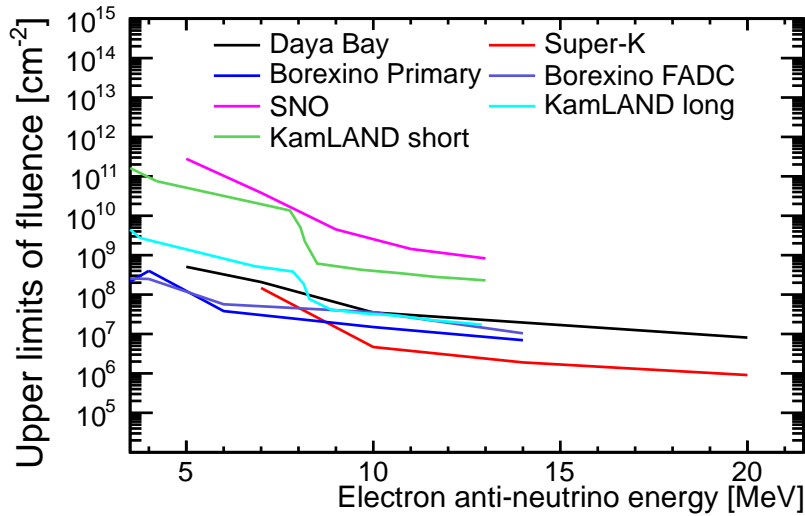


Figure 8.1 Fluence upper limits on $\bar{\nu}_e$ ($E_{\bar{\nu}_e} < 20$ MeV) from a GRB as a function of neutrino energy. The neutrino fluence of several neutrino experiments is compared with each other. Borexino Primary and FADC represent two semi-independent DAQ systems in the Borexino neutrino experiment. KamLAND long and short represents the long GRBs and short GRBs, respectively. The neutrino fluence of Daya Bay is the result of a ± 1000 s search time window.

The search results showed that the neutrino signal candidates did not significantly exceed the average background levels. Finally, the upper limits were given at a 90% con-

fidence level. The upper limits of the $\bar{\nu}_e$ fluence were from $2.03 \times 10^{10} \text{ cm}^{-2}$ to $0.08 \times 10^7 \text{ cm}^{-2}$ with the assumption of the monochromatic spectra, while the upper limits were $(2.08 - 10.8) \times 10^7 \text{ cm}^{-2}$ with the assumption of a Fermi-Dirac spectrum. The neutrino fluence has been estimated under the models, namely the GRB fireball model and the cosmic string model. From the values of the neutrino fluence under two different energy spectra assumptions, our results are more inclined to the GRB fireball model, which is generally accepted internationally. As shown in Fig. 8.1, we listed the upper limits of neutrino fluence given by several neutrino experiments, such as Super-K, SNO, Borexino, KamLAND, under the monochromatic spectra. It is observed that the neutrino fluence of Daya Bay is comparable with other neutrino experiments. Furthermore, we give the latest upper limits of MeV-scale neutrino fluence in the world.

The Daya Bay experiment is scheduled to operate until the end of 2020. With the accumulation of experimental data at Daya Bay and the GW events published by LIGO, the physicists may observe such events as SN1987A, if lucky. Also, large-scale neutrino experiments are building in the world, such as JUNO^[132], Jinping underground neutrino experiment^[133], and Hyper-K^[134], etc. Those will provide an excellent opportunity to find neutrinos from the universe. The joint observation of GWs, GRBs, and neutrinos will open a new world of multi-messenger astrophysics.

Bibliography

- [1] Chadwick J. The intensity distribution in the magnetic spectrum of beta particles from radium (b+ c)[J]. Verh. Phys. Gesell., 1914, 16: 383-391.
- [2] Brown L M. The idea of the neutrino[J]. Physics Today, 1978, 31(9): 23.
- [3] Cowan C L, Reines F, Harrison F, et al. Detection of the free neutrino: a confirmation[J]. Science, 1956, 124(3212): 103-104.
- [4] Pontecorvo B. Neutrino experiments and the problem of conservation of leptonic charge[J]. Sov. Phys. JETP, 1968, 26(984-988): 165.
- [5] Danby G, Gaillard J M, Goulianos K, et al. Observation of high-energy neutrino reactions and the existence of two kinds of neutrinos[J]. Physical Review Letters, 1962, 9(1): 36.
- [6] Hirata K, Kajita T, Koshiba M, et al. Observation of a neutrino burst from the supernova sn1987a[J]. Physical Review Letters, 1987, 58(14): 1490.
- [7] Hirata K, Kajita T, Koshiba M, et al. Observation in the kamiokande-ii detector of the neutrino burst from supernova sn1987a[J]. Physical Review D, 1988, 38(2): 448.
- [8] Bionta R, Blewitt G, Bratton C, et al. Observation of a neutrino burst in coincidence with supernova 1987a in the large magellanic cloud[M]// Neutrinos And Other Matters: Selected Works of Frederick Reines. World Scientific, 1991: 340-342.
- [9] Bratton C, Casper D, Ciocio A, et al. Angular distribution of events from sn1987a[J]. Physical Review D, 1988, 37(12): 3361.
- [10] Alekseev E, Krivosheina I, Volchenko V, et al. Possible detection of a neutrino signal on 23 february 1987 at the baksan underground scintillation telescope of the institute of nuclear research[J]. JETP Lett., 1987, 45: 739-744.
- [11] Alexeyev E, Alexeyeva L, Krivosheina I, et al. Detection of the neutrino signal from sn 1987a in the lmc using the inr baksan underground scintillation telescope[J]. Physics Letters B, 1988, 205(2-3): 209-214.
- [12] Kodama K, Ushida N, Andreopoulos C, et al. Observation of tau neutrino interactions[J]. Physics Letters B, 2001, 504(3): 218-224.
- [13] MissMJ, Cush. [EB/OL]. https://en.wikipedia.org/wiki/Standard_Model.
- [14] Decamp D, Deschizeaux B, Lees J P, et al. A precise determination of the number of families with light neutrinos and of the z boson partial widths[J]. Physics Letters B, 1990, 235(3-4): 399-411.
- [15] Spiering C. Towards High-Energy Neutrino Astronomy. A Historical Review[J/OL]. Eur. Phys. J. H, 2012, 37: 515-565. DOI: 10.1140/epjh/e2012-30014-2.
- [16] Araki T, et al. Experimental investigation of geologically produced antineutrinos with KamLAND[J/OL]. Nature, 2005, 436: 499-503. DOI: 10.1038/nature03980.

Bibliography

- [17] Bellini G, et al. Observation of Geo-Neutrinos[J/OL]. *Phys. Lett. B*, 2010, 687: 299-304. DOI: 10.1016/j.physletb.2010.03.051.
- [18] Berezhinskii V S, Zatsepin G T. Cosmic neutrinos of superhigh energy.[J]. *Yadern. Fiz.* 11: 200-5(1970).
- [19] Schutz B F. Gravitational wave astronomy[J]. *Classical and Quantum Gravity*, 1999, 16(12A): A131.
- [20] Einstein A. Approximative integration of the field equations of gravitation[J]. *Sitzungsber. Preuss. Akad. Wiss. Berlin (Math. Phys.)*, 1916, 1916: 688-696.
- [21] Einstein A. Über gravitationswellen[J]. *Sitzungsber. Preuss. Akad. Wiss. Berlin (Math. Phys.)*, 1918, 1918: 154-167.
- [22] [EB/OL]. <https://www.ligo.caltech.edu/images?page=2>.
- [23] Taylor J, Fowler L, McCulloch P. Measurements of general relativistic effects in the binary pulsar PSR 1913+16[J/OL]. *Nature*, 1979, 277: 437-440. DOI: 10.1038/277437a0.
- [24] Weisberg J M, Taylor J H. Relativistic binary pulsar b1913+ 16: Thirty years of observations and analysis[J]. *arXiv preprint astro-ph/0407149*, 2004.
- [25] Weber J. Evidence for discovery of gravitational radiation[J]. *Physical Review Letters*, 1969, 22(24): 1320.
- [26] Tyson J A, Giffard R. Gravitational-wave astronomy[J]. *Annual review of astronomy and astrophysics*, 1978, 16(1): 521-554.
- [27] Astone P, Baggio L, Bassan M, et al. Igec2: A 17-month search for gravitational wave bursts in 2005–2007[J]. *Physical Review D*, 2010, 82(2): 022003.
- [28] Harry G M, Collaboration L S, et al. Advanced ligo: the next generation of gravitational wave detectors[J]. *Classical and Quantum Gravity*, 2010, 27(8): 084006.
- [29] Krolak A, Patil M. The first detection of gravitational waves[J/OL]. *Universe*, 2017, 3: 59. DOI: 10.3390/universe3030059.
- [30] Abbott B P, Abbott R, Abbott T, et al. Observation of gravitational waves from a binary black hole merger[J]. *Physical review letters*, 2016, 116(6): 061102.
- [31] Nielsen A B, Capano C D, Birnholtz O, et al. Parameter estimation and statistical significance of echoes following black hole signals in the first advanced ligo observing run[J]. *Physical Review D*, 2019, 99(10): 104012.
- [32] Abbott B P, Abbott R, Abbott T, et al. Gw151226: observation of gravitational waves from a 22-solar-mass binary black hole coalescence[J]. *Physical review letters*, 2016, 116(24): 241103.
- [33] Scientific L, Abbott B, Abbott R, et al. Gw170104: observation of a 50-solar-mass binary black hole coalescence at redshift 0.2[J]. *Physical Review Letters*, 2017, 118(22): 221101.
- [34] Abbott B P, Abbott R, Abbott T, et al. Gw170608: Observation of a 19 solar-mass binary black hole coalescence[J]. *The Astrophysical Journal Letters*, 2017, 851(2): L35.
- [35] Abbott B P, Abbott R, Abbott T, et al. Gw170814: a three-detector observation of gravitational waves from a binary black hole coalescence[J]. *Physical review letters*, 2017, 119(14): 141101.

- [36] Abbott B P, Abbott R, Abbott T, et al. Gw170817: observation of gravitational waves from a binary neutron star inspiral[J]. *Physical Review Letters*, 2017, 119(16): 161101.
- [37] Arnett W D, Rosner J L. Neutrino mass limits from sn1987a[J]. *Physical review letters*, 1987, 58(18): 1906.
- [38] Connaughton V, Burns E, Goldstein A, et al. Fermi gbm observations of ligo gravitational-wave event gw150914[J]. *The Astrophysical Journal Letters*, 2016, 826(1): L6.
- [39] McLaughlin G C, Surman R. Supernova neutrinos: The accretion disk scenario[J]. *Physical Review D*, 2007, 75(2): 023005.
- [40] Adrián-Martínez S, Albert A, André M, et al. High-energy neutrino follow-up search of gravitational wave event gw150914 with antares and iccube[J]. *Physical Review D*, 2016, 93(12): 122010.
- [41] Gando A, Gando Y, Hachiya T, et al. A search for electron antineutrinos associated with gravitational-wave events gw150914 and gw151226 using kamland[J]. *The Astrophysical Journal Letters*, 2016, 829(2): L34.
- [42] Abe K, Haga K, Hayato Y, et al. Search for neutrinos in super-kamiokande associated with gravitational-wave events gw150914 and gw151226[J]. *The Astrophysical Journal Letters*, 2016, 830(1): L11.
- [43] Abe K, Bronner C, Hayato Y, et al. Search for neutrinos in super-kamiokande associated with the gw170817 neutron-star merger[J]. *The Astrophysical Journal Letters*, 2018, 857(1): L4.
- [44] Agostini M, Altenmuller K, Appel S, et al. A search for low-energy neutrinos correlated with gravitational wave events gw150914, gw151226 and gw170104 with the borexino detector[J]. arXiv preprint arXiv:1706.10176, 2017.
- [45] Kulkarni S, Djorgovski S, Odewahn S C, et al. The afterglow, redshift and extreme energetics of the γ -ray burst of 23 january 1999[J]. *Nature*, 1999, 398(6726): 389-394.
- [46] [EB/OL]. <https://imagine.gsfc.nasa.gov/news/10sep08.html>.
- [47] Klebesadel R W, Strong I B, Olson R A. Observations of gamma-ray bursts of cosmic origin[J]. *The Astrophysical Journal*, 1973, 182: L85.
- [48] Piran T. Gamma-ray bursts and the fireball model[J]. *Physics Reports*, 1999, 314(6): 575-667.
- [49] [EB/OL]. <https://gammaray.msfc.nasa.gov/batse/grb/skymap/>.
- [50] Robert S. Mallozzi. The durations of the 4b catalog gamma-ray bursts[EB/OL]. <https://gammaray.msfc.nasa.gov/batse/grb/duration/>.
- [51] Meszaros P. Gamma-ray bursts[J]. *Reports on Progress in Physics*, 2006, 69(8): 2259.
- [52] Band D, Matteson J, Ford L, et al. Batse observations of gamma-ray burst spectra. i-spectral diversity[J]. *The Astrophysical Journal*, 1993, 413: 281-292.
- [53] Dingus B, Catelli J. Egret detections of the highest energy emission from gamma-ray bursts[C]// 19th Texas Symposium on Relativistic Astrophysics and Cosmology. 1998.
- [54] Sakamoto T, Barthelmy S, Barbier L, et al. The first swift bat gamma-ray burst catalog[J]. *The Astrophysical Journal Supplement Series*, 2008, 175(1): 179.

Bibliography

- [55] Piran T. Towards understanding gamma-ray bursts[J]. arXiv preprint astro-ph/9507114, 1995.
- [56] Berezhinsky V, Hnatyk B, Vilenkin A. Gamma ray bursts from superconducting cosmic strings[J]. *Physical Review D*, 2001, 64(4): 043004.
- [57] Halzen F, Jaczko G. Signatures of γ ray bursts in neutrino telescopes[J]. *Physical Review D*, 1996, 54(4): 2779.
- [58] Paczynski B. Gamma-ray bursters at cosmological distances[J]. *The Astrophysical Journal*, 1986, 308: L43-L46.
- [59] Goodman J. Are gamma-ray bursts optically thick?[J]. *The Astrophysical Journal*, 1986, 308: L47-L50.
- [60] Katz J, Piran T. Persistent counterparts to gamma-ray bursts[J]. *The Astrophysical Journal*, 1997, 490(2): 772.
- [61] Piran T, Narayan R, et al. Spectra and light curves of gamma-ray burst afterglows[J]. *The Astrophysical Journal Letters*, 1998, 497(1): L17.
- [62] Waxman E. High energy neutrinos from gamma-ray bursts[J]. *Nuclear Physics B-Proceedings Supplements*, 2001, 91(1-3): 494-500.
- [63] De Paolis F, Ingrosso G, Orlando D, et al. High energy neutrinos from grbs[J]. *Nuclear Physics B-Proceedings Supplements*, 2001, 100(1-3): 347-349.
- [64] Vietri M. The soft x-ray afterglow of gamma-ray bursts: A stringent test for the fireball model[J]. *The Astrophysical Journal Letters*, 1997, 478(1): L9.
- [65] Waxman E, Bahcall J. High energy neutrinos from cosmological gamma-ray burst fireballs[J]. *Physical Review Letters*, 1997, 78(12): 2292.
- [66] Kumar P. Gamma-ray burst energetics[J]. *The Astrophysical Journal Letters*, 1999, 523(2): L113.
- [67] Kumar P, Zhang B. The physics of gamma-ray bursts & relativistic jets[J]. *Physics Reports*, 2015, 561: 1-109.
- [68] Fukuda S, Fukuda Y, Ishitsuka M, et al. Search for neutrinos from gamma-ray bursts using super-kamiokande[J]. *The Astrophysical Journal*, 2002, 578(1): 317.
- [69] Vogel P, Beacom J F. Angular distribution of neutron inverse beta decay, $\nu e + p \rightarrow e^{++} n$ [J]. *Physical Review D*, 1999, 60(5): 053003.
- [70] Agostini M, Altenmüller K, Appel S, et al. Borexino's search for low-energy neutrino and antineutrino signals correlated with gamma-ray bursts[J]. *Astroparticle Physics*, 2017, 86: 11-17.
- [71] Aharmim B, Ahmed S, Anthony A, et al. A search for astrophysical burst signals at the sudbury neutrino observatory[J]. *Astroparticle Physics*, 2014, 55: 1-7.
- [72] Asakura K, Gando A, Gando Y, et al. Study of electron anti-neutrinos associated with gamma-ray bursts using kamland[J]. *The Astrophysical Journal*, 2015, 806(1): 87.
- [73] Vieregg A, Palladino K, Allison P, et al. The first limits on the ultra-high energy neutrino fluence from gamma-ray bursts[J]. *The Astrophysical Journal*, 2011, 736(1): 50.

- [74] Adrián-Martínez S, Samarai I A, Albert A, et al. First search for neutrinos in correlation with gamma-ray bursts with the antares neutrino telescope[J]. arXiv preprint arXiv:1302.6750, 2013.
- [75] Adrián-Martínez S, Albert A, Al Samarai I, et al. Search for muon neutrinos from gamma-ray bursts with the antares neutrino telescope using 2008 to 2011 data[J]. *Astronomy & Astrophysics*, 2013, 559: A9.
- [76] Cao J, Luk K B. An overview of the daya bay reactor neutrino experiment[J]. *Nuclear Physics B*, 2016, 908: 62-73.
- [77] An F, Bai J, Balantekin A, et al. Observation of electron-antineutrino disappearance at daya bay[J]. *Physical Review Letters*, 2012, 108(17): 171803.
- [78] An F, Balantekin A, Band H, et al. Search for a light sterile neutrino at daya bay[J]. *Physical review letters*, 2014, 113(14): 141802.
- [79] An F P, Balantekin A, Band H, et al. Improved search for a light sterile neutrino with the full configuration of the daya bay experiment[J]. *Physical review letters*, 2016, 117(15): 151802.
- [80] Adamson P, An F, Anghel I, et al. Limits on active to sterile neutrino oscillations from disappearance searches in the minos, daya bay, and bugey-3 experiments[J]. *Physical review letters*, 2016, 117(15): 151801.
- [81] An F P, Balantekin A, Band H, et al. Measurement of the reactor antineutrino flux and spectrum at daya bay[J]. *Physical review letters*, 2016, 116(6): 061801.
- [82] An F P, Balantekin A, Band H, et al. Improved measurement of the reactor antineutrino flux and spectrum at daya bay[J]. *Chinese Physics C*, 2017, 41(1): 013002.
- [83] An F, Balantekin A, Band H, et al. Evolution of the reactor antineutrino flux and spectrum at daya bay[J]. *Physical review letters*, 2017, 118(25): 251801.
- [84] An F, Balantekin A, Band H, et al. Seasonal variation of the underground cosmic muon flux observed at daya bay[J]. *Journal of Cosmology and Astroparticle Physics*, 2018, 2018(01): 001.
- [85] An F, Balantekin A, Band H, et al. The muon system of the daya bay reactor antineutrino experiment[J]. *Nuclear Instruments and Methods in Physics Research Section A: Accelerators, Spectrometers, Detectors and Associated Equipment*, 2015, 773: 8-20.
- [86] An F, An Q, Bai J, et al. A side-by-side comparison of daya bay antineutrino detectors[J]. *Nuclear Instruments and Methods in Physics Research Section A: Accelerators, Spectrometers, Detectors and Associated Equipment*, 2012, 685: 78-97.
- [87] Guo X. A precision measurement of the neutrino mixing angle θ_{13} using reactor antineutrinos at daya bay[R]. 2007.
- [88] An F, Bai J, Balantekin A, et al. The detector system of the daya bay reactor neutrino experiment[J]. *Nuclear Instruments and Methods in Physics Research Section A: Accelerators, Spectrometers, Detectors and Associated Equipment*, 2016, 811: 133-161.
- [89] Qian X, Peng J C. Physics with reactor neutrinos[J]. *Reports on Progress in Physics*, 2019, 82(3): 036201.
- [90] Ji-Lei X, Meng-Yun G, Chang-Gen Y, et al. Design and preliminary test results of daya bay rpc modules[J]. *Chinese Physics C*, 2011, 35(9): 844.

- [91] Ma L, Lebanowski L, Chen J, et al. The mass production and quality control of rpcs for the daya bay experiment[J]. Nuclear Instruments and Methods in Physics Research Section A: Accelerators, Spectrometers, Detectors and Associated Equipment, 2011, 659(1): 154-160.
- [92] Liu J, Cai B, Carr R, et al. Automated calibration system for a high-precision measurement of neutrino mixing angle θ_{13} with the daya bay antineutrino detectors[J]. Nuclear Instruments and Methods in Physics Research Section A: Accelerators, Spectrometers, Detectors and Associated Equipment, 2014, 750: 19-37.
- [93] An F, Balantekin A, Band H, et al. New measurement of θ_{13} via neutron capture on hydrogen at daya bay[J]. Physical Review D, 2016, 93(7): 072011.
- [94] An F P, Balantekin A, Band H, et al. Measurement of electron antineutrino oscillation based on 1230 days of operation of the daya bay experiment[J]. Physical Review D, 2017, 95(7): 072006.
- [95] Lindhard J, Nielsen V, Scharff M, et al. Integral equations governing radiation effects[J]. Mat. Fys. Medd. Dan. Vid. Selsk, 1963, 33(10): 1-42.
- [96] Birks J B. Scintillations from organic crystals: specific fluorescence and relative response to different radiations[J]. Proceedings of the Physical Society. Section A, 1951, 64(10): 874.
- [97] Craun R, Smith D. Analysis of response data for several organic scintillators[J/OL]. Nuclear Instruments and Methods, 1970, 80(2): 239 - 244. <http://www.sciencedirect.com/science/article/pii/0029554X70907688>. DOI: [https://doi.org/10.1016/0029-554X\(70\)90768-8](https://doi.org/10.1016/0029-554X(70)90768-8).
- [98] Caballero O, McLaughlin G, Surman R. Neutrino spectra from accretion disks: neutrino general relativistic effects and the consequences for nucleosynthesis[J]. The Astrophysical Journal, 2012, 745(2): 170.
- [99] Caballero O, Zielinski T, McLaughlin G, et al. Black hole spin influence on accretion disk neutrino detection[J]. Physical Review D, 2016, 93(12): 123015.
- [100] Llewellyn Smith C. Neutrino Reactions at Accelerator Energies[J/OL]. Phys. Rept., 1972, 3: 261-379. DOI: 10.1016/0370-1573(72)90010-5.
- [101] Strumia A, Vissani F. Precise quasielastic neutrino/nucleon cross-section[J]. Physics Letters B, 2003, 564(1-2): 42-54.
- [102] Allison J, Amako K, Apostolakis J, et al. Geant4 developments and applications[J]. IEEE Transactions on nuclear science, 2006, 53(1): 270-278.
- [103] Geant-web. Geant overview[EB/OL]. 2019[2019-12-06]. <http://geant4.web.cern.ch/>.
- [104] Geant4—a simulation toolkit[J]. Nuclear Instruments and Methods in Physics Research Section A: Accelerators, Spectrometers, Detectors and Associated Equipment, 2003, 506(3): 250 - 303.
- [105] An F, An Q, Bai J, et al. Improved measurement of electron antineutrino disappearance at daya bay[J]. Chinese Physics C, 2013, 37(1): 011001.
- [106] An F P, et al. Measurement of electron antineutrino oscillation based on 1230 days of operation of the Daya Bay experiment[J/OL]. Phys. Rev. D, 2017, 95(7): 072006. DOI: 10.1103/PhysRevD.95.072006.
- [107] An F, et al. New measurement of θ_{13} via neutron capture on hydrogen at Daya Bay[J/OL]. Phys.

- Rev. D, 2016, 93(7): 072011. DOI: 10.1103/PhysRevD.93.072011.
- [108] Jing-Yi Y, Zhe W, Shao-Min C. A precise calculation of delayed coincidence selection efficiency and accidental coincidence rate[J]. Chinese Physics C, 2015, 39(5): 056201.
- [109] Thomas J Langford C W, Karsten M. Heeger. Unblinded target masses at daya bay[EB/OL]. 2014[2014-05-22]. <http://dayabay.ihep.ac.cn/cgi-bin/DocDB/ShowDocument>.
- [110] Cowan G, Cranmer K, Gross E, et al. Asymptotic formulae for likelihood-based tests of new physics[J]. The European Physical Journal C, 2011, 71(2): 1554.
- [111] Feldman G J, Cousins R D. Unified approach to the classical statistical analysis of small signals[J]. Physical Review D, 1998, 57(7): 3873.
- [112] Baret B, Bartos I, Bouhou B, et al. Bounding the time delay between high-energy neutrinos and gravitational-wave transients from gamma-ray bursts[J]. Astroparticle Physics, 2011, 35(1): 1-7.
- [113] Wei H. Highlight on supernova early warning at daya bay[J]. Physics Procedia, 2015, 61: 802-806.
- [114] Grbweb[EB/OL]. https://icecube.wisc.edu/~grbweb_public/index.html.
- [115] The gamma-ray coordinates network[EB/OL]. <http://gcn.gsfc.nasa.gov/>.
- [116] Felde J. Near realtime searches for neutrinos from grbs with icecube[J]. PoS, 2015: 1089.
- [117] Paciesas W S, Meegan C A, von Kienlin A, et al. The fermi gbm gamma-ray burst catalog: The first two years[J]. The Astrophysical Journal Supplement Series, 2012, 199(1): 18.
- [118] Goldstein A, Burgess J M, Preece R D, et al. The fermi gbm gamma-ray burst spectral catalog: the first two years[J]. The Astrophysical Journal Supplement Series, 2012, 199(1): 19.
- [119] Aptekar R, Frederiks D, Golenetskii S, et al. Konus-w gamma-ray burst experiment for the ggs wind spacecraft[J]. Space Science Reviews, 1995, 71(1-4): 265-272.
- [120] Bautz M W, Miller E D, Sanders J S, et al. Suzaku observations of abell 1795: Cluster emission to r 200[J]. Publications of the Astronomical Society of Japan, 2009, 61(5): 1117-1133.
- [121] Gehrels N, Chincarini G, Giommi P, et al. The swift gamma-ray burst mission[J]. The Astrophysical Journal, 2004, 611(2): 1005.
- [122] Winkler C, Di Cocco G, Gehrels N, et al. The integral mission[J]. Astronomy & Astrophysics, 2003, 411(1): L1-L6.
- [123] Nakazato K, Sumiyoshi K, Suzuki H, et al. Supernova neutrino light curves and spectra for various progenitor stars: from core collapse to proto-neutron star cooling[J]. The Astrophysical Journal Supplement Series, 2013, 205(1): 2.
- [124] Totani T, Sato K, Dalhed H, et al. Future detection of supernova neutrino burst and explosion mechanism[J]. The Astrophysical Journal, 1998, 496(1): 216.
- [125] Kiuchi K, Sekiguchi Y, Kyutoku K, et al. Gravitational waves, neutrino emissions and effects of hyperons in binary neutron star mergers[J]. Classical and Quantum Gravity, 2012, 29(12): 124003.
- [126] Collaboration P, Ade P, Aghanim N, et al. Planck 2013 results. xvi. cosmological parameters[J].

- Astron. Astrophys, 2014, 571: A16.
- [127] Choubey S, King S. Gamma ray bursts as probes of neutrino mass, quantum gravity, and dark energy[J]. Physical Review D, 2003, 67(7): 073005.
- [128] Li H, Dai Z, Zhang X. Testing varying neutrino mass with short gamma ray bursts[J]. Physical Review D, 2005, 71(11): 113003.
- [129] Orii A. Search for neutrinos associated with gamma-ray bursts in super-kamiokande[D]. School of Science, The University of Tokyo, 2018.
- [130] Tegmark M, Strauss M A, Blanton M R, et al. Cosmological parameters from sdss and wmap[J]. Physical review D, 2004, 69(10): 103501.
- [131] Cosmology calculators[EB/OL]. <http://www.astro.ucla.edu/~wright/CosmoCalc.html>.
- [132] An F, An G, An Q, et al. Neutrino physics with JUNO[J/OL]. Journal of Physics G Nuclear Physics, 2016, 43(3): 030401. DOI: 10.1088/0954-3899/43/3/030401.
- [133] Beacom J F, Chen S, Cheng J, et al. Physics prospects of the jinping neutrino experiment[J]. Chinese physics C, 2017, 41(2): 023002.
- [134] Nakamura K. Hyper-Kamiokande — A Next Generation Water Cherenkov Detector[J/OL]. International Journal of Modern Physics A, 2003, 18(22): 4053-4063. DOI: 10.1142/S0217751X03017361.

Appendix A Geant4 9.6 physical list

```
#include "NeutronHPphysics.hh"
#include "NeutronHPMessenger.hh"
#include "G4ParticleDefinition.hh"
#include "G4ProcessManager.hh"
#include "G4ProcessTable.hh"
// Processes
#include "G4HadronElasticProcess.hh"
// #include "G4ParticleHPElasticData.hh"
#include "G4NeutronHPElasticData.hh"
// #include "G4ParticleHPThermalScatteringData.hh"
#include "G4NeutronHPThermalScatteringData.hh"
// #include "G4ParticleHPElastic.hh"
#include "G4NeutronHPElastic.hh"
// #include "G4ParticleHPThermalScattering.hh"
#include "G4NeutronHPThermalScattering.hh"
#include "G4NeutronHPInelasticProcess.hh"
// #include "G4ParticleHPInelasticData.hh"
#include "G4NeutronHPInelasticData.hh"
#include "G4NeutronHPInelasticData.hh"
// #include "G4ParticleHPInelastic.hh"
#include "G4NeutronHPInelastic.hh"
#include "G4HadronCaptureProcess.hh"
// #include "G4ParticleHPCaptureData.hh"
#include "G4NeutronHPCaptureData.hh"
// #include "G4ParticleHPCapture.hh"
#include "G4NeutronHPCapture.hh"
#include "G4HadronFissionProcess.hh"
// #include "G4ParticleHPFissionData.hh"
#include "G4NeutronHPFissionData.hh"
```

```
//#include "G4ParticleHPFission.hh"
#include "G4NeutronHPFission.hh"
#include "G4SystemOfUnits.hh"

NeutronHPphysics::NeutronHPphysics(const G4String& name)
: G4VPhysicsConstructor(name), fThermal(true), fNeutronMessenger(0)
{
    fNeutronMessenger = new NeutronHPMessenger(this);
}

NeutronHPphysics::~NeutronHPphysics()
{
    delete fNeutronMessenger;
}

void NeutronHPphysics::ConstructProcess()
{
    G4ParticleDefinition* neutron = G4Neutron::Neutron();
    G4ProcessManager* pManager = neutron->GetProcessManager();

    // delete all neutron processes if already registered
    //
    G4ProcessTable* processTable = G4ProcessTable::GetProcessTable();
    G4VProcess* process = 0;
    process = processTable->FindProcess("hadElastic", neutron);
    if (process) pManager->RemoveProcess(process);
    //
    process = processTable->FindProcess("neutronInelastic", neutron);
    if (process) pManager->RemoveProcess(process);
    //
    process = processTable->FindProcess("nCapture", neutron);
    if (process) pManager->RemoveProcess(process);
    //
}
```

```
process = processTable->FindProcess("nFission", neutron);
if (process) pManager->RemoveProcess(process);

// (re) create process: elastic
//
G4HadronElasticProcess* process1 = new G4HadronElasticProcess();
pManager->AddDiscreteProcess(process1);
//
// modella
// G4ParticleHPElastic* modella = new G4ParticleHPElastic();
G4NeutronHPElastic* modella = new G4NeutronHPElastic();
process1->RegisterMe(modella);
process1->AddDataSet(new G4NeutronHPElasticData());
//
// modellb
if (fThermal) {
    modella->SetMinEnergy(4*eV);
    G4NeutronHPThermalScattering* modellb =
        new G4NeutronHPThermalScattering();
    process1->RegisterMe(modellb);
    process1->AddDataSet(new G4NeutronHPThermalScatteringData());
}

// (re) create process: inelastic
//
G4NeutronInelasticProcess* process2 =
    new G4NeutronInelasticProcess();
pManager->AddDiscreteProcess(process2);
//
// cross section data set
G4NeutronHPInelasticData* dataSet2 = new G4NeutronHPInelasticData();
process2->AddDataSet(dataSet2);
//
```

```
// models
G4NeutronHPInelastic* model2 = new G4NeutronHPInelastic ();
process2 ->RegisterMe (model2);

// (re) create process: nCapture
//
G4HadronCaptureProcess* process3 = new G4HadronCaptureProcess ();
pManager->AddDiscreteProcess (process3);
//
// cross section data set
G4NeutronHPCaptureData* dataSet3 = new G4NeutronHPCaptureData ();
process3 ->AddDataSet (dataSet3);
//
// models
G4NeutronHPCapture* model3 = new G4NeutronHPCapture ();
process3 ->RegisterMe (model3);

// (re) create process: nFission
//
G4HadronFissionProcess* process4 = new G4HadronFissionProcess ();
pManager->AddDiscreteProcess (process4);
//
// cross section data set
G4NeutronHPFissionData* dataSet4 = new G4NeutronHPFissionData ();
process4 ->AddDataSet (dataSet4);
//
// models
G4NeutronHPFission* model4 = new G4NeutronHPFission ();
process4 ->RegisterMe (model4);
}
```

Appendix B Geant4 10.3 physical list

```
#include "NeutronHPphysics.hh"
#include "NeutronHPMessenger.hh"
#include "G4ParticleDefinition.hh"
#include "G4ProcessManager.hh"
#include "G4ProcessTable.hh"
// Processes
#include "G4HadronElasticProcess.hh"
#include "G4ParticleHPElasticData.hh"
#include "G4ParticleHPThermalScatteringData.hh"
#include "G4ParticleHPElastic.hh"
#include "G4ParticleHPThermalScattering.hh"
#include "G4NeutronInelasticProcess.hh"
#include "G4ParticleHPInelasticData.hh"
#include "G4ParticleHPInelastic.hh"
#include "G4HadronCaptureProcess.hh"
#include "G4ParticleHPCaptureData.hh"
#include "G4ParticleHPCapture.hh"
#include "G4HadronFissionProcess.hh"
#include "G4ParticleHPFissionData.hh"
#include "G4ParticleHPFission.hh"
#include "G4SystemOfUnits.hh"

NeutronHPphysics::NeutronHPphysics(const G4String& name)
:   G4VPhysicsConstructor(name), fThermal(true),
   fNeutronMessenger(0)
{
  fNeutronMessenger = new NeutronHPMessenger(this);
}
```

```

}

NeutronHPphysics::~NeutronHPphysics()
{
    delete fNeutronMessenger;
}

void NeutronHPphysics::ConstructProcess()
{
    G4ParticleDefinition* neutron = G4Neutron::Neutron();
    G4ProcessManager* pManager = neutron->GetProcessManager();
    // delete all neutron processes if already registered
    G4ProcessTable* processTable = G4ProcessTable::GetProcessTable();
    G4VProcess* process = 0;
    process = processTable->FindProcess("hadElastic", neutron);
    if (process) pManager->RemoveProcess(process);
    process = processTable->FindProcess("neutronInelastic", neutron);
    if (process) pManager->RemoveProcess(process);
    process = processTable->FindProcess("nCapture", neutron);
    if (process) pManager->RemoveProcess(process);
    process = processTable->FindProcess("nFission", neutron);
    if (process) pManager->RemoveProcess(process);
    // (re) create process: elastic
    G4HadronElasticProcess* process1 = new G4HadronElasticProcess();
    pManager->AddDiscreteProcess(process1);
    // modella
    G4ParticleHPElastic* modella = new G4ParticleHPElastic();
    process1->RegisterMe(modella);
    process1->AddDataSet(new G4ParticleHPElasticData());
    // modellb
    if (fThermal) {
        modella->SetMinEnergy(4*eV);
        G4ParticleHPThermalScattering* modellb =

```



```

        new G4ParticleHPThermalScattering ();
    process1 ->RegisterMe(model1b);
    process1 ->AddDataSet(new G4ParticleHPThermalScatteringData ());
}

// (re) create process: inelastic
G4NeutronInelasticProcess* process2 =
        new G4NeutronInelasticProcess ();
pManager->AddDiscreteProcess(process2);
// cross section data set
G4ParticleHPInelasticData* dataSet2 =
        new G4ParticleHPInelasticData ();
process2 ->AddDataSet(dataSet2);
// models
G4ParticleHPInelastic* model2 = new G4ParticleHPInelastic ();
process2 ->RegisterMe(model2);
// (re) create process: nCapture
G4HadronCaptureProcess* process3 = new G4HadronCaptureProcess ();
pManager->AddDiscreteProcess(process3);
// cross section data set
G4ParticleHPCaptureData* dataSet3 = new G4ParticleHPCaptureData ();
process3 ->AddDataSet(dataSet3);
// models
G4ParticleHPCapture* model3 = new G4ParticleHPCapture ();
process3 ->RegisterMe(model3);
// (re) create process: nFission
G4HadronFissionProcess* process4 = new G4HadronFissionProcess ();
pManager->AddDiscreteProcess(process4);
G4ParticleHPFissionData* dataSet4 = new G4ParticleHPFissionData ();
process4 ->AddDataSet(dataSet4);
G4ParticleHPFission* model4 = new G4ParticleHPFission ();
process4 ->RegisterMe(model4);}

```

Appendix C Muon veto efficiency and multiplicity cut efficiency

Table C.1 The detailed efficiencies of muon veto about all the GW events when AD muon energy is required to be higher than 100 MeV. The “Ave” represents the average muon veto efficiencies of GRB analysis from Dec. 2011 to Mar. 2019.

	Data	EH1-AD1	EH1-AD2	EH2-AD1	EH2-AD2	EH3-AD1	EH3-AD2	EH3-AD3	EH3-AD4	
		Muon veto efficiencies of GW analysis								
GW150914	nGd	79.92%	79.56%	83.67%	83.62%	98.26%	98.26%	98.25%	98.23%	
	nH	76.79%	76.45%	81.19%	81.14%	97.97%	97.97%	97.96%	97.94%	
GW151012	nGd	80.04%	79.59%	83.74%	83.69%	98.26%	98.27%	98.25%	98.23%	
	nH	76.92%	76.48%	81.26%	81.21%	97.97%	97.98%	97.96%	97.94%	
GW151226	nGd	80.30%	79.63%	83.77%	83.75%	98.27%	98.28%	98.26%	98.22%	
	nH	77.17%	76.52%	81.30%	81.27%	97.98%	98.00%	97.98%	97.94%	
GW170104	nGd	–	–	83.59%	83.53%	98.27%	98.27%	98.18%	98.28%	
	nH	–	–	81.14%	81.08%	97.99%	97.99%	97.89%	97.99%	
GW170608	nGd	–	79.42%	83.69%	83.51%	98.28%	98.27%	98.23%	98.28%	
	nH	–	76.47%	81.24%	81.38%	98.00%	97.99%	97.94%	97.99%	
GW170814	nGd	–	79.57%	83.86%	83.72%	98.29%	98.29%	98.27%	98.27%	
	nH	–	76.33%	81.22%	81.05%	98.56%	98.55%	98.52%	98.50%	
GW170817	nGd	–	79.56%	83.90%	83.74%	98.29%	98.29%	98.28%	98.27%	
	nH	–	76.46%	81.42%	81.26%	98.00%	98.00%	97.99%	97.99%	
		Muon veto efficiencies of GRB analysis								
Ave.	nGd	79.93%	79.53%	83.65%	83.54%	98.24%	98.22%	98.22%	98.24%	
	nH	76.81%	76.43%	81.18%	81.08%	97.95%	97.94%	97.93%	97.95%	

Table C.2 The detailed efficiencies of multiplicity cut about all the GW events when AD muon energy is required to be higher than 100 MeV. The “Ave” represents the average multiplicity cut efficiencies of GRB analysis from Dec. 2011 to Mar. 2019.

	Data	EH1-AD1	EH1-AD2	EH2-AD1	EH2-AD2	EH3-AD1	EH3-AD2	EH3-AD3	EH3-AD4
		Multiplicity cut efficiencies of GW analysis							
GW150914	nGd	97.73%	97.73%	97.85%	97.84%	97.88%	97.89%	97.87%	97.86%
	nH	98.47%	98.48%	98.50%	98.51%	98.53%	98.52%	98.51%	98.49%
GW151012	nGd	97.74%	97.78%	97.86%	97.84%	97.87%	97.89%	97.87%	97.85%
	nH	98.47%	98.48%	98.50%	98.52%	98.52%	98.51%	98.50%	98.49%
GW151226	nGd	97.75%	97.78%	97.86%	97.85%	97.88%	97.88%	97.88%	97.85%
	nH	98.48%	98.48%	98.51%	98.52%	98.52%	98.50%	98.51%	98.49%
GW170104	nGd	–	–	97.89%	97.85%	97.85%	97.88%	97.88%	97.86%
	nH	–	–	98.52%	98.51%	98.49%	98.50%	98.53%	98.47%
GW170608	nGd	–	97.79%	97.87%	97.86%	97.89%	97.88%	97.89%	97.87%
	nH	–	98.49%	98.50%	98.51%	98.53%	98.50%	98.51%	98.51%
GW170814	nGd	–	97.80%	97.87%	97.86%	97.89%	97.87%	97.88%	97.85%
	nH	–	98.48%	98.51%	98.51%	98.51%	98.50%	98.51%	98.49%
GW170817	nGd	–	97.80%	97.88%	97.86%	97.87%	97.88%	97.89%	97.85%
	nH	–	98.48%	98.51%	98.51%	98.51%	98.50%	98.51%	98.49%
		Multiplicity cut efficiencies of GRB analysis							
Ave.	nGd	97.73%	97.77%	97.84%	97.84%	97.85%	97.85%	97.83%	97.85%
	nH	98.48%	98.48%	98.50%	98.51%	98.51%	98.49%	98.49%	98.50%

Appendix D IBD candidates for all GWs

 Table D.5 IBD candidates in ± 10 s and ± 1000 s search time windows are shown assuming the monochromatic spectra.

GW	T_w [s]	E_ν [MeV]	EH1		EH2		EH1			
			AD1	AD2	AD1	AD2	AD1	AD2	AD3	AD4
GW150914	± 10	5 (nGd)	0	0	0	0	0	0	0	0
		5 (nH)	0	0	0	0	0	0	0	0
		7 (nGd)	0	0	0	0	0	0	0	0
		7 (nH)	0	0	0	0	0	0	0	0
		10 (nGd)	0	0	0	0	0	0	0	0
		10 (nH)	0	0	0	0	0	0	0	0
	± 1000	5 (nGd)	4	3	6	4	0	0	0	0
		5 (nH)	4	2	5	3	0	0	0	1
		7 (nGd)	3	2	0	2	0	0	0	0
		7 (nH)	3	0	1	1	0	0	0	0
		10 (nGd)	0	0	0	0	0	0	0	0
		10 (nH)	0	0	0	1	0	0	0	0
GW151012	± 10	5 MeV (nGd)	0	0	0	0	0	0	0	0
		5 MeV (nH)	0	0	0	0	0	0	0	0
		7 MeV (nGd)	0	0	0	0	0	0	0	0
		7 MeV (nH)	0	0	0	0	0	0	0	0
		10 MeV (nGd)	0	0	0	0	0	0	0	0
		10 MeV (nH)	0	0	0	0	0	0	0	0
	± 1000	5 MeV (nGd)	1	5	1	4	0	2	0	0
		5 MeV (nH)	4	3	2	5	1	0	0	0
		7 MeV (nGd)	1	2	1	2	0	0	0	0
		7 MeV (nH)	3	3	0	1	0	0	0	0
		10 MeV (nGd)	0	0	0	0	0	0	0	0
		10 MeV (nH)	0	0	0	0	0	0	0	0
GW151226	± 10	5 MeV (nGd)	0	0	0	0	0	0	0	0
		5 MeV (nH)	0	0	0	0	0	0	0	0
		7 MeV (nGd)	0	0	0	0	0	0	0	0
		7 MeV (nH)	0	0	0	0	0	0	0	0
		10 MeV (nGd)	0	0	0	0	0	0	0	0
		10 MeV (nH)	0	0	0	0	0	0	0	0
	± 1000	5 MeV (nGd)	8	4	4	6	0	1	1	0

continued D.5 IBD selected candidates assuming monochromatic spectra.

GW	T_w	E_ν	EH1		EH2		EH1			
			AD1	AD2	AD1	AD2	AD1	AD2	AD3	AD4
GW170104		5 MeV (nH)	3	4	5	1	1	0	2	0
		7 MeV (nGd)	2	4	1	4	0	0	1	0
		7 MeV (nH)	3	0	3	0	0	0	0	1
		10 MeV (nGd)	0	0	0	0	0	0	0	0
		10 MeV (nH)	0	0	0	0	0	0	0	0
	± 10	5 MeV (nGd)	–	–	0	0	0	0	0	0
		5 MeV (nH)	–	–	0	0	0	0	0	0
		7 MeV (nGd)	–	–	0	0	0	0	0	0
		7 MeV (nH)	–	–	0	0	0	0	0	0
		10 MeV (nGd)	–	–	0	0	0	0	0	0
± 1000	10 MeV (nH)	–	–	0	0	0	0	0	0	
	5 MeV (nGd)	–	–	4	7	0	0	1	0	
	5 MeV (nH)	–	–	3	5	1	0	0	1	
	7 MeV (nGd)	–	–	2	0	0	0	0	0	
	7 MeV (nH)	–	–	1	1	0	0	0	0	
GW170608	± 10	10 MeV (nGd)	–	–	0	0	0	0	0	0
		10 MeV (nH)	–	–	0	0	0	0	0	0
		5 MeV (nGd)	–	0	0	0	0	0	0	0
		5 MeV (nH)	–	0	0	0	0	0	0	0
		7 MeV (nGd)	–	0	0	0	0	0	0	0
	± 1000	7 MeV (nH)	–	0	0	0	0	0	0	0
		5 MeV (nGd)	–	4	7	3	1	0	0	0
		5 MeV (nH)	–	5	4	2	0	1	0	0
		7 MeV (nGd)	–	3	2	3	0	0	0	0
		7 MeV (nH)	–	0	1	1	0	0	0	0
GW170814	± 10	10 MeV (nGd)	–	0	0	0	0	0	0	0
		10 MeV (nH)	–	0	0	0	0	0	0	0
		5 MeV (nGd)	–	0	0	0	0	0	0	0
		5 MeV (nH)	–	1	0	0	0	0	0	0
	± 1000	7 MeV (nGd)	–	0	0	0	0	0	0	0
		7 MeV (nH)	–	0	0	0	0	0	0	0
		5 MeV (nGd)	–	6	5	7	0	1	0	0
		5 MeV (nH)	–	6	2	4	0	1	0	1

 ± 1000

continued D.5 IBD selected candidates assuming monochromatic spectra.

GW	T_w	E_ν	EH1		EH2		EH1			
			AD1	AD2	AD1	AD2	AD1	AD2	AD3	AD4
GW170817		7 MeV (nGd)	–	2	1	2	0	0	0	1
		7 MeV (nH)	–	4	0	0	1	0	0	0
		10 MeV (nGd)	–	0	0	0	0	0	0	0
		10 MeV (nH)	–	0	0	0	0	0	0	0
	± 10	5 MeV (nGd)	–	0	0	0	0	0	0	0
		5 MeV (nH)	–	0	0	0	0	0	0	0
		7 MeV (nGd)	–	0	0	0	0	0	0	0
		7 MeV (nH)	–	0	0	0	0	0	0	0
		10 MeV (nGd)	–	0	0	0	0	0	0	0
		10 MeV (nH)	–	0	0	0	0	0	0	0
	± 1000	5 MeV (nGd)	–	6	6	7	1	0	0	1
		5 MeV (nH)	–	3	5	6	2	0	1	1
		7 MeV (nGd)	–	5	3	0	0	0	0	0
		7 MeV (nH)	–	2	2	1	1	0	0	0
10 MeV (nGd)		–	0	0	0	0	0	0	0	
10 MeV (nH)		–	0	0	0	0	0	0	0	

 Table D.13 IBD candidates in ± 10 s and ± 1000 s search time windows are listed assuming the Fermi-Dirac spectrum. “LE” represents the low-energy region $E_p < 10$ MeV, and “HE” represents the high-energy region $E_p > 10$ MeV.

GW	T_w [s]	E_ν [MeV]	EH1		EH2		EH3			
			AD1	AD2	AD1	AD2	AD1	AD2	AD3	AD4
GW150914	± 10	LE (nGd)	0	0	0	0	0	0	0	0
		LE (nH)	0	0	0	0	0	0	0	0
		HE (nGd)	0	0	0	0	0	0	0	0
		HE (nH)	0	0	0	0	0	0	0	0
	± 1000	LE (nGd)	14	12	12	12	1	0	1	2
		LE (nH)	7	2	5	3	0	0	0	1
		HE (nGd)	0	0	0	0	0	0	0	0
		HE (nH)	0	0	0	0	0	0	0	0
GW151012	± 10	LE (nGd)	0	0	0	0	0	0	0	0
		LE (nH)	0	0	0	0	0	0	0	0
		HE (nGd)	0	0	0	0	0	0	0	0
		HE (nH)	0	0	0	0	0	0	0	0
	± 1000	LE (nGd)	11	18	12	11	1	4	2	1
		LE (nH)	7	4	2	6	1	0	1	0

continued D.13 IBD selected candidates assuming the Fermi-Dirac spectrum.

GW	T_w	E_ν	EH1		EH2		EH3				
			AD1	AD2	AD1	AD2	AD1	AD2	AD3	AD4	
GW151226		HE (nGd)	0	0	0	0	0	0	0	0	
		HE (nH)	0	0	0	0	0	0	0	0	
	± 10	LE (nGd)	0	0	0	0	0	0	0	0	
		LE (nH)	0	0	0	0	0	0	0	0	
		HE (nGd)	0	0	0	0	0	0	0	0	
		HE (nH)	0	0	0	0	0	0	0	0	
	± 1000	LE (nGd)	15	17	14	17	2	1	4	1	
		LE (nH)	6	3	7	1	1	0	1	1	
		HE (nGd)	0	0	0	0	0	0	0	0	
		HE (nH)	0	0	0	0	0	0	0	0	
	GW170104	± 10	LE (nGd)	–	–	0	0	0	0	0	0
			LE (nH)	–	–	0	0	0	0	0	0
HE (nGd)			–	–	0	0	0	0	0	0	
HE (nH)			–	–	0	0	0	0	0	0	
± 1000		LE (nGd)	–	–	14	18	3	0	3	2	
		LE (nH)	–	–	4	5	1	0	0	1	
		HE (nGd)	–	–	0	0	0	0	0	0	
		HE (nH)	–	–	0	0	0	0	0	0	
GW170608	± 10	LE (nGd)	–	0	0	0	0	0	0	0	
		LE (nH)	–	0	0	0	0	0	0	0	
		HE (nGd)	–	0	0	0	0	0	0	0	
		HE (nH)	–	0	0	0	0	0	0	0	
	± 1000	LE (nGd)	–	15	20	12	1	1	2	0	
		LE (nH)	–	4	3	3	0	0	0	0	
		HE (nGd)	–	0	0	0	0	0	0	0	
		HE (nH)	–	0	0	0	0	0	0	0	
GW170814	± 10	LE (nGd)	–	0	1	0	0	0	0	0	
		LE (nH)	–	1	0	0	0	0	0	0	
		HE (nGd)	–	0	0	0	0	0	0	0	
		HE (nH)	–	0	0	0	0	0	0	0	
	± 1000	LE (nGd)	–	14	12	13	0	4	1	1	
		LE (nH)	–	10	2	4	1	1	0	1	
		HE (nGd)	–	0	0	0	0	0	0	0	
		HE (nH)	–	0	0	0	0	0	0	0	
	± 10	LE (nGd)	–	0	0	0	0	0	0		
		LE (nH)	–	0	0	0	0	0	0		
		HE (nGd)	–	0	0	0	0	0	0		

GW170817

continued D.13 IBD selected candidates assuming the Fermi-Dirac spectrum.

GW	T_w	E_ν	EH1		EH2		EH3			
			AD1	AD2	AD1	AD2	AD1	AD2	AD3	AD4
		HE (nH)	–	0	0	0	0	0	0	0
		LE (nGd)	–	17	15	12	2	2	0	2
	± 1000	LE (nH)	–	4	6	7	2	0	1	1
		HE (nGd)	–	0	0	0	0	0	0	0
		HE (nH)	–	0	0	0	0	0	0	0

Table D.1 For the low-energy data point, $5 \text{ MeV } E_\nu$, the IBD candidates were searched associated with all GW events within the time window of $\pm 500 \text{ s}$. The “S” represents the number of IBD candidates. The “B” represents the expected background number.

GW	EH1-AD1		EH1-AD2		EH2-AD1		EH2-AD2		EH3-AD1		EH3-AD2		EH3-AD3		EH3-AD4		
	S	B	S	B	S	B	S	B	S	B	S	B	S	B	S	B	
GW150914	nGd	1	2.55±0.05	0	2.46±0.05	2	2.45±0.05	3	2.42±0.05	0	0.35±0.02	0	0.38±0.02	0	0.34±0.02	0	0.35±0.02
	nH	2	2.09±0.05	1	2.08±0.05	2	1.96±0.04	2	1.93±0.04	0	0.32±0.02	0	0.32±0.02	0	0.30±0.02	0	0.34±0.02
GW151012	nGd	1	2.30±0.04	1	2.34±0.04	1	1.75±0.04	3	1.67±0.05	0	0.28±0.02	1	0.28±0.02	0	0.28±0.02	1	0.30±0.02
	nH	2	1.94±0.04	2	1.97±0.04	2	1.44±0.04	2	1.42±0.03	1	0.28±0.02	0	0.27±0.02	0	0.27±0.02	0	0.27±0.02
GW151226	nGd	4	2.41±0.05	2	2.54±0.05	1	2.41±0.05	2	2.30±0.05	0	0.33±0.02	0	0.35±0.02	0	0.34±0.02	0	0.35±0.02
	nH	2	2.10±0.05	3	2.10±0.05	3	1.95±0.05	1	2.03±0.05	1	0.29±0.02	0	0.33±0.02	0	0.29±0.02	0	0.34±0.02
GW170104	nGd	-	-	-	-	1	2.27±0.06	4	2.19±0.06	0	0.36±0.02	0	0.36±0.02	0	0.34±0.02	1	0.30±0.02
	nH	-	-	-	-	1	1.94±0.05	3	1.84±0.05	1	0.29±0.02	0	0.28±0.02	0	0.28±0.02	0	0.30±0.02
GW170608	nGd	-	-	0	2.54±0.04	5	2.41±0.06	2	2.30±0.06	0	0.34±0.02	0	0.35±0.02	0	0.31±0.02	0	0.35±0.02
	nH	-	-	2	1.96±0.06	2	1.94±0.06	2	1.94±0.05	0	0.30±0.02	0	0.29±0.02	0	0.32±0.02	0	0.30±0.02
GW170814	nGd	-	-	2	2.57±0.04	4	2.30±0.05	2	2.20±0.05	0	0.35±0.02	0	0.34±0.02	0	0.36±0.02	0	0.36±0.02
	nH	-	-	5	2.11±0.05	0	1.98±0.04	2	2.00±0.04	0	0.30±0.02	0	0.31±0.02	0	0.30±0.02	0	0.31±0.02
GW170817	nGd	-	-	3	2.56±0.05	4	2.33±0.05	3	2.24±0.05	0	0.33±0.02	0	0.33±0.02	0	0.33±0.02	1	0.37±0.02
	nH	-	-	2	2.10±0.05	0	1.89±0.04	3	1.94±0.04	2	0.30±0.02	0	0.32±0.02	1	0.30±0.02	0	0.31±0.02

Table D.2 For the low-energy data point, 7 MeV E_ν , the IBD candidates are searched associated with all GW events within the time window of ± 500 s. The “S” represents the number of IBD candidates. The “B” represents the expected background number.

GW	EH1-AD1		EH1-AD2		EH2-AD1		EH2-AD2		EH3-AD1		EH3-AD2		EH3-AD3		EH3-AD4		
	S	B	S	B	S	B	S	B	S	B	S	B	S	B	S	B	
GW150914	nGd	3	0.90±0.03	1	0.93±0.03	0	0.86±0.03	1	0.86±0.03	0	0.13±0.01	0	0.13±0.01	0	0.15±0.01	1	0.14±0.01
	nH	2	0.75±0.03	0	0.79±0.03	0	0.70±0.03	0	0.75±0.03	0	0.11±0.01	0	0.10±0.01	0	0.10±0.01	0	0.09±0.01
GW151012	nGd	0	0.86±0.03	1	0.89±0.03	0	0.58±0.02	2	0.60±0.02	0	0.12±0.01	0	0.11±0.01	0	0.11±0.01	0	0.12±0.01
	nH	1	0.66±0.02	1	0.73±0.02	0	0.55±0.02	1	0.52±0.02	0	0.09±0.01	0	0.08±0.01	0	0.09±0.01	0	0.08±0.01
GW151226	nGd	1	0.84±0.03	0	0.94±0.03	0	0.92±0.03	3	0.86±0.03	0	0.13±0.01	0	0.12±0.01	1	0.11±0.01	0	0.13±0.01
	nH	2	0.73±0.02	0	0.78±0.03	2	0.72±0.03	0	0.75±0.03	0	0.10±0.01	0	0.10±0.01	0	0.09±0.01	1	0.11±0.01
GW170104	nGd	-	-	-	-	2	0.88±0.03	0	0.85±0.03	0	0.12±0.01	0	0.11±0.01	0	0.13±0.01	0	0.13±0.01
	nH	-	-	-	-	0	0.71±0.03	1	0.68±0.03	0	0.08±0.01	0	0.10±0.01	0	0.10±0.01	0	0.10±0.01
GW170608	nGd	-	-	3	0.94±0.02	1	0.89±0.04	1	0.86±0.04	0	0.13±0.02	0	0.13±0.02	0	0.12±0.01	0	0.10±0.01
	nH	-	-	0	0.71±0.04	1	0.66±0.03	0	0.70±0.03	0	0.11±0.01	0	0.11±0.01	0	0.13±0.01	0	0.11±0.01
GW170814	nGd	-	-	1	0.89±0.03	1	0.89±0.03	2	0.82±0.03	0	0.06±0.01	0	0.06±0.01	0	0.04±0.01	1	0.05±0.01
	nH	-	-	1	0.75±0.03	0	0.69±0.03	0	0.68±0.03	0	0.05±0.01	0	0.04±0.01	0	0.04±0.01	0	0.05±0.01
GW170817	nGd	-	-	3	0.91±0.03	2	0.88±0.03	0	0.83±0.01	0	0.12±0.01	0	0.14±0.01	0	0.13±0.01	0	0.12±0.01
	nH	-	-	1	0.71±0.03	2	0.68±0.03	0	0.66±0.03	0	0.12±0.01	0	0.12±0.01	0	0.10±0.01	0	0.10±0.01

Table D.3 For the low-energy data point, 10 MeV E_ν , the IBD candidates are searched associated with all GW events within the time window of ± 500 s. The “S” represents the number of IBD candidates. The “B” represents the expected background number.

GW	EH1-AD1		EH1-AD2		EH2-AD1		EH2-AD2		EH3-AD1		EH3-AD2		EH3-AD3		EH3-AD4	
	S	B	S	B	S	B	S	B	S	B	S	B	S	B	S	B
GW150914	nGd	0.02 ± 0.004	0	0.02 ± 0.004	0	0.02 ± 0.004	0	0.02 ± 0.004	0	0.006 ± 0.002	0	0.006 ± 0.002	0	0.004 ± 0.002	0	0.003 ± 0.001
	nH	0.02 ± 0.004	0	0.02 ± 0.005	0	0.02 ± 0.004	0	0.02 ± 0.004	0	0.001 ± 0.001	0	0.002 ± 0.001	0	0.001 ± 0.001	0	0.001 ± 0.001
GW151012	nGd	0.02 ± 0.004	0	0.01 ± 0.003	0	0.01 ± 0.003	0	0.01 ± 0.003	0	0.001 ± 0.001	0	0.002 ± 0.001	0	0.001 ± 0.001	0	0.001 ± 0.001
	nH	0.01 ± 0.003	0	0.02 ± 0.004	0	0.02 ± 0.004	0	0.02 ± 0.004	0	0.002 ± 0.001	0	0.003 ± 0.002	0	0.005 ± 0.002	0	0.002 ± 0.001
GW151226	nGd	0.01 ± 0.004	0	0.02 ± 0.004	0	0.02 ± 0.004	0	0.01 ± 0.003	0	0.001 ± 0.001	0	0.001 ± 0.001	0	0.001 ± 0.001	0	0.003 ± 0.002
	nH	0.02 ± 0.004	0	0.02 ± 0.004	0	0.02 ± 0.004	0	0.02 ± 0.004	0	0.001 ± 0.001	0	0.001 ± 0.001	0	0.001 ± 0.001	0	0.004 ± 0.002
GW170104	nGd	-	-	0.02 ± 0.004	0	0.02 ± 0.004	0	0.01 ± 0.004	0	0.003 ± 0.002	0	0.001 ± 0.001	0	0.001 ± 0.001	0	0.001 ± 0.001
	nH	-	-	0.01 ± 0.004	0	0.01 ± 0.004	0	0.02 ± 0.005	0	0.001 ± 0.001	0	0.001 ± 0.001	0	0.001 ± 0.001	0	0.001 ± 0.001
GW170608	nGd	-	0	0.02 ± 0.005	0	0.02 ± 0.005	0	0.02 ± 0.005	0	0.001 ± 0.001	0	0.001 ± 0.001	0	0.001 ± 0.001	0	0.003 ± 0.002
	nH	-	0	0.02 ± 0.005	0	0.02 ± 0.005	0	0.02 ± 0.005	0	0.003 ± 0.002	0	0.001 ± 0.001	0	0.002 ± 0.002	0	0.002 ± 0.002
GW170814	nGd	-	0	0.02 ± 0.004	0	0.02 ± 0.004	0	0.02 ± 0.004	0	0.002 ± 0.001	0	0.001 ± 0.001	0	0.004 ± 0.002	0	0.002 ± 0.001
	nH	-	0	0.02 ± 0.004	0	0.02 ± 0.004	0	0.02 ± 0.004	0	0.003 ± 0.002	0	0.004 ± 0.002	0	0.001 ± 0.001	0	0.004 ± 0.002
GW170817	nGd	-	0	0.02 ± 0.003	0	0.01 ± 0.003	0	0.02 ± 0.004	0	0.002 ± 0.001	0	0.001 ± 0.001	0	0.004 ± 0.002	0	0.003 ± 0.002
	nH	-	0	0.02 ± 0.004	0	0.02 ± 0.004	0	0.02 ± 0.004	0	0.005 ± 0.002	0	0.005 ± 0.002	0	0.001 ± 0.001	0	0.003 ± 0.002

Table D.4 For the high-energy points, 20 MeV, 30 MeV, 50 MeV, 70 MeV, and 90 MeV, the background rate is determined by integrating the energy range $E_p \pm \Delta$ using the prompt spectrum in Fig. 6.18. The time window is ± 500 s. The “S” represents the number of IBD candidates. The “B” represents the expected background number.

E_ν	S		B		B		B		B		B		B	
	(EH1-AD1)	(EH1-AD2)	(EH2-AD1)	(EH2-AD2)	(EH3-AD1)	(EH3-AD2)	(EH3-AD2)	(EH3-AD2)	(EH3-AD3)	(EH3-AD3)	(EH3-AD4)	(EH3-AD4)	(EH3-AD4)	(EH3-AD4)
nGd														
20 MeV	0	0.0039 ± 0.00017	0.0040 ± 0.00016	0.0028 ± 0.00014	0.0029 ± 0.00014	0.0018 ± 0.00003	0.0028 ± 0.00004	0.0028 ± 0.00004	0.0033 ± 0.00005	0.0033 ± 0.00005	0.0036 ± 0.00005	0.0036 ± 0.00005	0.0036 ± 0.00005	0.0036 ± 0.00005
30 MeV	0	0.0048 ± 0.00019	0.0050 ± 0.00018	0.0035 ± 0.00015	0.0032 ± 0.00016	0.0044 ± 0.00005	0.0035 ± 0.00005	0.0035 ± 0.00005	0.0047 ± 0.00006	0.0047 ± 0.00006	0.0039 ± 0.00005	0.0039 ± 0.00005	0.0039 ± 0.00005	0.0039 ± 0.00005
50 MeV	0	0.0061 ± 0.00021	0.0060 ± 0.00020	0.0045 ± 0.00018	0.0044 ± 0.00018	0.0044 ± 0.00005	0.0042 ± 0.00005	0.0042 ± 0.00005	0.0056 ± 0.00006	0.0056 ± 0.00006	0.0049 ± 0.00006	0.0049 ± 0.00006	0.0049 ± 0.00006	0.0049 ± 0.00006
70 MeV	0	0.0061 ± 0.00022	0.0066 ± 0.00021	0.0044 ± 0.00017	0.0044 ± 0.00018	0.0039 ± 0.00005	0.0049 ± 0.00006	0.0049 ± 0.00006	0.006 ± 0.00006	0.006 ± 0.00006	0.0057 ± 0.00007	0.0057 ± 0.00007	0.0057 ± 0.00007	0.0057 ± 0.00007
90 MeV	0	0.0064 ± 0.00022	0.0070 ± 0.00020	0.0043 ± 0.0002	0.0048 ± 0.00020	0.0051 ± 0.00006	0.0057 ± 0.00006	0.0057 ± 0.00006	0.006 ± 0.00006	0.006 ± 0.00006	0.0054 ± 0.00006	0.0054 ± 0.00006	0.0054 ± 0.00006	0.0054 ± 0.00006
nH														
20 MeV	0	0.0069 ± 0.00023	0.0069 ± 0.00022	0.0049 ± 0.00018	0.0046 ± 0.00019	0.0052 ± 0.00006	0.004 ± 0.00005	0.004 ± 0.00005	0.004 ± 0.00005	0.004 ± 0.00005	0.0043 ± 0.00006	0.0043 ± 0.00006	0.0043 ± 0.00006	0.0043 ± 0.00006
30 MeV	0	0.0069 ± 0.00023	0.0069 ± 0.00022	0.0054 ± 0.00019	0.0054 ± 0.00020	0.0057 ± 0.000062	0.005 ± 0.00006	0.005 ± 0.00006	0.0057 ± 0.00006	0.0057 ± 0.00006	0.0056 ± 0.00006	0.0056 ± 0.00006	0.0056 ± 0.00006	0.0056 ± 0.00006
50 MeV	0	0.0079 ± 0.00025	0.0075 ± 0.00023	0.0060 ± 0.00020	0.0052 ± 0.0002	0.0056 ± 0.00006	0.0063 ± 0.00007	0.0063 ± 0.00007	0.0060 ± 0.00006	0.0060 ± 0.00006	0.0051 ± 0.00006	0.0051 ± 0.00006	0.0051 ± 0.00006	0.0051 ± 0.00006
70 MeV	0	0.0073 ± 0.00024	0.0076 ± 0.00023	0.0060 ± 0.00020	0.0057 ± 0.0002	0.0073 ± 0.00007	0.0055 ± 0.00006	0.0055 ± 0.00006	0.0067 ± 0.00008	0.0067 ± 0.00008	0.0068 ± 0.00007	0.0068 ± 0.00007	0.0068 ± 0.00007	0.0068 ± 0.00007
90 MeV	0	0.0069 ± 0.00023	0.0074 ± 0.00023	0.0049 ± 0.0002	0.0051 ± 0.0002	0.0062 ± 0.00006	0.006 ± 0.00006	0.006 ± 0.00006	0.0056 ± 0.00006	0.0056 ± 0.00006	0.0054 ± 0.00006	0.0054 ± 0.00006	0.0054 ± 0.00006	0.0054 ± 0.00006

Table D.6 IBD candidates in different data sources and the expected background numbers associated with GW150914 within time window ± 500 s. The “SIG” represents the IBD candidates. The “BKG” represents the expect background numbers.

Det.	Low energy data				High energy data			
	nGd		nH		nGd		nH	
	SIG.	BKG.	SIG.	BKG.	SIG.	BKG.	SIG.	BKG.
AD1	4	6.96 ± 0.08	4	2.52 ± 0.06	0	0.060 ± 0.008	0	0.080 ± 0.009
AD2	5	6.95 ± 0.08	1	2.54 ± 0.05	0	0.054 ± 0.007	0	0.072 ± 0.008
AD3	4	6.62 ± 0.08	2	2.37 ± 0.05	0	0.037 ± 0.006	0	0.041 ± 0.006
AD4	8	6.46 ± 0.08	1	2.35 ± 0.05	0	0.027 ± 0.005	0	0.056 ± 0.008
AD5	0	0.97 ± 0.03	0	0.37 ± 0.02	0	0.004 ± 0.002	0	0.008 ± 0.003
AD6	0	1.00 ± 0.03	0	0.36 ± 0.02	0	0.003 ± 0.002	0	0.007 ± 0.003
AD7	0	0.97 ± 0.03	0	0.34 ± 0.02	0	0.001 ± 0.001	0	0.004 ± 0.002
AD8	1	0.97 ± 0.03	0	0.36 ± 0.02	0	0.007 ± 0.002	0	0.005 ± 0.002

Table D.7 IBD candidates in different classes and the expected background numbers associated with GW151012 within time window ± 500 s. The “SIG” represents the IBD candidates. The “BKG” represents the expect background numbers.

Class	Low energy data				High energy data			
	nGd		nH		nGd		nH	
	SIG.	BKG.	SIG.	BKG.	SIG.	BKG.	SIG.	BKG.
AD1	6	6.46 ± 0.07	3	2.29 ± 0.04	0	0.047 ± 0.006	0	0.079 ± 0.008
AD2	7	6.54 ± 0.07	1	2.29 ± 0.04	0	0.056 ± 0.007	0	0.074 ± 0.008
AD3	5	4.63 ± 0.06	1	1.76 ± 0.04	0	0.025 ± 0.005	0	0.057 ± 0.007
AD4	6	4.60 ± 0.06	3	1.75 ± 0.04	0	0.042 ± 0.006	0	0.057 ± 0.007
AD5	1	0.79 ± 0.03	1	0.34 ± 0.02	0	0.005 ± 0.002	0	0.008 ± 0.003
AD6	3	0.76 ± 0.03	0	0.31 ± 0.02	0	0.006 ± 0.002	0	0.003 ± 0.002
AD7	1	0.76 ± 0.03	0	0.30 ± 0.02	0	0.009 ± 0.003	0	0.005 ± 0.002
AD8	1	0.81 ± 0.03	0	0.31 ± 0.02	0	0.005 ± 0.002	0	0.002 ± 0.001

Table D.8 IBD candidates in different classes and the expected background numbers associated with GW151226 within time window ± 500 s. The “SIG” represents the IBD candidates. The “BKG” represents the expect background numbers.

Class	Low energy data				High energy data			
	nGd		nH		nGd		nH	
	SIG.	BKG.	SIG.	BKG.	SIG.	BKG.	SIG.	BKG.
AD1	6	6.64 ± 0.08	4	2.45 ± 0.05	0	0.044 ± 0.007	0	0.080 ± 0.009
AD2	4	7.09 ± 0.09	2	2.57 ± 0.05	0	0.038 ± 0.007	0	0.053 ± 0.008
AD3	4	6.56 ± 0.08	4	2.35 ± 0.05	0	0.034 ± 0.006	0	0.043 ± 0.007
AD4	9	6.42 ± 0.08	1	2.44 ± 0.05	0	0.038 ± 0.006	0	0.051 ± 0.008
AD5	1	0.92 ± 0.03	1	0.39 ± 0.02	0	0.006 ± 0.003	0	0.002 ± 0.001
AD6	0	0.96 ± 0.03	0	0.38 ± 0.02	0	0.001 ± 0.001	0	0.006 ± 0.003
AD7	3	0.88 ± 0.03	0	0.35 ± 0.02	0	0.003 ± 0.001	0	0.007 ± 0.003
AD8	1	0.98 ± 0.03	1	0.40 ± 0.02	0	0.004 ± 0.002	0	0.005 ± 0.002

Table D.9 IBD candidates in different classes and the expected background numbers associated with GW170104 within time window ± 500 s. The “SIG” represents the IBD candidates. The “BKG” represents the expect background numbers.

Class	Low energy data				High energy data			
	nGd		nH		nGd		nH	
	SIG.	BKG.	SIG.	BKG.	SIG.	BKG.	SIG.	BKG.
AD1	–	–	–	–	–	–	–	–
AD2	–	–	–	–	–	–	–	–
AD3	7	6.48 ± 0.07	1	2.37 ± 0.06	0	0.040 ± 0.007	0	0.048 ± 0.008
AD4	13	6.11 ± 0.09	3	2.23 ± 0.06	0	0.033 ± 0.007	0	0.057 ± 0.009
AD5	2	0.99 ± 0.04	1	0.31 ± 0.02	0	0.001 ± 0.001	0	0.003 ± 0.002
AD6	0	0.99 ± 0.04	0	0.33 ± 0.02	0	0.003 ± 0.001	0	0.001 ± 0.001
AD7	1	0.91 ± 0.04	0	0.30 ± 0.02	0	0.006 ± 0.003	0	0.004 ± 0.003
AD8	1	0.92 ± 0.04	0	0.34 ± 0.02	0	0.006 ± 0.003	0	0.004 ± 0.003

Table D.10 IBD candidates in different classes and the expected background numbers associated with GW170608 within time window ± 500 s. The “SIG” represents the IBD candidates. The “BKG” represents the expect background numbers.

Class	Low energy data				High energy data			
	nGd		nH		nGd		nH	
	SIG.	BKG.	SIG.	BKG.	SIG.	BKG.	SIG.	BKG.
AD1	–	–	–	–	–	–	–	–
AD2	9	7.17 ± 0.11	2	2.38 ± 0.06	0	0.063 ± 0.010	0	0.075 ± 0.011
AD3	11	6.55 ± 0.11	2	2.25 ± 0.06	0	0.056 ± 0.010	0	0.080 ± 0.012
AD4	6	6.42 ± 0.10	2	2.38 ± 0.06	0	0.065 ± 0.011	0	0.072 ± 0.011
AD5	0	0.95 ± 0.04	0	0.39 ± 0.03	0	0.003 ± 0.002	0	0.003 ± 0.002
AD6	1	0.96 ± 0.04	0	0.35 ± 0.02	0	0.007 ± 0.003	0	0.002 ± 0.002
AD7	1	0.92 ± 0.04	0	0.40 ± 0.03	0	0.002 ± 0.002	0	0.002 ± 0.002
AD8	0	0.93 ± 0.04	0	0.35 ± 0.02	0	0.010 ± 0.004	0	0.007 ± 0.003

 Table D.11 IBD candidates in different classes and the expected background numbers associated with GW170814 within time window ± 500 s. The “SIG” represents the IBD candidates. The “BKG” represents the expect background numbers.

Class	Low energy data				High energy data			
	nGd		nH		nGd		nH	
	SIG.	BKG.	SIG.	BKG.	SIG.	BKG.	SIG.	BKG.
AD1	–	–	–	–	–	–	–	–
AD2	9	6.94 ± 0.08	6	2.51 ± 0.05	0	0.081 ± 0.009	0	0.088 ± 0.009
AD3	9	6.36 ± 0.08	0	2.36 ± 0.05	0	0.042 ± 0.006	0	0.047 ± 0.007
AD4	6	6.29 ± 0.08	2	2.35 ± 0.05	0	0.039 ± 0.006	0	0.052 ± 0.007
AD5	0	0.94 ± 0.03	1	0.39 ± 0.02	0	0.006 ± 0.002	0	0.006 ± 0.002
AD6	2	0.97 ± 0.03	0	0.36 ± 0.02	0	0.002 ± 0.001	0	0.009 ± 0.003
AD7	1	0.95 ± 0.03	0	0.34 ± 0.02	0	0.005 ± 0.002	0	0.013 ± 0.004
AD8	1	1.00 ± 0.03	0	0.36 ± 0.02	0	0.002 ± 0.001	0	0.006 ± 0.002

Table D.12 IBD candidates in different classes and the expected background numbers associated with GW170817 within time window ± 500 s. The “SIG” represents the IBD candidates. The “BKG” represents the expected background numbers.

Class	Low energy data				High energy data			
	nGd		nH		nGd		nH	
	SIG.	BKG.	SIG.	BKG.	SIG.	BKG.	SIG.	BKG.
AD1	–	–	–	–	–	–	–	–
AD2	8	7.02 ± 0.09	3	2.45 ± 0.05	0	0.079 ± 0.010	0	0.095 ± 0.011
AD3	9	6.31 ± 0.08	2	2.28 ± 0.05	0	0.043 ± 0.007	0	0.051 ± 0.007
AD4	6	6.32 ± 0.08	3	2.29 ± 0.05	0	0.043 ± 0.007	0	0.050 ± 0.007
AD5	0	0.92 ± 0.03	1	0.38 ± 0.02	0	0.007 ± 0.003	0	0.007 ± 0.003
AD6	1	0.98 ± 0.03	0	0.38 ± 0.02	0	0.004 ± 0.002	0	0.008 ± 0.003
AD7	0	0.94 ± 0.03	1	0.35 ± 0.02	0	0.003 ± 0.002	0	0.011 ± 0.003
AD8	2	0.98 ± 0.03	0	0.35 ± 0.02	0	0.003 ± 0.002	0	0.002 ± 0.001

Appendix E Summary parameters to calculate neutrino fluence

Table E.1 Summary of parameters to calculate the low-energy neutrino fluence assuming the monochromatic spectra under ± 500 s time window. The muon veto efficiency are the averaged muon efficiency of all GW events. We averaged all the IBD candidates and the background numbers. “LE” represents the low-energy points, namely 5 MeV, 7 MeV, and 9 MeV. “HE” represents the high-energy points, namely 20 MeV, 30 MeV, 50 MeV, 70 MeV, and 90 MeV.

E_ν	EH1				EH2		EH3			$F(\bar{\nu}_e)$ $\times 10^{10} \text{ cm}^{-2}$	
	AD1	AD2	AD1	AD2	AD1	AD2	AD1	AD2	AD3		AD4
Common	ϵ_μ (nGd)	80.08%	79.56%	83.75%	83.65%	98.27%	98.27%	98.24%	98.24%	98.26%	
	ϵ_μ (nH)	76.96%	76.45%	81.25%	81.20%	98.08%	98.04%	98.05%	98.05%	98.04%	
	ϵ_m (nGd)	97.74%	97.77%	97.87%	97.85%	97.88%	97.88%	97.88%	97.88%	97.86%	
	ϵ_m (nH)	98.47%	98.48%	98.51%	98.51%	98.52%	98.50%	98.51%	98.51%	98.49%	
	N_P	$(3.15 \pm 0.02) \times 10^{30}$									
5 MeV	ϵ_{MC} (nGd)	$36.07 \pm 0.10\%$									
	ϵ_{MC} (nH)	$30.78 \pm 0.13\%$									
	σ	$1.27 \times 10^{-42} \text{ cm}^2$									
	BKG. (nGd)	2.42 ± 0.05	2.50 ± 0.05	2.27 ± 0.05	2.19 ± 0.05	0.33 ± 0.02	0.34 ± 0.02	0.34 ± 0.02	0.34 ± 0.02	0.34 ± 0.02	0.34 ± 0.02
	BKG. (nH)	2.04 ± 0.05	2.05 ± 0.05	1.87 ± 0.05	1.87 ± 0.05	0.30 ± 0.02	0.30 ± 0.02	0.29 ± 0.02	0.29 ± 0.02	0.31 ± 0.02	0.31 ± 0.02
	SIG. (nGd)	2	1.33	2.57	2.71	0	0.14	0	0	0.43	0
	SIG. (nH)	2	2.5	1.43	2.14	0.71	0	0.14	0	0	0
	ϵ_{MC} (nGd)	$36.20 \pm 0.10\%$									
	ϵ_{MC} (nH)	$31.48 \pm 0.09\%$									
	σ	$2.96 \times 10^{-42} \text{ cm}^2$									
7 MeV	BKG. (nGd)	0.87 ± 0.03	0.92 ± 0.03	0.84 ± 0.03	0.81 ± 0.03	0.12 ± 0.01	0.11 ± 0.01	0.11 ± 0.01	0.11 ± 0.01	0.11 ± 0.01	0.11 ± 0.01
	BKG. (nH)	0.71 ± 0.02	0.75 ± 0.03	0.67 ± 0.03	0.68 ± 0.03	0.094 ± 0.01	0.093 ± 0.01	0.093 ± 0.01	0.093 ± 0.01	0.091 ± 0.01	0.091 ± 0.01
	SIG. (nGd)	1.33	1.5	0.86	1.29	0	0	0	0.14	0.43	0
	SIG. (nH)	1.67	0.5	0.71	0.29	0	0	0	0	0.14	0
	ϵ_{MC} (nGd)	$36.31 \pm 0.09\%$									
	ϵ_{MC} (nH)	$31.71 \pm 0.08\%$									
	σ	$6.76 \times 10^{-42} \text{ cm}^2$									
	BKG. (nGd)	0.08 ± 0.01	0.08 ± 0.01	0.08 ± 0.01	0.07 ± 0.01	0.01 ± 0.0003	0.01 ± 0.0003	0.01 ± 0.0003	0.01 ± 0.0003	0.01 ± 0.0003	0.01 ± 0.0003
	BKG. (nH)	0.07 ± 0.01	0.08 ± 0.01	0.07 ± 0.01	0.07 ± 0.01	0.01 ± 0.0003	0.01 ± 0.0003	0.01 ± 0.0003	0.01 ± 0.0003	0.01 ± 0.0003	0.01 ± 0.0003
	SIG. (nGd)	0	0.17	0	0	0	0	0	0	0	0
SIG. (nH)	0	0	0	0	0	0	0	0	0	0	
10 MeV	ϵ_{MC} (nGd)	$36.31 \pm 0.09\%$									
	ϵ_{MC} (nH)	$31.71 \pm 0.08\%$									
	σ	$6.76 \times 10^{-42} \text{ cm}^2$									
	BKG. (nGd)	0.08 ± 0.01	0.08 ± 0.01	0.08 ± 0.01	0.07 ± 0.01	0.01 ± 0.0003	0.01 ± 0.0003	0.01 ± 0.0003	0.01 ± 0.0003	0.01 ± 0.0003	0.01 ± 0.0003
	BKG. (nH)	0.07 ± 0.01	0.08 ± 0.01	0.07 ± 0.01	0.07 ± 0.01	0.01 ± 0.0003	0.01 ± 0.0003	0.01 ± 0.0003	0.01 ± 0.0003	0.01 ± 0.0003	0.01 ± 0.0003
	SIG. (nGd)	0	0.17	0	0	0	0	0	0	0	0
	SIG. (nH)	0	0	0	0	0	0	0	0	0	0
	ϵ_{MC} (nGd)	$36.23 \pm 0.16\%$									
	ϵ_{MC} (nH)	$31.95 \pm 0.11\%$									
	σ	$28.9 \times 10^{-42} \text{ cm}^2$									
20 MeV	BKG. (nGd $\times 10^{-3}$)	4.7 ± 0.2	3.6 ± 0.2	3.1 ± 0.2	2.6 ± 0.2	0.45 ± 0.07	0.49 ± 0.08	0.38 ± 0.06	0.38 ± 0.06	0.64 ± 0.08	
	BKG. (nH $\times 10^{-3}$)	9.0 ± 0.3	8.3 ± 0.3	5.7 ± 0.2	6.0 ± 0.3	0.76 ± 0.09	1.10 ± 0.11	1.0 ± 0.1	1.0 ± 0.1	0.51 ± 0.07	
	SIG. (nGd)	0	0	0	0	0	0	0	0	0	
	SIG. (nH)	0	0	0	0	0	0	0	0	0	

Table E.2 Summary of parameters to calculate the high-energy neutrino fluence assuming the monochromatic spectra under ± 500 s time window. We averaged all the IBD candidates and the background numbers. "LE" represents the low-energy points, namely 5 MeV, 7 MeV and 9 MeV. "HE" represents the high-energy points, namely 20 MeV, 30 MeV, 50 MeV, 70 MeV and 90 MeV.

E_ν	EHI			EH2			EH3			$F(\bar{\nu}_e)$ $\times 10^{10} \text{ cm}^{-2}$
	AD1	AD2	AD1	AD1	AD2	AD1	AD2	AD3	AD4	
30 MeV	ϵ_{MC} (nGd)			36.12 \pm 0.18%						
	ϵ_{MC} (nH)			31.92 \pm 0.08%						
	σ			63.0 $\times 10^{-42} \text{ cm}^2$						0.16
	BKG. (nGd $\times 10^{-3}$)	6.6 \pm 0.3	6.0 \pm 0.3	4.3 \pm 0.2	4.1 \pm 0.2	0.51 \pm 0.07	0.54 \pm 0.09	0.43 \pm 0.07	0.34 \pm 0.06	
	BKG. (nH $\times 10^{-3}$)	11.0 \pm 0.4	7.5 \pm 0.3	5.2 \pm 0.2	6.2 \pm 0.3	0.93 \pm 0.10	1.0 \pm 0.1	0.68 \pm 0.08	0.85 \pm 0.09	
	SIG. (nGd)	0	0	0	0	0	0	0	0	
	SIG. (nH)	0	0	0	0	0	0	0	0	
50 MeV	ϵ_{MC} (nGd)			35.71 \pm 0.18%						
	ϵ_{MC} (nH)			31.10 \pm 0.09%						
	σ			156 $\times 10^{-42} \text{ cm}^2$						0.05
	BKG. (nGd $\times 10^{-3}$)	5.7 \pm 0.2	6.3 \pm 0.3	4.9 \pm 0.2	3.6 \pm 0.2	0.96 \pm 0.10	0.95 \pm 0.10	0.75 \pm 0.09	0.11 \pm 0.03	
	BKG. (nH $\times 10^{-3}$)	7.9 \pm 0.3	6.9 \pm 0.3	6.3 \pm 0.3	4.3 \pm 0.2	0.53 \pm 0.08	0.85 \pm 0.09	0.53 \pm 0.08	0.32 \pm 0.06	
	SIG. (nGd)	0	0	0	0	0	0	0	0	
	SIG. (nH)	0	0	0	0	0	0	0	0	
70 MeV	ϵ_{MC} (nGd)			35.52 \pm 0.16%						
	ϵ_{MC} (nH)			30.69 \pm 0.11%						
	σ			268 $\times 10^{-42} \text{ cm}^2$						0.02
	BKG. (nGd $\times 10^{-3}$)	7.6 \pm 0.3	7.2 \pm 0.3	4.5 \pm 0.2	4.4 \pm 0.2	1.0 \pm 0.1	0.76 \pm 0.10	0.60 \pm 0.08	0.75 \pm 0.09	
	BKG. (nH $\times 10^{-3}$)	7.7 \pm 0.3	1.1 \pm 0.4	6.8 \pm 0.3	5.2 \pm 0.2	1.2 \pm 0.1	0.59 \pm 0.08	1.0 \pm 0.1	0.44 \pm 0.09	
	SIG. (nGd)	0	0	0	0	0	0	0	0	
	SIG. (nH)	0	0	0	0	0	0	0	0	
90 MeV	ϵ_{MC} (nGd)			35.02 \pm 0.15%						
	ϵ_{MC} (nH)			29.09 \pm 0.15%						
	σ			389 $\times 10^{-42} \text{ cm}^2$						0.01
	BKG. (nGd $\times 10^{-3}$)	5.7 \pm 0.2	8.5 \pm 0.3	4.0 \pm 0.2	4.0 \pm 0.2	0.77 \pm 0.09	0.49 \pm 0.08	0.38 \pm 0.06	0.58 \pm 0.08	
	BKG. (nH $\times 10^{-3}$)	7.8 \pm 0.3	9.5 \pm 0.3	5.4 \pm 0.2	6.4 \pm 0.3	0.57 \pm 0.08	0.57 \pm 0.08	0.9 \pm 0.1	1.1 \pm 0.1	
	SIG. (nGd)	0	0	0	0	0	0	0	0	
	SIG. (nH)	0	0	0	0	0	0	0	0	

Table E.3 Summary of parameters to calculate the neutrino fluence assuming the Fermi-Dirac spectrum within the time window ± 500 s. The “LE” represents the low-energy data $E_p < 10$ MeV. The “HE” represents the high-energy data $E_p > 10$ MeV. The “SIG” represents the averaged IBD candidates and the “BKG” represents the averaged background numbers.

	EH1				EH2				EH3			
	AD1	AD2	AD1	AD2	AD1	AD2	AD1	AD2	AD1	AD2	AD3	AD4
ϵ_μ (nGd)	80.08%	79.56%	83.75%	83.65%	98.27%	98.27%	98.27%	98.27%	98.27%	98.27%	98.24%	98.26%
ϵ_μ (nH)	76.96%	76.45%	81.25%	81.20%	98.08%	98.08%	98.08%	98.04%	98.08%	98.04%	98.05%	98.04%
ϵ_m (nGd)	97.74%	97.77%	97.87%	97.85%	97.88%	97.88%	97.88%	97.88%	97.88%	97.88%	97.88%	97.86%
ϵ_m (nH)	98.47%	98.48%	98.51%	98.51%	98.52%	98.52%	98.52%	98.50%	98.52%	98.50%	98.51%	98.49%
ϵ_{MC} (nGd)					LE: $4.28 \pm 0.11\%$ HE: $32.18 \pm 0.32\%$							
ϵ_{MC} (nH)					LE: $4.37 \pm 0.09\%$ HE: $27.70 \pm 0.25\%$							
N_P					$(3.15 \pm 0.02) \times 10^{30}$							
$\bar{\sigma}(E_\nu)$					$1.47 \times 10^{-41} \text{ cm}^2$							
LE BKG. (nGd)	6.57 ± 0.09	6.93 ± 0.10	6.16 ± 0.09	6.04 ± 0.09	0.92 ± 0.03	0.93 ± 0.04	0.92 ± 0.03	0.93 ± 0.04	0.90 ± 0.04	0.93 ± 0.04	0.90 ± 0.04	0.94 ± 0.04
LE BKG. (nH)	2.42 ± 0.06	2.46 ± 0.06	2.20 ± 0.06	2.17 ± 0.06	0.35 ± 0.02	0.34 ± 0.02	0.35 ± 0.02	0.34 ± 0.02	0.35 ± 0.02	0.34 ± 0.02	0.35 ± 0.02	0.37 ± 0.02
HE BKG. (nGd)	0.047 ± 0.008	0.064 ± 0.009	0.045 ± 0.007	0.042 ± 0.007	0.005 ± 0.002	0.004 ± 0.002	0.005 ± 0.002	0.004 ± 0.002	0.004 ± 0.002	0.004 ± 0.002	0.004 ± 0.002	0.006 ± 0.003
HE BKG. (nH)	0.067 ± 0.009	0.080 ± 0.010	0.054 ± 0.008	0.051 ± 0.008	0.005 ± 0.002	0.005 ± 0.002	0.005 ± 0.002	0.005 ± 0.002	0.007 ± 0.003	0.005 ± 0.002	0.007 ± 0.003	0.007 ± 0.003
LE SIG. (nGd)	5.33	7	7	7.71	0.57	1	0.57	1	1	1	1	1
LE SIG. (nH)	3.67	2.5	1.71	2.14	0.71	0	0.71	0	0.14	0	0.14	0.14
HE SIG. (nGd)	0	0	0	0	0	0	0	0	0	0	0	0
HE SIG. (nH)	0	0	0	0	0	0	0	0	0	0	0	0
Fluence					$0.45 \times 10^{10} \text{ cm}^{-2}$							

Appendix F IBD candidates for all GRBs

Table F.1 The average background rates during the Daya Bay live-time assuming the monochromatic spectra. The live-time has removed the search time for all GRBs-related ± 1000 s, which is the longest of the three time windows. For the different search time windows, one needs to multiply the different time lengths to get the corresponded background events.

E_ν (Rate: per second)	Data	EH1			EH2			EH3		
		AD1	AD2	AD1	AD2	AD1	AD2	AD3	AD4	
5 MeV ($\times 10^{-3}$)	nGd	2.20 \pm 0.01	2.25 \pm 0.01	2.09 \pm 0.01	2.09 \pm 0.01	2.09 \pm 0.01	0.30 \pm 0.01	0.30 \pm 0.01	0.30 \pm 0.01	0.30 \pm 0.01
	nH	1.92 \pm 0.01	1.85 \pm 0.01	1.74 \pm 0.01	1.84 \pm 0.01	1.84 \pm 0.01	0.27 \pm 0.01	0.27 \pm 0.01	0.28 \pm 0.01	0.29 \pm 0.01
7 MeV ($\times 10^{-4}$)	nGd	7.62 \pm 0.03	7.81 \pm 0.02	7.28 \pm 0.02	7.14 \pm 0.02	7.14 \pm 0.02	1.06 \pm 0.01	1.06 \pm 0.01	1.06 \pm 0.01	1.08 \pm 0.01
	nH	6.19 \pm 0.02	6.37 \pm 0.02	5.95 \pm 0.02	5.83 \pm 0.02	5.83 \pm 0.02	0.90 \pm 0.01	0.90 \pm 0.01	0.90 \pm 0.01	0.89 \pm 0.01
10 MeV ($\times 10^{-5}$)	nGd	1.57 \pm 0.04	1.54 \pm 0.03	1.31 \pm 0.03	1.26 \pm 0.03	1.26 \pm 0.03	0.16 \pm 0.01	0.19 \pm 0.01	0.20 \pm 0.01	0.20 \pm 0.01
	nH	1.91 \pm 0.03	1.90 \pm 0.03	1.55 \pm 0.03	1.46 \pm 0.03	1.46 \pm 0.03	0.20 \pm 0.01	0.20 \pm 0.01	0.20 \pm 0.01	0.20 \pm 0.01
20 MeV ($\times 10^{-6}$)	nGd	5.46 \pm 0.21	5.10 \pm 0.17	3.08 \pm 0.13	3.20 \pm 0.14	3.20 \pm 0.14	0.28 \pm 0.04	0.28 \pm 0.04	0.33 \pm 0.04	0.39 \pm 0.05
	nH	6.53 \pm 0.26	6.96 \pm 0.20	4.86 \pm 0.17	4.73 \pm 0.17	4.73 \pm 0.17	0.52 \pm 0.05	0.47 \pm 0.05	0.45 \pm 0.05	0.40 \pm 0.05
30 MeV ($\times 10^{-6}$)	nGd	6.75 \pm 0.24	6.31 \pm 0.19	3.92 \pm 0.15	3.67 \pm 0.15	3.67 \pm 0.15	0.48 \pm 0.05	0.34 \pm 0.04	0.43 \pm 0.05	0.43 \pm 0.05
	nH	6.74 \pm 0.20	6.84 \pm 0.20	5.13 \pm 0.17	5.25 \pm 0.18	5.25 \pm 0.18	0.51 \pm 0.06	0.53 \pm 0.06	0.51 \pm 0.05	0.66 \pm 0.06
50 MeV ($\times 10^{-6}$)	nGd	6.94 \pm 0.24	6.66 \pm 0.20	4.53 \pm 0.16	4.38 \pm 0.16	4.38 \pm 0.16	0.41 \pm 0.05	0.48 \pm 0.05	0.44 \pm 0.05	0.52 \pm 0.05
	nH	8.04 \pm 0.29	8.03 \pm 0.21	5.84 \pm 0.18	5.29 \pm 0.18	5.29 \pm 0.18	0.68 \pm 0.06	0.72 \pm 0.06	0.57 \pm 0.06	0.61 \pm 0.06
70 MeV ($\times 10^{-6}$)	nGd	7.38 \pm 0.25	7.42 \pm 0.21	4.68 \pm 0.16	4.58 \pm 0.17	4.58 \pm 0.17	0.47 \pm 0.05	0.51 \pm 0.05	0.51 \pm 0.06	0.56 \pm 0.06
	nH	9.05 \pm 0.23	9.04 \pm 0.23	5.99 \pm 0.20	6.09 \pm 0.20	6.09 \pm 0.20	0.75 \pm 0.06	0.60 \pm 0.06	0.64 \pm 0.06	0.71 \pm 0.07
90 MeV ($\times 10^{-6}$)	nGd	7.96 \pm 0.26	8.40 \pm 0.22	4.91 \pm 0.17	5.11 \pm 0.18	5.11 \pm 0.18	0.53 \pm 0.06	0.60 \pm 0.06	0.49 \pm 0.06	0.60 \pm 0.06
	nH	9.06 \pm 0.23	8.91 \pm 0.23	5.21 \pm 0.17	5.43 \pm 0.18	5.43 \pm 0.18	0.65 \pm 0.06	0.71 \pm 0.06	0.66 \pm 0.06	0.65 \pm 0.06

Table F.2 Total IBD candidates of ± 500 s assuming the monochromatic spectra. For the specified neutrino energy, the data samples include the nGd data and nH data.

T_w	E_ν	Data	EH1		EH2		EH3			
			AD1	AD2	AD1	AD2	AD1	AD2	AD3	AD4
± 500 s	5 MeV	nGd	2523	3753	3623	3208	513	525	476	481
		nH	2072	3174	2947	2600	502	454	469	435
	7 MeV	nGd	871	1362	1191	1132	180	176	177	166
		nH	655	1092	946	920	175	151	150	116
	10 MeV	nGd	22	33	21	16	2	2	3	5
		nH	18	33	31	16	5	3	4	4
	20 MeV	nGd	5	6	5	5	2	1	1	0
		nH	6	15	4	7	0	1	1	0
	30 MeV	nGd	3	15	4	6	0	2	3	1
		nH	10	6	5	10	1	0	0	1
	50 MeV	nGd	7	11	8	10	0	1	3	1
		nH	3	10	15	9	1	0	1	0
	70 MeV	nGd	10	18	16	7	2	0	1	0
		nH	7	19	9	7	1	2	1	1
	90 MeV	nGd	5	10	13	6	0	0	0	0
		nH	9	9	6	11	1	0	1	2

 Table F.3 Total IBD candidates in a ± 1000 s time window with the monochromatic spectra. For the specified neutrino energy, the data samples include the nGd data and nH data.

T_w	E_ν	Data	EH1		EH2		EH3			
			AD1	AD2	AD1	AD2	AD1	AD2	AD3	AD4
± 1000 s	5 MeV	nGd	5072	7515	7153	6467	994	1019	984	967
		nH	4093	6232	5794	5215	960	891	900	806
	7 MeV	nGd	1765	2687	2380	2252	356	346	357	302
		nH	1374	2118	1925	1853	319	307	306	242
	10 MeV	nGd	41	59	44	36	5	3	3	5
		nH	43	56	57	33	8	6	6	6
	20 MeV	nGd	7	11	12	12	3	1	1	1
		nH	12	26	13	11	0	1	1	0
	30 MeV	nGd	9	26	7	14	0	2	5	1
		nH	15	18	14	20	1	0	1	1
	50 MeV	nGd	15	20	18	16	0	1	4	2
		nH	21	23	24	16	3	0	2	1
	70 MeV	nGd	14	24	21	11	2	0	3	0
		nH	18	27	16	16	2	5	3	1
	90 MeV	nGd	22	18	18	16	1	0	3	2
		nH	16	21	15	18	3	0	1	2

Table F.4 Total IBD candidates of the dynamic time window assuming the monochromatic spectra. For the specified neutrino energy, the data samples include the nGd data and nH data.

T_w	E_ν	Data	EH1		EH2		EH3			
			AD1	AD2	AD1	AD2	AD1	AD2	AD3	AD4
$\pm T_{\text{Dyna S}}$	5 MeV	nGd	1180	1760	1629	1447	235	247	247	219
		nH	862	1359	1320	1197	196	209	206	190
	7 MeV	nGd	375	599	584	476	106	88	77	68
		nH	271	484	462	388	76	56	59	65
	10 MeV	nGd	6	12	10	9	1	0	2	0
		nH	11	9	15	10	3	4	0	2
	20 MeV	nGd	1	7	2	2	0	1	0	1
		nH	4	7	9	2	1	1	0	0
	30 MeV	nGd	3	5	2	3	0	1	2	0
		nH	2	4	5	4	0	1	0	0
	50 MeV	nGd	2	3	2	5	0	1	2	0
		nH	4	9	3	5	0	1	1	0
	70 MeV	nGd	1	7	1	2	1	0	1	0
		nH	1	5	1	4	1	1	0	0
	90 MeV	nGd	4	8	3	5	0	0	1	1
		nH	3	5	1	4	0	1	2	0

Acknowledgements

Firstly, I would like to give the most sincere respect to my supervisor Prof. Shaomin Chen and my associate supervisor Assoc. Prof. Zhe Wang. Many thanks for teaching me in scientific research and life during my Ph.D. time. I am always inspired and moved by Prof. Shaomin Chen by his intelligence and kindness. And I learned a rigorous research attitude from Prof. Zhe Wang. These experiences will be crucial later in my life.

Secondly, I would like to give grateful thanks to Prof. Yuanning Gao, Assoc. Prof. Zhenwei Yang, and Assoc. Prof. Xianglei Zhu, Assoc. Prof. Liming Zhang, and Assist. Prof. Benda Xu for their valuable suggestions in my Ph.D. life. I would give a special thanks to Prof. Wei Wang and Prof. Jiajie Ling at Sun Yat-sen University as they have provided lots of useful help.

Moreover, I would like to thank my colleagues and friends in the High Energy Physics Center and the Daya Bay collaboration, Dr. Hanyu Wei, Dr. Xiangpan Ji, Dr. Yiming Zhang, Dr. Linyan Wan, Dr. Liupan An, Ziyi Guo, Wentai Luo, Lin Zhao, Jinjing Li, Yuzi Yang, Tong Xu, Zhaokan Cheng, and Shuaijie Li. We spent several years together and they helped me a lot.

In the end, I want to thank my family and friends for their encouragement and support in these years. Without their understanding, I could not make today's achievements.

声 明

本人郑重声明：所提交的学位论文，是本人在导师指导下，独立进行研究工作所取得的成果。尽我所知，除文中已经注明引用的内容外，本学位论文的研究成果不包含任何他人享有著作权的内容。对本论文所涉及的研究工作做出贡献的其他个人和集体，均已在文中以明确方式标明。

签 名： 郭磊 日 期： 2020.11.03

Resume and Academic Achievements

个人简历

1991.06.01 出生于山东省成武县。

2010.09 考入广西大学物理科学与工程技术学院物理学专业，2014.07 本科毕业并获得理学学士学位。

2014.09 免试进入到清华大学工程物理系攻读物理学博士学位至今。

发表的学术论文

- [1] Lei Guo for Daya Bay Collaboration, Search For Electron-Antineutrinos Associated With Gravitational-Wave Events GW150914, GW151012, GW151226, GW170104, GW170608, GW170814, and GW170817 at Daya Bay., Chin, Phys. C, Vol. 45, No. 2 (2021). (已被 SCI 录用)
- [2] Lei Guo for Jinping Collaboration, The R&D Progress of the Jinping Neutrino Experiment, TIPP., Particle Physics., Springer, 178-182 (2017). (会议期刊)
- [3] Ghulam Hussain, Lei Guo, et al., Assay of low-background stainless steel by smelting for the neutrino experiment at Jinping, Nucl. Instrum. Meth. A. 881, 65-71 (2018). (SCI 原刊)
- [4] Jinping Collaboration, Physics prospects of the Jinping neutrino experiment, Chin, Phys. C, 41, 023002 (2017). (SCI 原刊)

指导教师学术评语

论文提出了寻找与引力波或伽马暴关联的大亚湾实验中微子信号。大亚湾实验对百兆电子伏以下的反电子中微子能量具有很好的测量精度。实验从 2011 年开始运行到 2020 年，正好涵盖了引力波实验发现的事例与伽马射线暴观测的事例探测时间。寻找可能存在与这些天文观测事例在时间上关联的反电子中微子信号，将有助于探索它们发生的物理机制，具有重要的科学意义。郭磊同学在大亚湾实验，开展了目前国际上最全的引力波或伽马暴关联的反电子中微子信号寻找，研究工作不但涉及了中微子物理方面的内容，还涉及了对天体物理方面的理解，以及在中微子探测器性能以及粒子响应方面的粒子探测方面的知识，工作量饱满。由于他在此方面的独立研究贡献，被指定为大亚湾合作组的文章撰稿人，完成了引力波关联大亚湾中微子信号寻找结果的论文撰写，并以学术期刊论文形式发表。另外，值得一提的是，除了已经包含在其博士论文的工作以外，他还为位于四川西昌中国锦屏地下实验的中微子探测器原型机的研制作出了重要贡献，他设计并搭建了探测器纯水系统。该系统从 2017 年开始已经正常运行至今，确保了原型机的相关研究顺利展开。这项工作也表明他具有很好的实验技术与工程实现的运用能力。以上工作表明郭磊同学达到了清华大学物理学博士学术水平的要求。

郭磊同学在学期间没有出现违反国家法律与学校规章制度的行为与表现。他按要求完成了所有课程的学习，并通过了物理学分委会组织的严格的博士资格考试，表明他在基础理论与专业知识方面有良好的掌握。同时，由于他能够以英文撰写博士论文，虽然经过了多次修改，但是可以看到其外语能力有着明显的进步。在课题组期间，郭磊同学能经常在组会和大亚湾合作会，锦屏中微子合作组会上做学术报告，具备了良好的独立科研能力，学术作风严谨，博士论文研究工作到毕业要求。

答辩委员会决议书

论文提出了寻找与引力波或伽马暴关联的大亚湾实验中微子信号。在多信使天文观测时代，中微子、引力波（GW）和伽马暴（GRB）的联合观测，对了解天体过程的动力学机制及宇宙演化至关重要。论文针对在大亚湾反应堆中微子实验上可能存在与 GW 或 GRB 事例关联的反电子中微子信号开展研究，工作具有重要的科学意义与价值。

论文取得的主要创新性成果包括：

1. 研究了反电子中微子的反贝塔衰变反应在大亚湾实验上的探测。讨论了反冲中子能量对正电子能量测量的影响，并给出了能量修正公式。验证了不同中子慢化及散射模型对本研究影响较小。

2. 进行了 2019 年 3 月为止观测到的引力波事例关联中微子信号搜寻，根据不同的物理动机需求，采用了多个搜索时间窗口，在两个假设模型下给出了关联中微子通量上限结果。

3. 分析了从 2011 年 12 月到 2019 年 3 月期间，共计 2225 个伽马暴事例，在三个搜寻时间窗口和两个能谱模型下，给出了 GRB 关联中微子通量的上限结果。

论文工作表明作者在物理学具有扎实的专业基础知识，具有实验数据分析和独立科研能力。论文写作规范，数据详实，叙述清楚。答辩过程表述清楚，问题回答正确。

答辩委员会表决，一致同意通过论文答辩，并建议授予郭磊理学博士学位。